UNIVERSITÀ
DEGLI STUDI
DI PADOVA

UNIVERSITÀ DEGLI STUDI DI PADOVA

Dipartimento di Ingegneria Industriale

Scuola di Dottorato di Ricerca in Ingegneria Industriale
Indirizzo in Progettazione e Dinamica dei Sistemi Meccanici
Ciclo XXVI

Design of light hybrid vehicles suited to urban and sub-urban mobility

Direttore della Scuola:
Ch.mo Prof. Paolo Colombo .....

Coordinatore d'Indirizzo:
Ch.mo Prof. Alberto Doria .....

Supervisore:
Ch.mo Prof. Silverio Bolognani .....

Co-tutor:
Ch.mo Prof. Alberto Doria .....

Dottorando: Marco Ferrari

.....

Contents

ABSTRACT v

INTRODUCTION vii

1 HYBRID ELECTRIC VEHICLE POWER-TRAINS 1

1.1 HYBRID ELECTRIC VEHICLE 1

1.2 SERIES HYBRID POWER-TRAINS 2

1.3 PARALLEL HYBRID POWER-TRAINS 3

1.4 MIXED HYBRID POWER-TRAINS 4

1.5 PLUG-IN HYBRIDS 5

1.6 HYBRIDNESS 5

1.7 TOYOTA PRIUS CONCEPT 6

1.7.1 Planetary gear 6

1.7.2 Toyota Hybrid System I 7

1.7.3 Hybrid Synergy Drive 8

2 DYNAMICS OF HYBRID VEHICLES 11

2.1 LONGITUDINAL CENTER OF MASS 11

2.2 LONGITUDINAL DYNAMICS 13

2.2.1 AERODYNAMIC FORCE 14

2.2.2 ROLLING RESISTANCE 14

2.2.3 RESISTANT FORCE CAUSED BY ROAD GRADE 15

2.2.4 LOAD TRANSFERS 16

2.3 FOUR-BAR LINKAGE 17

2.4 LATERAL DYNAMICS 17

2.4.1 STEADY TURNING 20
2.5 MATLAB CODE 22
2.5.1 GUI INPUT 22
2.5.2 GUI OUTPUT 25

3 SYNCHRONOUS ELECTRIC MACHINES 33
3.1 REFERENCES 35
3.2 ANALYTICAL MODEL OF THE STATOR 35
3.2.1 ELECTRICAL LOADING 35
3.2.2 STATOR MAGNETIC POTENTIAL 37
3.2.3 QUANTITIES IN THE ROTOR REFERENCE FRAME 38
3.3 ROTOR WITH ONE FLUX-BARRIER PER POLE 39
3.3.1 ROTOR MAGNETIC POTENTIAL AND AIR-GAP FLUX DENSITY 39
3.3.2 TORQUE COMPUTATION 41
3.4 ROTOR WITH THREE FLUX-BARRIERS PER POLE 42
3.4.1 ROTOR MAGNETIC POTENTIALS 43
3.4.2 TORQUE COMPUTATION 45
3.5 VALIDATION OF THE ANALYTICAL MODEL WITH THREE FLUX-BARRIERS PER POLE 45
3.6 ROTORS WITH DIFFERENT NUMBER OF BARRIERS PER POLE: INVESTIGATION ON $\Delta\tau$ AND τ_{avg} 48
3.7 FURTHER IMPROVEMENTS BY MEANS OF THE MACHAON CONFIGURATION . 49
3.8 SATURATION EFFECTS 52
3.8.1 FLUX LINKAGES 54
3.8.2 TORQUE RIPPLE, MEAN TORQUE AND POWER AND POWER FACTOR . 55
3.9 THE PMAREL MOTOR 57
3.9.1 SATURATION EFFECTS DUE TO THE PHASE CURRENT VARIATION . . 62
3.10 EXPERIMENTAL RESULTS 63

4 DYNAMICS OF SYNCHRONOUS ELECTRIC MACHINES 67
4.1 ROTOR VIBRATION MODES 67
4.2 MECHANICAL STRESS 70

5 APPLICATIONS 73
5.1 HY-SNAKE 74
5.1.1 POWER-TRAIN OVERVIEW 75
5.1.2 CHASSIS DESIGN 77
5.1.3 OPTIMIZATION OF THE FOUR-BAR LINKAGE 80
5.1.4 IPM MOTORS 83

5.1.5 FINAL PERFORMANCES 84
5.2 VELOMOBILE 86
5.2.1 GENERAL LAYOUT OF THE VEHICLE 86
5.2.2 HUMAN HYBRID POWER TRAIN 88
5.2.3 DYNAMIC ANALYSIS 89
5.2.4 SYNCHRONOUS RELUCTANCE MACHINE 93
5.2.5 FINAL PERFORMANCES 99
5.3 APRILIA RS4 125 HYBRID 102
5.3.1 POWER-TRAIN OVERVIEW 103
5.3.2 PERFORMANCE OF THE ELECTRICAL MACHINE 104
5.3.3 PERFORMANCE OF THE ELECTRIC CONVERTER 105
5.3.4 ENERGY STORAGE SYSTEM (ESS) 107
5.3.5 CONTROL UNIT 113
5.3.6 HEM PROTOTYPE 114
5.3.7 RACE TRACK TESTS 116

ABSTRACT

ITALIAN VERSION

Attualmente nei paesi sviluppati ed in via di sviluppo i problemi di inquinamento dovuti al traffico ed alla carenza di fonti energetiche stanno diventando sempre più importanti; per questo motivo vi è un notevole sviluppo di tecnologie elettriche ed ibride per il trasporto stradale. L'impiego di veicoli a due o tre ruote è particolarmente adatto a ridurre il traffico nelle aree urbane ed il consumo energetico relativo ai mezzi di trasporto.
L'introduzione di un sistema di propulsione elettrica o ibrida in un veicolo leggero è una sfida poiché alcuni componenti pesanti e voluminosi devono essere alloggiati in spazi limitati. Inoltre la dinamica dei veicoli a due e tre ruote è fortemente influenzata dalle masse aggiunte (la massa dei componenti elettrici è comparabile con quella del telaio). In questa tesi vengono presentati diversi sistemi di propulsione adatti a veicoli ibridi leggeri. Nella prima parte viene data una panoramica sui diversi tipi di configurazioni ibride. Poi viene presentata un'analisi sul comportamento dinamico dei veicoli leggeri con particolare enfasi sui veicoli a tre ruote.
La seconda parte della tesi presenta un modello analitico della macchina a riluttanza finalizzato a semplificare la progettazione stessa, con l'obiettivo di minimizzare il ripple di coppia. Nella terza parte vengono presentati tre casi studio: un veicolo a tre ruote con propulsione ibrida di tipo "range extender ", una velomobile a tre ruote con sistema di propulsione umano-elettrico ed una moto con propulsione ibrida di tipo "parallelo".

ENGLISH VERSION

The problems of pollution, traffic jam and lack of energy sources are becoming more and more important and for these reasons there is a significant development of electric and hybrid vehicles. The introduction of an electric or hybrid propulsion system in a small vehicle is a challenge because some heavy and voluminous components have to be accommodated in a narrow room and because the dynamic behavior of a two- three-wheeled vehicle is strongly influenced by the added masses. This thesis deals with propulsion systems suited to light hybrid vehicles. In the first part of the thesis an overview on different kind of hybrid configurations is given. Then a careful analysis on the dynamic behavior of light vehicles with particular emphasis on three-wheeled vehicles is presented. The second part of the thesis shows an analytical model of the reluctance machine aimed both to simplify the designing and to minimize the torque ripple. In the third part three cases study are presented: a range extender three-wheeled vehicle, a human-electric three-wheeled velomobile and a mild-hybrid motorcycle.

INTRODUCTION

Nowadays in developed and developing countries the problems of pollution, traffic jam and lack of energy sources are becoming more and more important; for these reasons there is a significant development of electric and hybrid technologies for road transportation.
The employment of two- or three-wheeled vehicles is particularly suited to reduce the traffic in urban areas and the energy consumption related to the means of transportation.

The introduction of an electric or hybrid propulsion system in a small vehicle is a challenge because some heavy and voluminous components have to be accommodated in a narrow room and because the dynamic behavior of a two- three-wheeled vehicle is strongly influenced by the added masses (the mass of the electric components is comparable with the mass of the chassis). Specific dynamic studies are needed to maintain the handling and the stability properties of conventional vehicles equipped with internal combustion engines.

Three-wheeled vehicles are suited to accommodate electric or hybrid propulsion systems since they have more useful space than a conventional motorcycle. Thanks to the experience of the Motorcycle Dynamics Research Group (MDRG) of Padova in three-wheeled vehicles, this thesis mainly deals with such a vehicles.

The efficiency of hybrid and pure electric power-trains is very important since it is strongly related to the vehicle range. The electric machine is an important element of such a power-trains. To the aim of maximizing the whole efficiency, electrical machine's losses have to be reduced as much as possible.
A careful design analysis have to be performed in order to choose the best electric machine typology taking into account its tasks (e.g. for generating purpose in range extender vehicles or for traction applications).
In this thesis permanent magnet synchronous machines have been considered, with particular emphasis in synchronous reluctance machines and permanent magnet assisted reluctance machines. A specific analytical model of such a machines is presented. Performance analysis have been carried out with the aim of minimizing the torque ripple and maximizing the efficiency.

In Chapter 1 an overview on hybrid power-trains is presented. Chapter 2 deals with the dynamics of light vehicles in particular three-wheeled vehicles. Chapters 3 and 4 show the studies made on the electrical machine. Finally in Chapter 5 three cases study are presented: a range extender three-wheeled vehicle, a human-electric three-wheeled velomobile and a mild-hybrid motorcycle.

Chapter 1

HYBRID ELECTRIC VEHICLE POWER-TRAINS

The chapter deals with an overview on different kinds of hybrid power-trains suitable for vehicles in general (not limited to light vehicles).
In the first part the main architectures (parallel, series, range-extender) are presented. In the second part the "Toyota Hybrid System" is described.

1.1 HYBRID ELECTRIC VEHICLE

A hybrid vehicle combines any two power (energy) sources. Possible combinations include diesel/electric, gasoline/flywheel, and fuel cell/battery. Typically one energy source is storage and the other is conversion of a fuel to energy. The combination of two power sources may support two separate propulsion systems.

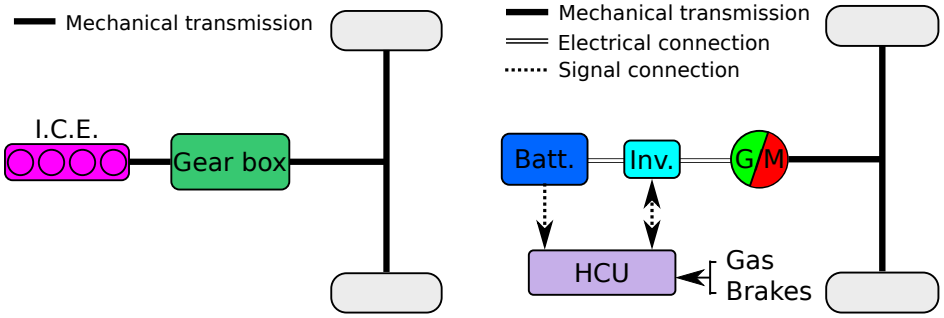

(a) Pure gasoline (b) Pure electric

Figure 1.1: Pure power-trains

Consistent with the definition of hybrid above, the Hybrid Electric Vehicle (HEV) combines a gasoline engine with an electric motor. An alternate arrangement is a diesel engine and an electric motor. Throughout this thesis, the word *ICE* is used to denote the gasoline or diesel engine. Further the word *motor* signifies an electric motor or the generator/motor (G/M). A hybrid power-train may consist of a gasoline engine combined with an G/M. A HEV is composed of components from a pure electrical vehicle (see Fig. 1.1b) and a pure gasoline vehicle (see Fig. 1.1a). The G/M installed in the HEV enables regenerative braking. For the HEV, the G/M may be tucked directly behind the ICE. The transmission appears next in line.

This arrangement has two torque producers; the G/M in motor mode (M-mode) and the ICE. The battery and G/M are connected electrically.

One new component, the Hybrid Control Unit (HCU), has been added. The function of the HCU is to monitoring the whole system in order to enhance driving experience.
Mixing propulsion from the ICE and G/M opens many new control dilemmas to be solved and decisions to be made. Major functions are to maximize miles per gallon (mpg) and minimize exhaust emissions, assuming, of course, that maximum mpg is the design goal. Integration of mechanical components, electrical components, and the control software is as important as hardware, if not more so. Integration and software challenges are enormous. Components must engage and disengage smoothly.
Numerous minor functions of the HCU include component protection by monitoring battery State Of Charge (SOC), battery temperature, electric motor overheating, and ICE overheating.

There are three common design options for HEV: series, parallel, and mixed.

1.2 SERIES HYBRID POWER-TRAINS

Fig. 1.2 shows that the series HEV has two shafts that are not connected. Hence, the ICE can run at optimum speed and throttle setting to give minimum fuel consumption. Further, control of ICE operating point provides easier control to minimize emissions. The ICE and generator are a unit, but this unit is not connected to the drive shaft. The ICE and generator can be located anywhere.

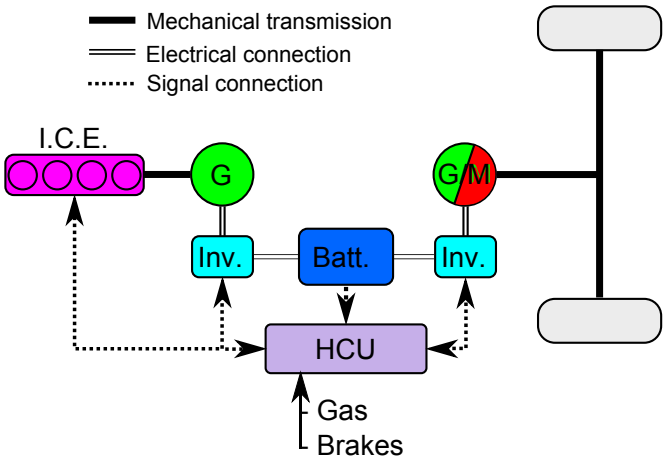

Figure 1.2: Series power-train.

Naturally, the series configuration does have some disadvantages. The generator, which is needed, is a heavy, extra component. The generator is sometimes called an alternator/rectifier. The capacity of the generator (G) equals the total power of the HEV. Likewise, the traction motor, which is shown as G/M in Fig. 1.2, must have power equal to total vehicle power for propulsion.
The series HEV has double conversion of energy:

$$Mechanical \longrightarrow Electrical \longrightarrow Mechanical$$

All mechanical power is converted to electric and then back to mechanical. Each conversion has associated losses. Although a disadvantage relative to weight, the high power traction G/M

does yield an advantage precisely because of its high power. During regenerative braking, large braking power may be available. If the G/M in G-mode does not have enough power rating to absorb the braking power, friction brakes are used. Regenerative braking efficiency suffers.

1.3 PARALLEL HYBRID POWER-TRAINS

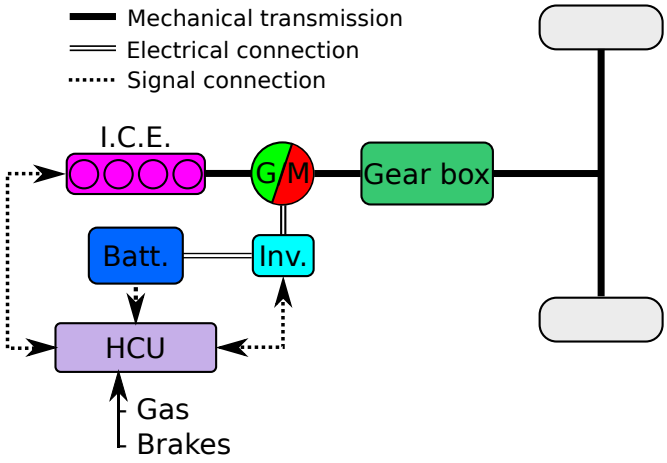

Figure 1.3: Parallel power-train.

With parallel layout, a direct mechanical connection can be traced from the ICE to the drive wheels, see Fig. 1.3. This is the most simple parallel configuration. The resultant traction power is achieved by the contributions of the ICE and of the G/M together. With this configuration is not allowed a pure electric mode because of the fixed connection between ICE and G/M.

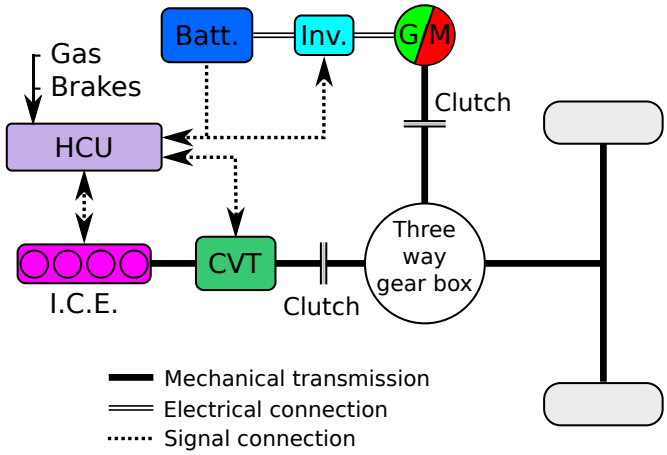

Figure 1.4: Advanced parallel power-train.

A more advanced parallel layout is shown in Fig. 1.4. Now a direct mechanical connection can be traced from the M/G to the drive wheels and, likewise, from the ICE to the drive wheels. Because of this direct mechanical connection a transmission is needed to match ICE speed with drive shaft speed. In this application, a Continuously Variable Transmission (CVT) is superior to a transmission with a limited number of fixed gear ratios.

Among the advantages of a parallel hybrid is the single energy conversion for both electrical

and mechanical. This single energy conversion is shown diagrammatically as:

$$ICE\ (mechanical) \longrightarrow Drive\ shaft\ (mechanical)$$

$$Motor\ (electrical) \longrightarrow Drive\ shaft\ (mechanical)$$

Except at low battery SOC, the ICE runs only when the car is moving. Parallel hybrid does not need the heavy component, which is the alternator/rectifier or generator (G) of Fig. 1.2. Considerable design flexibility exists in selecting the size of the G/M. The G/M can be sized to meet the required function at somewhat less than full vehicle power.

Some features of the advanced parallel hybrid are the ability to operate with ICE alone, electric motor only, or with both motor and ICE supplying torque. The electric-only mode is very important for improved mpg during stop-and-go operations. The parallel hybrid can respond to the demand for large instantaneous changes in either torque or power. The fast response is an advantage in traffic.

Among the disadvantages of parallel arrangement are the various added power-train parts such as added clutches and transmissions. Typically a three-shaft transmission is needed; two input shafts and one output shaft. See Fig. 1.4 which shows a three-way gearbox. Further, the ICE throttle setting varies causing difficulty in controlling emissions. Varying ICE throttle setting causes ICE operation at higher specific fuel consumption. Because of the need to mechanically connect the ICE with the drive shaft, choices for location of the ICE are limited.

1.4 MIXED HYBRID POWER-TRAINS

Fig. 1.5 shows an example of mixed power-train. Looking at this configuration it is worth noticing that it engages parts of series and parallel power-trains. Mixed power-trains are pretty complex because require a high number of components. Thanks to the clutch it is possible to connect the ICE directly to the wheels or only to the G/M 1. The G/M 2 can be used to improve the total traction power of the vehicle during accelerations and to improve the regenerative braking capability during decelerations. Compared to the power-train shown in Fig. 1.4, the mixed power-train allows to use both the G/Ms and the ICE when the maximum power is required. During cruise motion the ICE can work at maximum efficiency charging batteries. Pure electric mode is also possible thanks to the G/M 2.

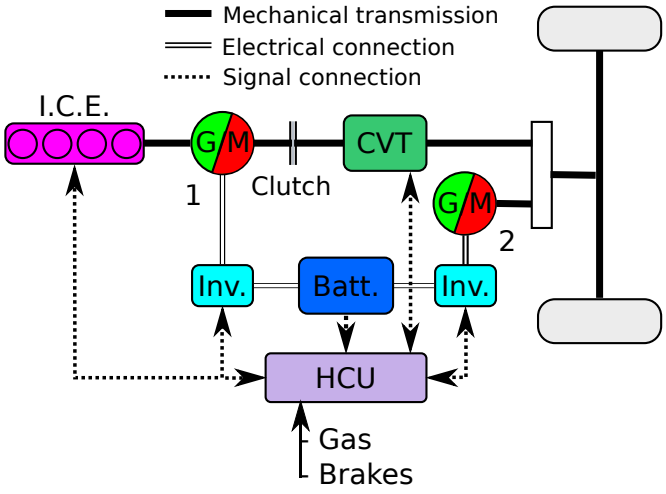

Figure 1.5: Mixed power-train.

1.5 PLUG-IN HYBRIDS

In HEVs the battery is charged as the vehicle is driven. The tedious task of recharging the battery is avoided.
Actually HEVs are gaining popularity, people want to add a larger battery to an HEV to get 80, 90, 100, or 200 mpg. The more energetic battery creates a class of hybrids known as the plug-in hybrid electric vehicle (PHEV). A plug-in hybrid, as the name implies, requires plugging in to an electrical outlet for recharging.

How far can a plug-in go in electric-only mode with a large battery? For instance, from GM EV1[1] data, with $16.2\ kWh$, a distance of $145\ km$ can be covered. From these numbers the energy per kilometer equals $16.2\ kWh/145\ km = 112\ Wh/km$.

PHEV will most likely use lithium-ion (Li-ion) batteries to lessen the weight gain of a large battery. However, Li-ion batteries are expensive.

1.6 HYBRIDNESS

Some hybrids have more than one generator/motor (G/M). Hybrids with in–wheel motor and all–wheel–drive (AWD), have more than one motor.

It is possible to define an index *H* to classify the degree of hybridization of vehicles:

$$H = \frac{\sum\ power\ of\ all\ traction\ motors\ (electric)}{\sum\ power\ of\ all\ traction\ motors\ (electric) + ICE\ power} \tag{1.1}$$

H is commonly named hybridness.

As an example of hybridness consider a car with the propulsion:
ICE: 90 kW (max)
Electric motor: 20 kW (max)

$$H = \frac{20\ kW}{20\ kW + 90\ kW} = 0.18\ \% \tag{1.2}$$

The series hybrid has motor power approximately equal to ICE power. For H less than 50 %, the series hybrid morphs into the mixed hybrid. For H greater than 50 %, the series hybrid transforms into the range extender electric vehicle. H greater than 50 % is also the region for the plug–in hybrid.

For small hybridness, that is H much less than 50 %, the optimum hybrid operates near the best specific fuel consumption line on the ICE map. Small H corresponds to mild hybrids. For a band of hybridness near 50 %, the efficiencies of both electrical and ICE components affect the optimum operating points. Values of H larger than 40 % are termed full hybrids. For large values of H, that is, near 100 %, hybrid optimization focuses on the G/M, battery, and power electronics.

Further details about hybrid power-trains are in [1].

[1]The General Motors EV1 was an electric car produced and leased by the General Motors Corporation from 1996 to 1999. It was the first mass-produced and purpose-designed electric vehicle of the modern era from a major automaker, and the first GM car designed to be an electric vehicle from the outset.

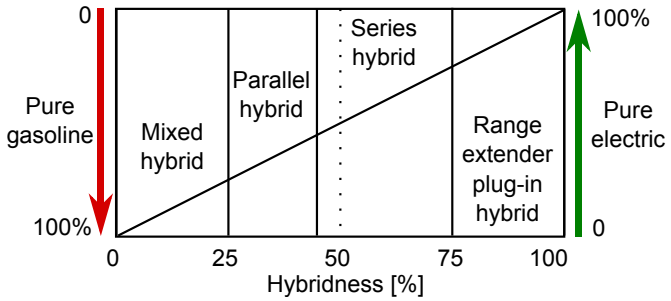

Figure 1.6: Mixed, parallel, series and plug–in hybrid.

1.7 TOYOTA PRIUS CONCEPT

The Toyota Hybrid System (THS) power train combines an ICE and an electric motor. THS was installed in the passenger vehicle Prius, which was introduced in December 1997 and became the first mass-produced hybrid passenger vehicle in the world and also the bestselling one so far. The key component of Prius is the THS which distributes the power of the ICE to the generator and to the drive shaft by using a planetary gear system. In 2006, Toyota developed a new generation THS, termed Hybrid Synergy Drive (HSD) and its application in the *SUV Lexus GS 450h* obtained a distinct advantage both in the vehicle power performance and fuel economy. Sales of Toyota hybrid vehicles have been expanding year by year, increasing their presence in the automotive market and contributing to the improvement of the global environment.

1.7.1 Planetary gear

The planetary gear set is the core of the power split transmission and the means through which ICE torque splits, a portion to the generator and a portion to the driveline, [2]. Fig. 1.7 shows a schematic of a planetary gear composed of four planets supported by a carrier and interposed between the central sun gear and the outer ring gear.

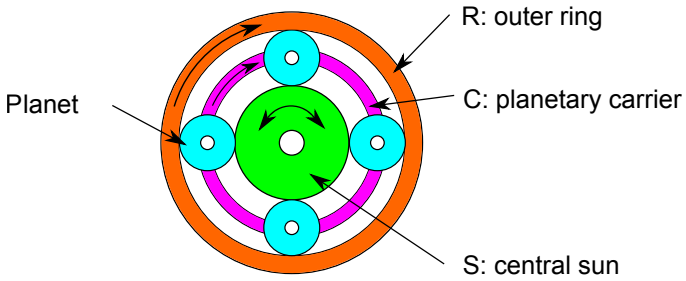

Figure 1.7: Power split device layout.

The fundamental equation of the planetary gear is that the gear rotation must maintain a fixed ratio of angular velocity relative to the carrier body. This fixed ratio is defined as the basic ratio, k, and it equals the radius of the ring, r_r divided by the radius of the sun gear, r_s. The basic ratio of the planetary gear is:

$$-k = -\frac{r_r}{r_s} = -\frac{r_r r_p}{r_p r_s} = \frac{\omega_s - \omega_c}{\omega_r - \omega_c} \tag{1.3}$$

in which r_p is the radius of one planet, and $\omega_r, \omega_c, \omega_s$ are the rotation speeds of ring, carrier and sun respectively.

Alternatively, (1.3) can be written in terms of its gear radii as:

$$\omega_c = \frac{r_s}{2r_c}\omega_s + \frac{r_r}{2r_c}\omega_r \tag{1.4}$$

1.7.2 Toyota Hybrid System I

Prius I is the first hybrid generation from Toyota and it was introduced in the U.S. market in December 1997.
The basic design of the THS I is shown in Fig. 1.8. The schematic diagram illustrates the paths of power flow between the generator G/M 1, ICE, planetary gear set and the electric traction motor G/M 2.

G/M 1 (Secondary motor-generator): Acts as a motor sharing power with ICE to drive G/M 2, generates power to recharge the high voltage battery or starts the ICE. By regulating the amount of electrical power generated (by varying G/M 1's mechanical torque and speed), G/M 1 effectively controls the continuously variable transmission.

G/M 2 (Primary motor-generator): Drives the wheels, regenerates power for high voltage battery energy storage or brakes the vehicle. G/M 2 provides a smooth acceleration from standstill. During regenerative braking, G/M 2 acts as a generator, converting kinetic energy into electrical energy, storing this electrical energy in the battery.

Without contribution by the battery, the overall driveline power equals the ICE power. ICE power arrives at the driveline via a geared path (Carrier → Ring) and an electric path (Sun gear → generator → motor → Ring gear). ICE and motor power are summed to total traction power at the planetary ring gear. Net driveline power is available at the vehicle axle to provide for acceleration and to match the road load.
In power split, the battery contributes energy during electric only vehicle launch and to augment acceleration. The battery recuperates energy during deceleration (on grade) and braking, [3].

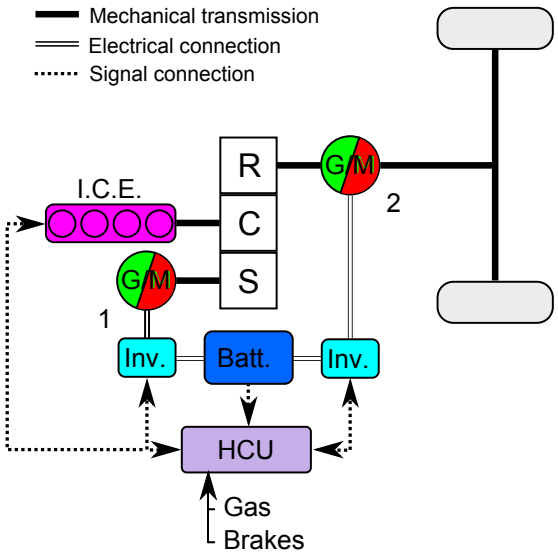

Figure 1.8: First generation Toyota Prius power-train (THS I).

1.7.3 Hybrid Synergy Drive

The first generation TSD, well known as *Highlander Hybrid* has been introduced in 2004 and its basic structure is shown in Fig. 1.9. The first part of the power-train (ICE, G/M 1 and gear set) is the same of THS I, whereas in the second part has been added another gear set. The latter connects the first gear set (Ring 1 $\rightarrow$ Carrier 2), the G/M 2 (Sun gear 2) whereas the Ring 2 is locked.

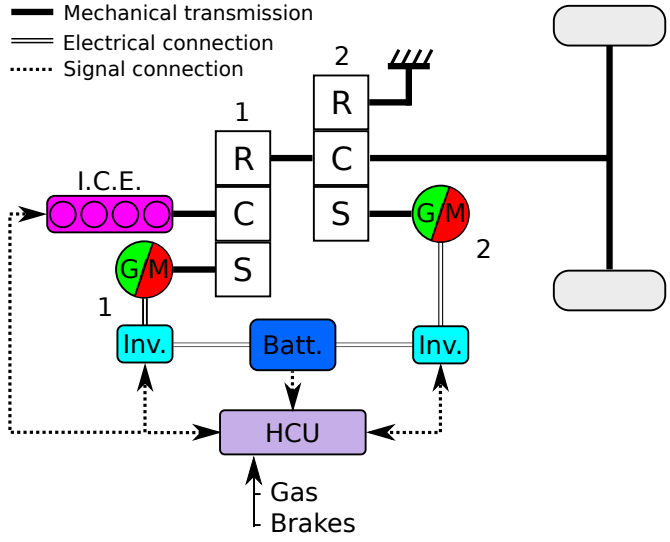

Figure 1.9: Second generation Toyota Prius power-train (THS II).

The second generation HSD can be seen as a double planetary gear mechanism. The front part of the mechanism is similar to THS I, while the rear part is the innovation of HSD. It is a two-stage motor speed reduction device, which can rationally regulate motor speed and torque to achieve the decoupling of ICE speed and torque based on different conditions. Therefore it can allow the ICE to work at high-efficiency status.

The speed reduction device uses a Ravigneaux-type gear train for compactness and to ensure two large reduction ratios. Two wet friction brakes are used to switch between the reduction ratios. Applying brake B1 provides a reduction ratio of 1.9 in the high gear range, while applying brake B2 provides a reduction ratio of 3.9 in the low gear range. The two-stage motor speed reduction device is operated automatically by a hydraulic control system, achieving smoother shift performance by collaborating generator, motor, and regenerative braking system controls. By optimizing the hydraulic control system to accommodate the higher output of the ICE and motor, the Lexus GS 450h has smoother shift performance than conventional automatic transmission vehicles, [4].

The HSD operates in distinct phases depending on speed and demanded torque. Here are a few of them:

Battery charging: The HSD can charge its battery without moving the car, by running the ICE and extracting electrical power from G/M 1.

Engine start: To start the ICE, power is applied to G/M 1 to act as a starter.

Neutral gear: Most jurisdictions require automotive transmissions to have a neutral gear that decouples the ICE and transmission. The HSD "neutral gear" is achieved by turning the electric motors off. Under this condition, the planetary gear is stationary if the vehicle wheels are not turning.

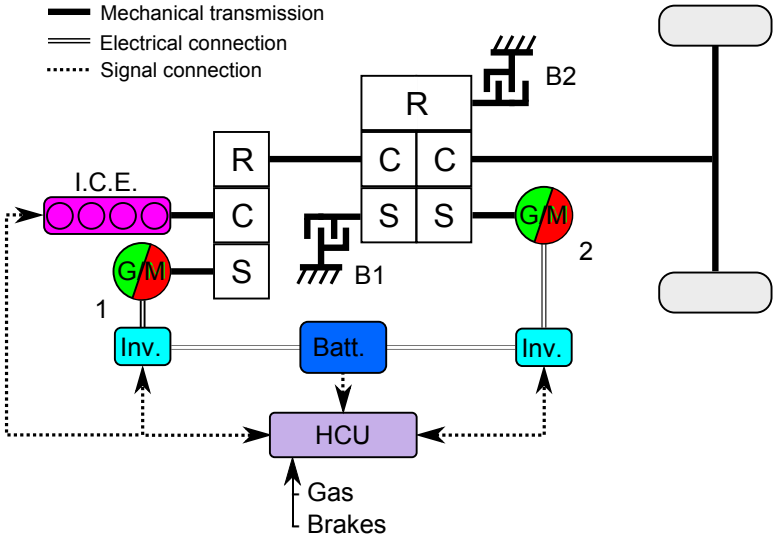

Figure 1.10: Hybrid Synergy Drive (HSD).

EV operation: At slow speeds and moderate torques the HSD can operate without running the ICE at all: electricity is supplied only to G/M 2, allowing G/M 1 to rotate freely (and thus decoupling the ICE from the wheels). This is popularly known as "Stealth Mode". The car can be driven in this silent mode for some miles even without gasoline.

Low gear: When accelerating at low speeds in normal operation, the ICE turns more rapidly than the wheels but it does not develop sufficient torque. The extra torque is given by the G/M 2 which is fed to G/M 1, acting as a generator.

High gear: When cruising at high speed, the ICE turns more slowly than the wheels but develops more torque than needed. G/M 2 then runs as a generator to remove the excess ICE torque, producing power that is fed to G/M 1 acting as a motor to increase the wheel speed. In steady state, the ICE provides all of the power to propel the car unless the ICE is unable to supply it (as during heavy acceleration, or driving up a steep incline at high speed). In this case, the battery supplies the difference.

Regenerative braking: By drawing power from G/M 2 and depositing it into the battery pack, the HSD can simulate the deceleration of normal engine braking while saving the power for future boost. The regenerative brakes in an HSD system absorb a significant amount of the normal braking load, so the conventional brakes on HSD vehicles are undersized compared to brakes on a conventional car of similar mass.

Engine braking: The HSD system has a special transmission setting to provide engine braking on hills. During braking when the battery is approaching potentially damaging high charge levels, the electronic control system automatically switches to conventional engine braking, drawing power from G/M 2 and shunting it to G/M 1, speeding the ICE with throttle closed to absorb energy and decelerate the vehicle.

Chapter 2

DYNAMICS OF HYBRID VEHICLES

This chapter deals with the dynamics of light vehicles with particular reference to three-wheeled vehicles with two rear wheels (fixed), one front wheel (tilting) and a four-bar mechanism which connects the front and the rear frame.

In the first part of the chapter the longitudinal dynamics is presented, whereas in the second part the lateral dynamics is analyzed. Finally, in the third part a specific Matlab® code is presented; this software is aimed to better integrate the mechanical design with the position of the electrical components in order to optimize the dynamic behavior.

Further details about the three-wheeled vehicle can be found in [8]. Further details about the vehicle dynamics can be found in [9].

2.1 LONGITUDINAL CENTER OF MASS

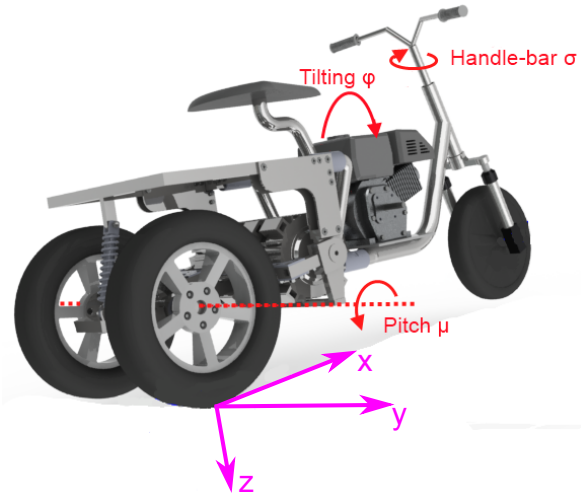

Figure 2.1: SAE reference frame.

The position of a three-wheeled vehicle Center Of Mass (CoM) has a significant influence on the vehicle dynamic behavior. The CoM position depends on the distribution and the values of the masses of the individual components of the vehicle (engine, tank, electric motors, batteries, power electronics, wheels, frame, etc.). Since in a hybrid/electric vehicle, the heavier

components are batteries, power electronics and motor/engine, their location greatly influences the location of the whole vehicle CoM (CoM_m).

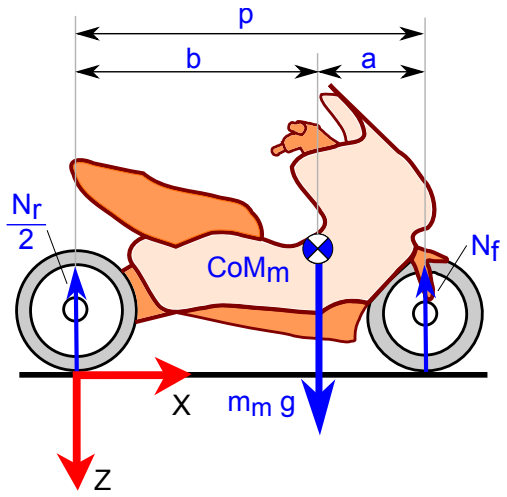

Figure 2.2: Longitudinal position of the CoM.

Referring to Fig. 2.2, N_f indicates the load on the front wheel and N_r the total load on the rear wheels under static conditions. These two loads are determined by the whole mass distribution of the vehicle and, as a consequence, by the position of the CoM_m.
The longitudinal distance between the contact point of the rear wheel and the CoM_m is defined as b, whereas a is the distance between the contact point of the front wheel and the CoM_m.
The wheelbase of the vehicle can be defined as: $p = a + b$.
The loads N_f and N_r can be computed as follows:

$$N_f = g\, m_m \frac{b}{p} \tag{2.1}$$

$$N_r = g\, m_m \frac{p-b}{p} \tag{2.2}$$

where g is the gravity force and m_m is the total mass of the vehicle.

When the CoM is rear ($N_r > 50\%$), there is an easier transfer of the power to the ground. However a greater N_f partially compensates the effects of the aerodynamic forces that tend to unload the front wheel.

In general the position of the rider moves the overall CoM_m toward the back of the vehicle, see Fig. 2.3. As a consequence the load on the rear wheel increases whereas the load on the front wheel decreases.

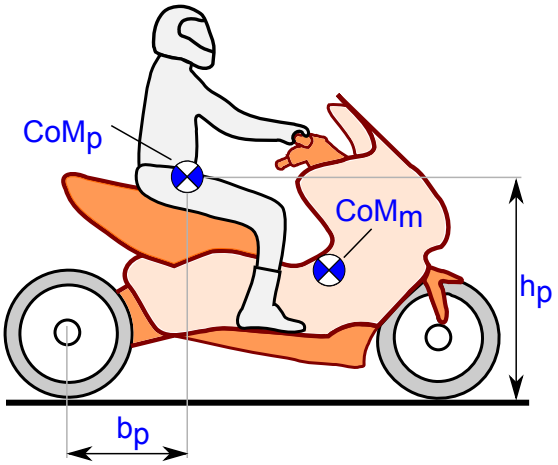

Figure 2.3: CoM position of the three-wheeled vehicle (CoM_m) and the rider (CoM_p).

2.2 LONGITUDINAL DYNAMICS

The behavior of motorcycles during rectilinear motion depends on longitudinal forces. During steady state motion, the traction force delivered by the motor equals the resistant forces that oppose the forward motion. Resistant forces depends mainly on three phenomena:

- aerodynamic resistance to forward motion;
- resistance to tire rolling;
- the component of the weight force caused by the road grade.

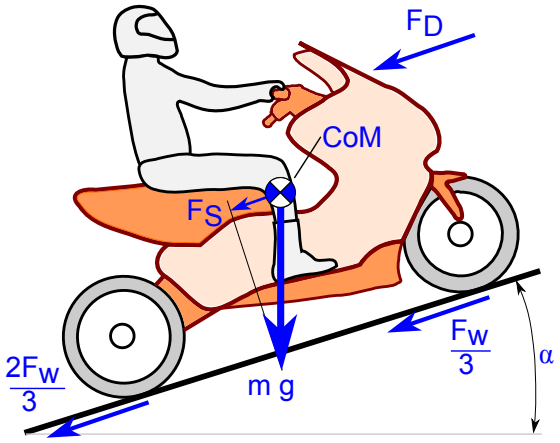

Figure 2.4: Resistant forces acting on a three-wheeled vehicle.

2.2.1 AERODYNAMIC FORCE

The aerodynamic actions that influence the dynamic behavior of a vehicle are three forces (drag, lift and lateral force) and three moments (pitching, yawing and rolling moment). The most important component related to the rectilinear behavior is the drag force. It is applied in the pressure center which is usually located above the total CoM (vehicle + rider) of the vehicle.
The drag force influences both the maximum velocity and the acceleration of the vehicle. The drag force is proportional to the square of the vehicle forward velocity:

$$F_D = \frac{1}{2}\,\rho\,C_D\,A_f\,V^2 \tag{2.3}$$

where ρ is the air density (equal to $1.167\ kg/m^3$ at atmospheric pressure of $987\ mbar$ and at $20°$), V is the vehicle forward velocity (m/s), C_D is the coefficient of aerodynamic resistance, also called *drag coefficient* (dimensionless) and A_f is the frontal area of vehicle (m^2).

The value of C_D strongly depends on the shape of the vehicle.

The frontal area A differs according with the type of vehicle and is strongly influenced by the body of the rider and his position during the travel. Reference values might vary from 0.4 to $1\ m^2$; the smallest value is related to sport motorcycles whereas the biggest value refers to touring motorcycles.

The product $C_D\ A$ gives the drag area and it can vary from 0.18 for race motorcycles to $0.7\ m^2$ for completely faired motorcycles.
The power to overcome aerodynamic drag, P_D, in watts is:

$$P_D = F_D V \tag{2.4}$$

Hence, combining the equations (2.3) and (2.4) gives:

$$P_D = \left(\frac{1}{2}\,\rho\,C_D\,A_f\,V^2\right) V = \frac{1}{2}\,\rho\,C_D\,A_f\,V^3 \tag{2.5}$$

2.2.2 ROLLING RESISTANCE

The rolling radius of a wheel that rotates without slipping on a flat surface is defined by the ratio between the forward velocity (V) and its angular speed (ω):

$$R_0 = \frac{V}{\omega} \tag{2.6}$$

The effective rolling radius R_0 is lower than the radius of the unloaded tire R because of the deformation of the tire, see Fig.2.5. R_0 depends on the type of the tire, its radial stiffness, the load, the inflation pressure and the forward velocity (V).

During the motion the lower part of the tire is compressed nonuniformly because of the hysteresis of the material. This causes a change in the distribution of the contact pressures, which therefore are not symmetric. Contact pressures are higher on the side of the forward direction, respect to the z-axis in Fig. 2.5. The resultant of the normal contact pressures N is displaced of the distance d (respect to the z-axis) on the side of the forward direction as well. The forward displacement is called: rolling resistant coefficient $f_w = d/R$.

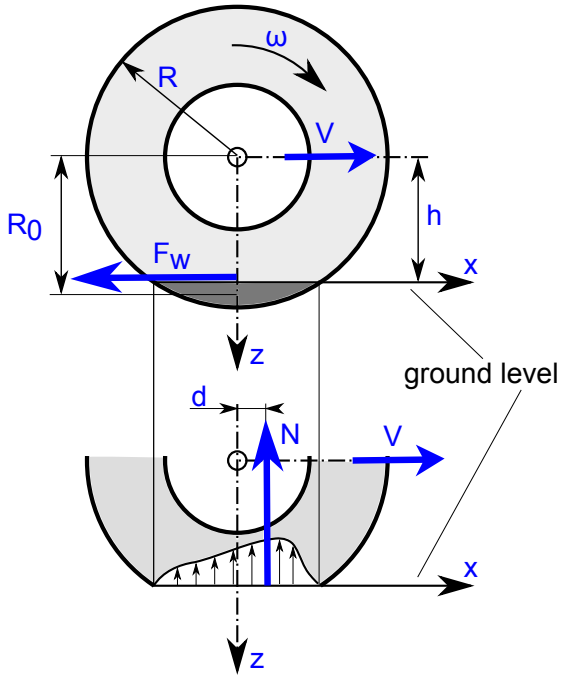

Figure 2.5: Forces acting on a rolling wheel.

Hence, to move the wheel with constant forward velocity it is necessary to overcome a rolling resistance moment equal to:

$$M_w = d\ N \tag{2.7}$$

The resistance to rolling is expressed by means of a resistance force that opposes the forward motion, and whose value is given by the product of the rolling friction coefficient f_w and the vertical load:

$$F_w = f_w\ N = \frac{d}{R} N \tag{2.8}$$

2.2.3 RESISTANT FORCE CAUSED BY ROAD GRADE

The resistant force due to the road grade is equal to the component of the weight force as shown in Fig. 2.4:

$$F_P = m\ g\ \sin\alpha \tag{2.9}$$

where m is the total mass of the vehicle ($m = m_m + m_p$) in kg and α is the steepness of the hill, angle between horizontal and the road surface (see Fig. 2.4).

2.2.4 LOAD TRANSFERS

Referring to Fig. 2.6, the rolling resistance force is zero (i.e. $F_w = 0$) and the road surface is flat (i.e. $F_P = 0$). Only the drag force, whose pressure center height is h_D, opposes the vehicle motion. F_{trac} is the total traction force delivered by the motors/engine and N_f, N_r are the reactive vertical forces exchanged between tires and road.

The equations of equilibrium allow to determine the unknown values of N_f, N_r:

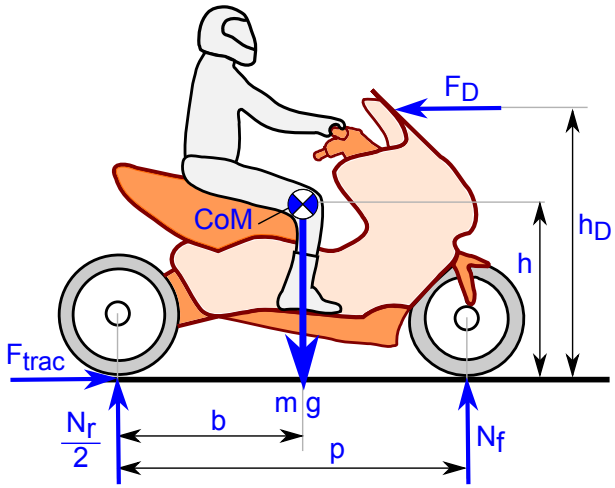

Figure 2.6: Forces acting on a three-wheeled vehicle during straight running.

$$\begin{cases} F_{trac} - F_D = 0 & \text{Equilibrium of horizontal forces} \\ m\,g - N_r - Nf = 0 & \text{Equilibrium of vertical forces} \\ F_{trac}\,h - N_r\,b + N_f\,(b-p) + F_D\,(h_D - h) = 0 & \text{Equilibrium of moments respect to CoM} \end{cases} \tag{2.10}$$

Solving the system in (2.10) the loads on the tires are:

$$N_f = m\,g\,\frac{b}{p} - F_{trac}\,\frac{h_D}{p} \qquad \text{Dynamic load on the front wheel} \tag{2.11}$$

$$N_r = m\,g\,\frac{(p-b)}{p} + F_{trac}\,\frac{h_D}{p} \qquad \text{Dynamic load on the rear wheels} \tag{2.12}$$

The solutions in (2.11) and (2.12) are composed of two terms. The first is the static load on the wheels, depending on the weight force:

$$N_{sf} = m\,g\,\frac{b}{p} \qquad N_{sr} = m\,g\,\frac{(p-b)}{p} \tag{2.13}$$

The second term is the load transfer N_{tr}, directly proportional to the traction force F_{trac} and to the pressure center height h_D. The load transfer is inversely proportional to the wheelbase p.

$$N_{tr} = F_{trac}\,\frac{h_D}{p} \tag{2.14}$$

2.3 FOUR-BAR LINKAGE

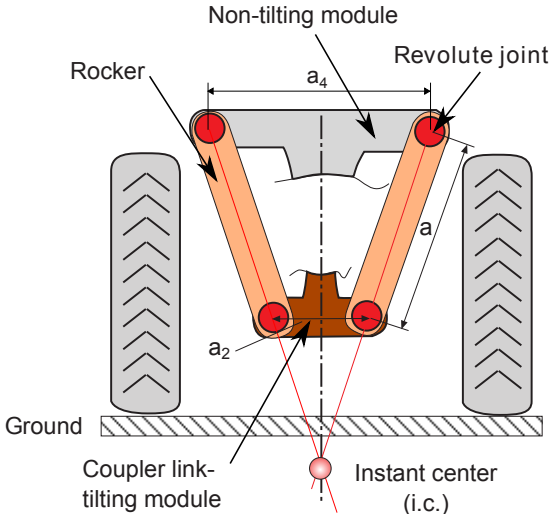

Figure 2.7: Sketch of the four-bar linkage.

The four-bar linkage shown in Fig. 2.7 is the innovative aspect of three-wheeled vehicles with two fixed rear wheels. The four-bar linkage is significantly responsible of the dynamic behavior of the vehicle.

The four-bar linkage is made up of the rear frame which does not tilt, the tilting front frame and two connecting bars (rockers) that link the front and rear frame by means of four revolute joints. With this configuration the front frame rotates around an instantaneous tilting axis. The intersection of the tilting axis with the four-bar linkage plane defines the instantaneous center of rotation (i.c.). The i.c. position in the linkage plane is defined by the intersection of the two axes of the rockers, as shown in Fig. 2.7.

Therefore, the relative positions among the four revolute joints define the i.c. position, that could be above the road plane, on the road plane or below the road plane. The vertical and lateral position of the i.c. and the tilting axis inclination affect the load transfer from the inner rear wheel to the external rear one during a cornering maneuver.

A detailed analysis of the lateral dynamics of the three-wheeled vehicle is presented in the following Section.

2.4 LATERAL DYNAMICS

The four-bar linkage presented in Fig. 2.7 is now sketched in Fig. 2.8 in order to define its kinematic equations.
The kinematic analysis of the four-bar linkage has been carried out considering the upper left revolute joint as the origin (O_A) of the fixed reference frame.

The vectors closure condition is described by the following equations:

$$\vec{Z}_1 + \vec{Z}_2 - \vec{Z}_3 - \vec{Z}_4 = 0 \tag{2.15}$$

$$\vec{Z}_4 - \vec{Z}_2 = \vec{Z}_5 \tag{2.16}$$

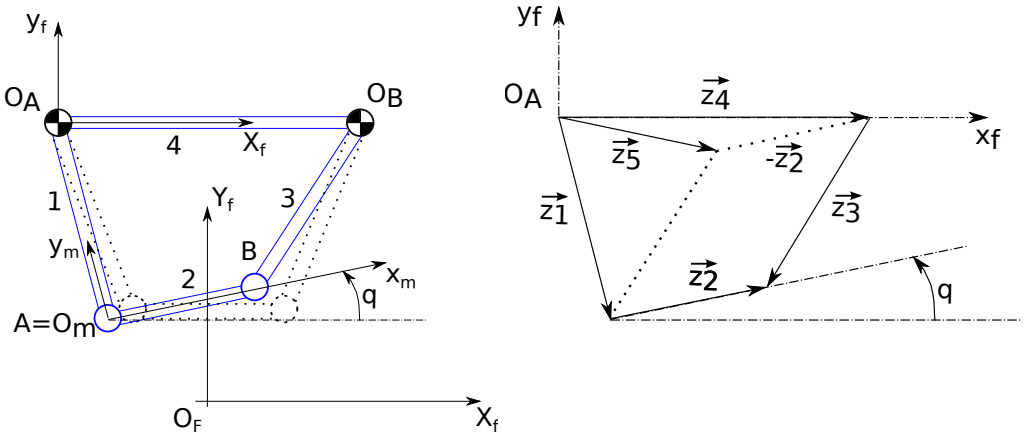

(a) Four-bar mechanism (b) Vectors closure condition of the four-bar linkage

Figure 2.8: Four-bar linkage.

Referring to Fig. 2.8a, the following relations are stated:

- $|\vec{Z}_4| = a_4$ Frame
- $|\vec{Z}_2| = a_2$ Coupler-link
- $|\vec{Z}_1| = |\vec{Z}_3| = a$ Rocker

The vectors closure condition $\vec{Z}_4, -\vec{Z}_2, \vec{Z}_5$ written in function of cosines and sines is:

$$a_4 \ \cos\theta_4 - a_2 \ \cos q = |\vec{Z}_5| \ \cos\theta_5 \tag{2.17}$$

$$a_4 \ \sin\theta_4 - a_2 \ \sin q = |\vec{Z}_5| \ \sin\theta_5 \tag{2.18}$$

Hence, the magnitude of $\vec{Z}_5$ is:

$$|\vec{Z}_5| = \sqrt{a_2^2 - 2 \ a_4 \ a_2 \ \cos q + a_4^2} \tag{2.19}$$

and the phase of $\vec{Z}_5$ is:

$$\theta_5 = \arctan\left(\frac{-a_2 \ \sin q}{-a_2 \ \cos q + a_4}\right) \tag{2.20}$$

To the aim of defining the phase of $\vec{Z}_3$, the vectors closure condition $\vec{Z}_1, -\vec{Z}_3, -\vec{Z}_5$ is now considered:

$$a \ \cos\theta_1 = a \ \cos\theta_3 + |\vec{Z}_5| \ \cos\theta_5 \tag{2.21}$$

$$a \ \sin\theta_1 = a \ \sin\theta_3 + |\vec{Z}_5| \ \sin\theta_5 \tag{2.22}$$

obtaining:

$$\theta_3 = \theta_5 - \arccos\left(\frac{-|\vec{Z}_5|}{2\,a}\right) \tag{2.23}$$

By means of the same equations the phase of $\vec{Z}_1$ is stated as well:

$$\theta_1 = \theta_5 - \arccos\left(\frac{|\vec{Z}_5|}{2\,a}\right) \tag{2.24}$$

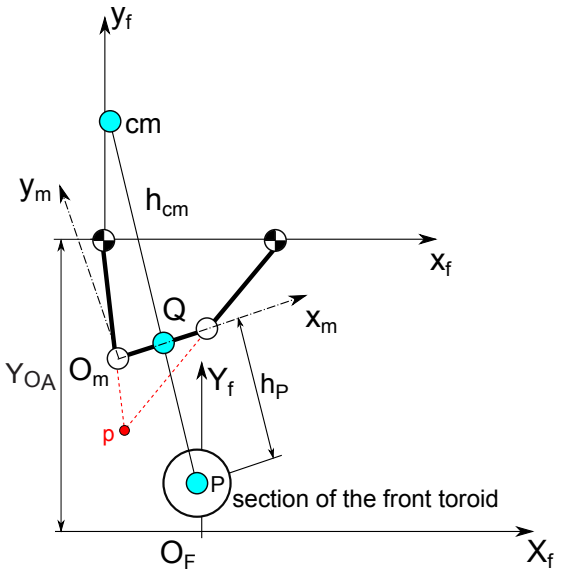

Figure 2.9: Motion of the most important points in the plain of the connecting rod.

As stated in Section 2.3, the intersection of the two axes of the rockers defines the instantaneous center of rotation. This point is highlighted in Fig. 2.9 with the letter p (red dot). The trajectory described by this point for different roll angles is named fixed centrode. The coordinates of the point p in the fixed reference frame (with origin O_A) are x_{pf} and y_{pf}:

$$x_{pf}\ \tan\theta_1 = (x_{pf} - a_4)\ \tan\theta_3 \tag{2.25}$$

hence:

$$\begin{cases} x_{pf} = \dfrac{-a_4\ \tan\theta_3}{-\tan\theta_3 + \tan\theta_1} \\ y_{pf} = x_{pf}\ \tan\theta_1 \end{cases} \tag{2.26}$$

Defining the coordinates of the origin O_A respect to the reference frame with origin in O_F (Fig. 2.9) they become:

$$\begin{cases} X_{O_A} = -a_4/2 \\ Y_{O_A} = \text{independent variable} \end{cases} \tag{2.27}$$

it is possible to obtain the global coordinates of the fixed centrode in the reference frame with origin in O_F:

$$\begin{cases} X_{pf} = x_{pf} + X_{O_A} \\ Y_{pf} = y_{pf} + Y_{O_A} \end{cases} \tag{2.28}$$

Referring to Fig. 2.9 the coordinates of the mobile reference frame with origin in O_m respect to the fixed reference frame with origin in O_A are:

$$\begin{cases} x_{O_m} = a\ \cos\theta_1 \\ y_{O_m} = a\ \sin\theta_1 \end{cases} \tag{2.29}$$

hence, in the reference frame with origin in O_F they are:

$$\begin{cases} X_{O_m} = x_{O_m} + X_{O_A} \\ Y_{O_m} = y_{O_m} + Y_{O_A} \end{cases} \tag{2.30}$$

Referring to Fig. 2.9 the distance between the center of the coupler-link (Q) and the center of the toroid of the front wheel (P) is h_P:

$$h_P = Y_{O_A} - r_f - \sqrt{a^2 - \frac{a_4 - a_2}{2}^2} \tag{2.31}$$

in which r_f is the radius of the toroid of the front wheel.
The coordinates of the point P are:

$$\begin{pmatrix} X_P \\ Y_P \end{pmatrix} = \begin{bmatrix} \cos q & -\sin q \\ \sin q & \cos q \end{bmatrix} \begin{pmatrix} \frac{a_2}{2} \\ -h_P \end{pmatrix} + \begin{pmatrix} X_{O_m} \\ Y_{O_m} \end{pmatrix}$$

2.4.1 STEADY TURNING

The steady turning maneuver is useful to study the stability of the vehicle. Such a maneuver consists of a cornering action at constant speed. This allows to know the overturning limits for vehicles (in general) and in particular for three-wheeled vehicles with linkage.

Referring to Fig. 2.6 the total mass of the vehicle (m) can be split into two parts: M_f and M_r that represent the masses related to the front and to the rear frame respectively:

$$M_f = m\ \frac{b}{p} \tag{2.32}$$

$$M_r = \frac{m\ (p-b)}{p} \tag{2.33}$$

and the static loads can be rewritten as:

$$N_f = g\ M_f \tag{2.34}$$

$$N_r = g\ M_r \tag{2.35}$$

On the horizontal plane, the equilibrium of the forces acting on the whole vehicle (traslation) is given by:

$$m\ R_c\ \Omega^2 - F_{sf} - F_{sr} = 0 \tag{2.36}$$

in which R_c is the turning radius, Ω is the yaw rate and F_{sf}, F_{sr} are the lateral forces on the front and on the rear tires respectively.
The equilibrium of the forces acting on the whole vehicle (rotation) is:

$$-(p-b)F_{sf} + bF_{sr} = 0 \tag{2.37}$$

Then:

$$F_{sf} = \frac{b\ m\ \Omega^2\ R_c}{p} = \Omega^2\ M_f\ R_c \tag{2.38}$$

$$F_{sr} = \frac{(-b+p)\ m\ \Omega^2\ R_c}{p} = \Omega^2\ M_r\ R_c \tag{2.39}$$

Referring to Fig.2.10, the equilibrium of the forces acting on the rear frame is given by:

$$N_{r,ext} + N_{r,int} = Nr \tag{2.40}$$

in which $N_{r,ext} = N_r/2 + \Delta N_r$ and $N_{r,int} = N_r/2 - \Delta N_r$. The load transfer ΔN_r can be expressed as:

$$\Delta N_r = \frac{N_{r,ext} - N_{r,int}}{2} \tag{2.41}$$

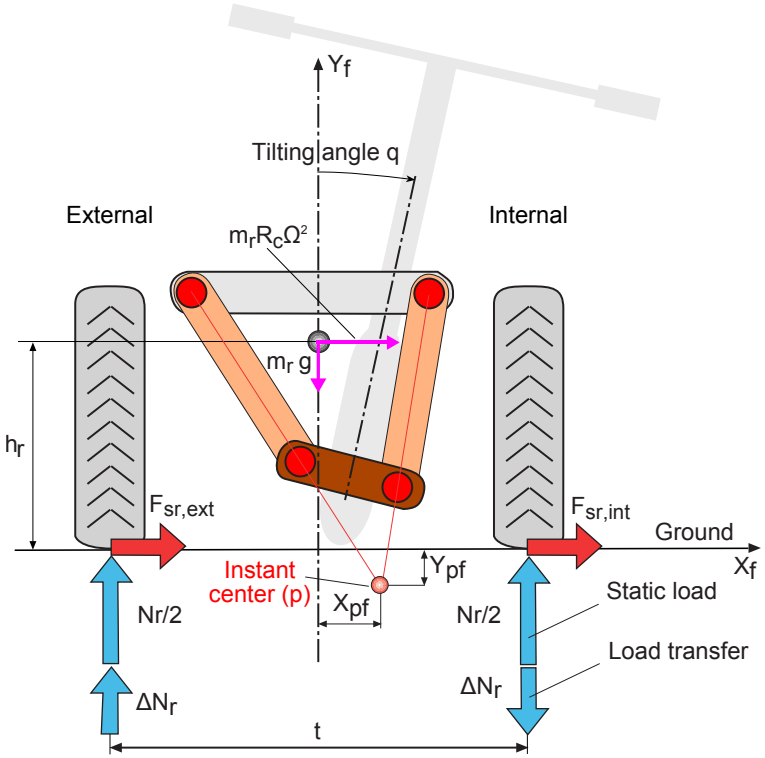

Figure 2.10: Equilibrium of the rear frame.

Lateral load transfers on the rear wheels depend on the yaw rate of the vehicle for a given R_c. Stated as m_f and m_r the masses of the front and the rear frame, h_f the CoM height of the

front frame respect to the *SAE* reference frame (see Fig. 2.1), and q the roll angle, the yaw rate Ω is:

$$\Omega = \sqrt{\frac{g\,(-M_f + m_f)\,(-X_P + X_{pf}) + g\,h_f\,m_f\,\sin q}{R_c\,[h_f\,m_f\,\cos q + (M_f - m_f)\,Y_{pf}]}} \tag{2.42}$$

the vehicle forward velocity become:

$$V = \Omega\,R_c \tag{2.43}$$

Finally the load transfer (ΔN_r) on the rear wheels can be expressed as follows:

$$\Delta N_r = \frac{g\,(M_r - m_r)\,X_{pf}}{t} + \frac{(M_r - m_r)\,\Omega^2\,R_c\,Y_{pf}}{t} + \frac{\Omega^2\,R_c\,h_r\,m_r}{t} \tag{2.44}$$

where t is the vehicle track, as shown in Fig.2.10.
The vehicle is stable until the following relation is satisfied:

$$\Delta N_r < \frac{N_r}{2} \tag{2.45}$$

2.5 MATLAB CODE

To the aim of designing the propulsion system and estimating the final performances of a light three-wheeled vehicle, a specific Matlab code has been developed. Such a software is based on a Graphical User Interface (GUI) in order to make easier the approach with the program.

The main interface of the GUI is shown in Fig. 2.11. This is a real command window, since it is possible to manage the input and the output given by the software. Referring to Fig. 2.11, the command window is composed of two parts:

- Input: the vehicle can be customized by setting several parameters, both mechanical and electrical;
- Output: the performances of the vehicle are given in accordance with the input values.

2.5.1 GUI INPUT

To the aim of describing the vehicle and its electrical components, many parameters have to be set up. The input files menu is divided in five sub-menu:

- Test cycles.
- Mechanical inputs.
- Electrical inputs.
- CoM positioning.
- Additional settings.

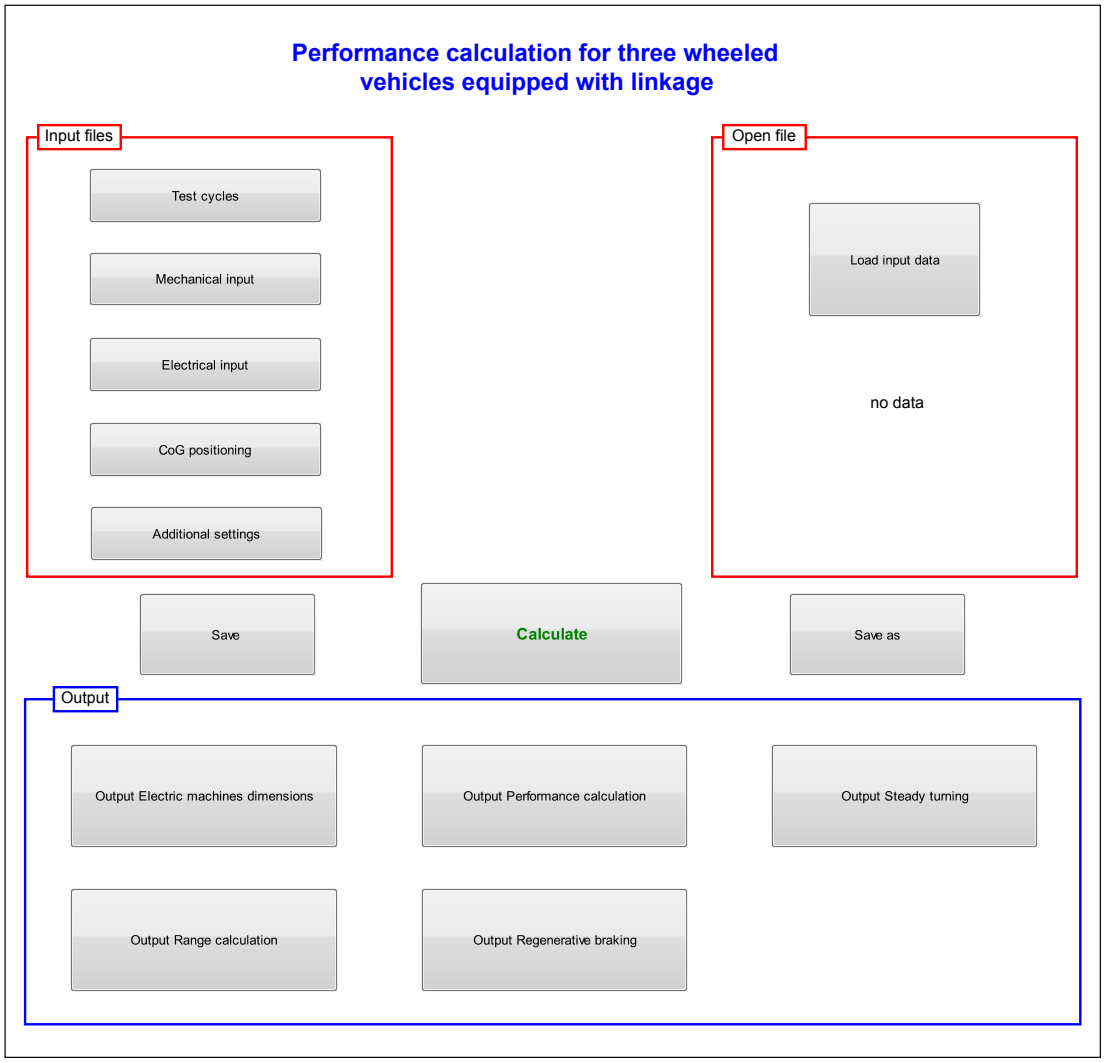

Figure 2.11: GUI main interface

TEST CYCLES

In such a sub-menu the user can choose the test cycle for estimating the performance (range) of the vehicle. It is possible to choose between two test cycles: the ECE-15[1] test cycle, suited to urban environments (see Fig. 2.12a) and a customized test cycle suited to sub-urban environments (see Fig. 2.12b). The latter can be set up by the user by imposing acceleration, deceleration and cruise speed of the test cycle.
The road grade can be also specified in each test cycle.

[1]The ECE-15 test cycle was introduced in the 1970 to define the levels of emission of light vehicles. The test cycle was devised to be representative of city-center driving and has a maximum speed of only $50\ km/h$.

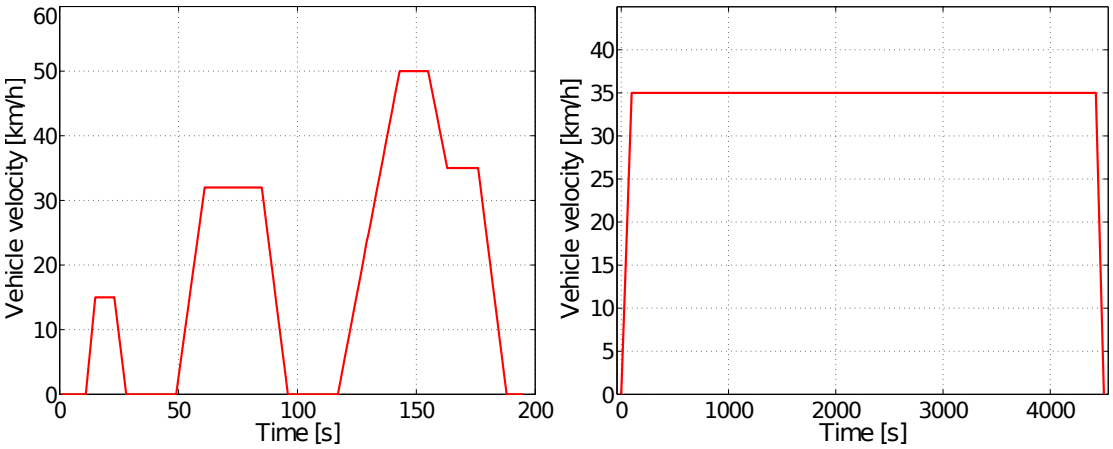

(a) ECE-15 (b) Sub-urban

Figure 2.12: Test cycles available in the GUI.

MECHANICAL INPUTS

Mechanical inputs are related to the mechanical parameters of the vehicle, such as track, wheelbase, wheel radius, wheel inertia, vehicle mass, etc. Values related to the resistant forces acting on the vehicle (e.g. drag coefficient, rolling coefficient, additional forces, etc.) can be also set up in this sub-menu.

ELECTRICAL INPUTS

Electrical inputs deal with the electrical components placed on-board the vehicle. In particular, the main parameters of the electrical machines can be set up. For instance, rated power, rated speed, rated current, rated torque and efficiency need to be specified in order to estimate the main electric machine dimensions and weights. In addition, it is possible to enable the boost[2] and/or the regenerative braking mode for each motor.

Electronic converter specifications can be imposed as well. Volume density, weight density and efficiency allow to estimate the total volume and density of the electronic converter.

If the power-train includes i.c. engines, their characteristics can be included in the electrical input file. Moreover if there is an electric generator coupled with the i.c. engine, its main parameters (included the power electronic) can be set up.

The energy storage system characteristics are included as well. It is possible to specify the nominal voltage, capacity, weight, volume and efficiency.

Finally some additional components can be added, such as wire weights, control units and so on.

[2]With the term "boost" is meant the overload mode. It is useful during either acceleration or overtaking maneuvers.

COM POSITIONING

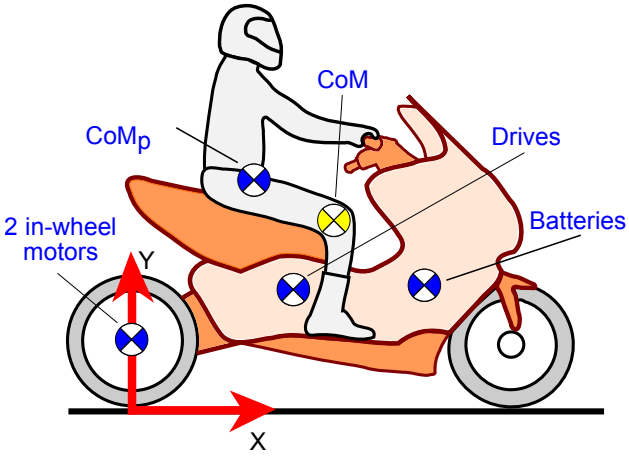

Figure 2.13: Components positioning

In this file it is possible to specify the CoM coordinates of the vehicle without electrical components on-board. Then, all the electrical components included in the file "Electrical inputs" can be positioned in the vehicle by specifying their CoM coordinates. As consequence, the total CoM can be computed, considering the rider and an additional passenger as well. Fig. 2.13 shows an example of components positioning in the vehicle. This feature is very important since the position of each component is strongly related with the dynamics of the whole vehicle. A correct disposition of the weights allow to gain stability and, as consequence, safety.

ADDITIONAL SETTINGS

In the last input file it is possible to introduce the mechanical characteristics (speed versus torque) of the electrical motors, both in rated and boost mode. In addition, the integration times for the vehicle dynamics calculation can be set up.

OPEN FILE

Once all the input files are filled in, it is possible to store the input data for future calculations.

2.5.2 GUI OUTPUT

To the aim of highlighting the potentialities of this software, an example of calculation is given. The reference vehicle is a pure electric motorcycle and it is equipped with a four-bar linkage in order to connect the two fixed rear wheels with the front tilting wheel. As shown in Fig. 2.13, the vehicle is equipped with two rear in-wheel motors, whereas in the front frame are placed the drives of the motors and the batteries.

Table 2.1 collects the main parameters of the reference vehicle used in the simulations. In order to study the lateral dynamics of the vehicle, all the calculations presented in Section 2.4 have to be taken into account. For this reason the four-bar linkage geometry must be well known.

The output generated by the software are:

- Electric machine dimensions.
- Range calculation.
- Performance calculation.
- Regenerative braking.
- Steady turning.

Table 2.1: Parameters used in the simulations

Symbol	Specification	Value	Unit
C_D	Drag coefficient	0.7	$-$
A	Frontal section area	1	m^2
f_v	Rolling resistance coefficient	0.02	$-$
F_{fr}	Additional friction forces	8	N
	Vehicle properties		
m_m	Vehicle mass	165	kg
m_p	Rider mass	80	kg
t	Vehicle track	0.45	m
p	Vehicle wheelbase	1.44	m
b	X coordinate of the CoM	0.531	m
	Four-bar linkage properties		
a_4	Frame	0.408	m
a_2	Coupler-link	0.156	m
a	Rocker	0.315	m
X_{O_A}	X-coordinate of O_A in O_F	$-a_4/2$	m
Y_{O_A}	Y-coordinate of O_A in O_F	0.53	m
X_{pf}	X-coordinate of the i.c. in O_F ($q = 0$)	0	m
Y_{pf}	Y-coordinate of the i.c. in O_F ($q = 0$)	0.063	m
	Steady turning		
R_c	Curve radius	24	m

ELECTRIC MACHINE DIMENSIONS

The main electric machine dimensions are given in this output file. In particular, the volume and the weight of each electric machine are estimated. This is important to evaluate the space needed for a certain amount of propulsive power and to design the chassis. The volume and the weight of the drives are estimated as well.

The main characteristics of the electric machines adopted in the reference vehicle are collected in Table 2.2.

Table 2.2: Electric machine characteristics of the reference vehicle

Specification	Value	Unit
Two in-wheel motors with		
Rated torque @ 640 rpm	45	Nm
Rated power @ 640 rpm	2.5	kW
Mass	14	kg
Two power converters with		
Maximum power	5	kW
Mass	1.4	kg
Volume	2	$litres$

In addition, in the same output file, the position of the total CoM is given. The CoM coordinates of the reference vehicle are:

$$\begin{cases} XCoG = 0.531\ m \\ YCoG = 0.547\ m \end{cases} \tag{2.46}$$

RANGE CALCULATION

This output file contains the calculations related to the range of the vehicle. Depending on the type of the test cycle and on the specific power-train chosen, the software calculates the range of the vehicle. If the urban test cycle is selected the range is given in pure electric mode, whereas the sub-urban test cycle is usually used to test the range in hybrid mode. The range of a pure electric vehicle depends on the size of the battery pack, whereas in an hybrid vehicle it depends on both the battery pack and the gasoline tank.

The power-train of the reference vehicle is pure electric. The battery pack has a rated capacity of 100 Ah and a mass of 21 kg thanks to the adopted Lithium technology. The estimated range in urban driving is about 100 km.

PERFORMANCE CALCULATION

This output file generates some curves in order to present the performances of the vehicle during acceleration. Trends of traction forces, resistant forces, acceleration, speed and load transfers are given.
For instance, Fig. 2.14 presents the results of the reference vehicle. More in detail Fig. 2.14a shows the total traction force given by the electrical machines at the wheels and the resistant forces acting on the vehicle in the plane force versus vehicle velocity. The intersection between the two curves represents the cruise speed of the vehicle.
Figs. 2.14b and 2.14c show the acceleration and the vehicle velocity versus time behaviors. The maximum acceleration is equal to $4\ m/s^2$ considering a boost torque two times the rated one, whereas the maximum speed is $53\ km/h$.
Finally Fig. 2.14d shows the loads on both the rear and the front frame during the vehicle acceleration. The maximum load transfer (that equals the difference between the initial and the final static load on both the rear and the front frame) is $1890 - 1600 = 290\ N$. This value is useful to design the chassis of the vehicle.

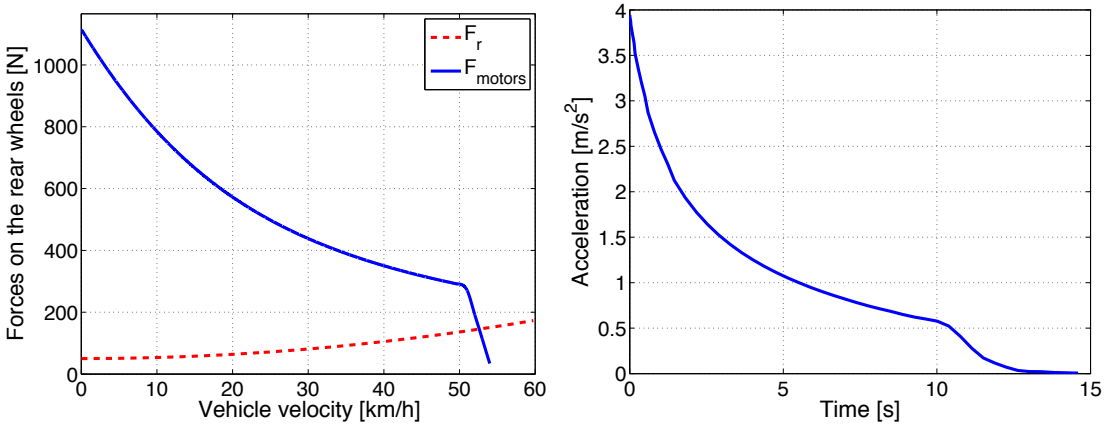

(a) Traction forces

(b) Vehicle acceleration

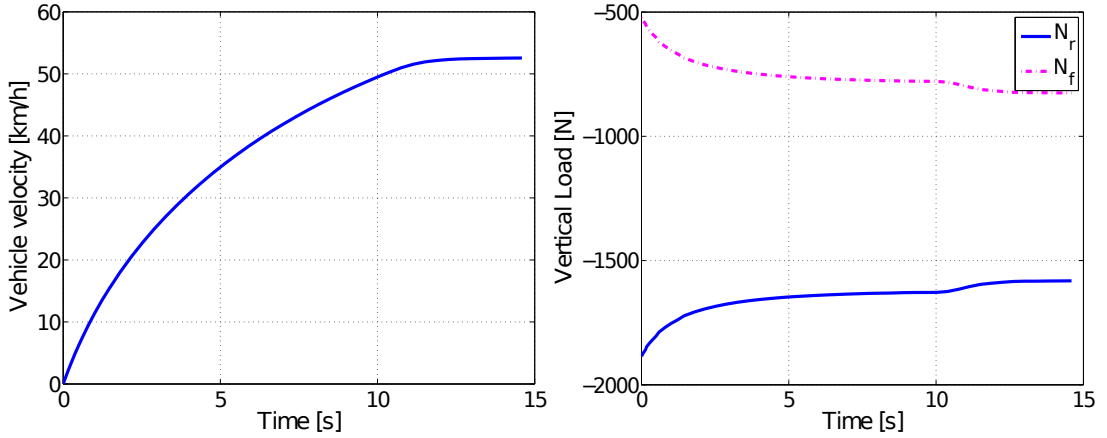

(c) Vehicle velocity

(d) Loads on the rear/front frame during acceleration

Figure 2.14: Vehicle performances during acceleration.

REGENERATIVE BRAKING

The same curves represented above are now given during braking phase.
Fig. 2.15a shows the braking forces (at the wheels) acting on the reference vehicle. The solid line represents the force exerted by the in-wheel motors during regenerative braking. The dashed line shows the resistant forces which in this case contribute to brake the vehicle. The dotted line indicates the braking force given by the front brake.
It is worth noticing that the maximum braking force exerted by the in-wheel motors is not constant because of their mechanical characteristic. To the aim of using the maximum available braking force, the minimum value is reached at the maximum speed (when the braking starts) whereas the maximum value is reached at the minimum speed (when the vehicle stops).
Figs. 2.15b and 2.15c show the deceleration and the vehicle velocity versus time behaviors. The maximum deceleration is equal to $-5\ m/s^2$. Starting from a constant speed of $50\ km/h$, the stopping distance is about $26\ m$.
Finally Fig. 2.14d shows the loads on both the rear and the front frame during the vehicle deceleration. The maximum load transfer is $1250 - 1052 = 198\ N$. This value is useful to design the chassis of the vehicle.

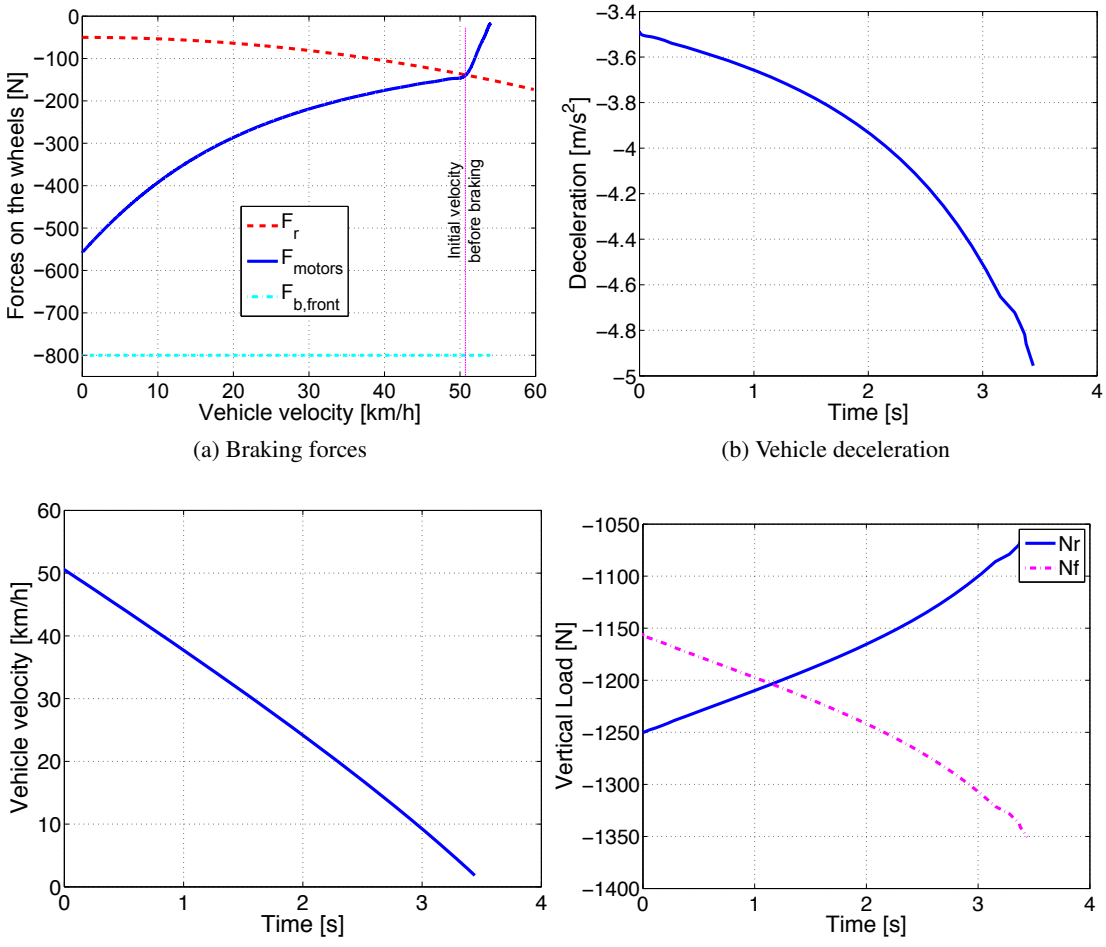

(a) Braking forces

(b) Vehicle deceleration

(c) Vehicle velocity

(d) Loads on the rear/front frame during deceleration

Figure 2.15: Vehicle performances during braking.

To the aim of verifying the effectiveness of the braking forces, some adherence curves

are given for both the rear and front wheels. The adherence limit is given by the relation: $F_{braking} < \mu_{adh}\ N_v$. μ_{adh} is a coefficient that takes into account the road conditions (with ice, with snow, wet and dry) and N_v is the vertical load on the wheels. Referring to Fig.2.16a the solid lines show the load transfer on the rear wheels multiplied by different μ_{adh}. The dashed line shows the braking force given by the in-wheel motors.
Fig.2.16b shows the adherence curves for the front wheel. The only braking force acting on the front wheel (dashed line) is the one given by the front brake.
It is worth noticing that in-wheel motors do not give a constant braking force if they are controlled like in the motoring mode (constant current). In other words, the motors should be overloaded as their mechanical characteristic decreases, to obtain a constant braking force.

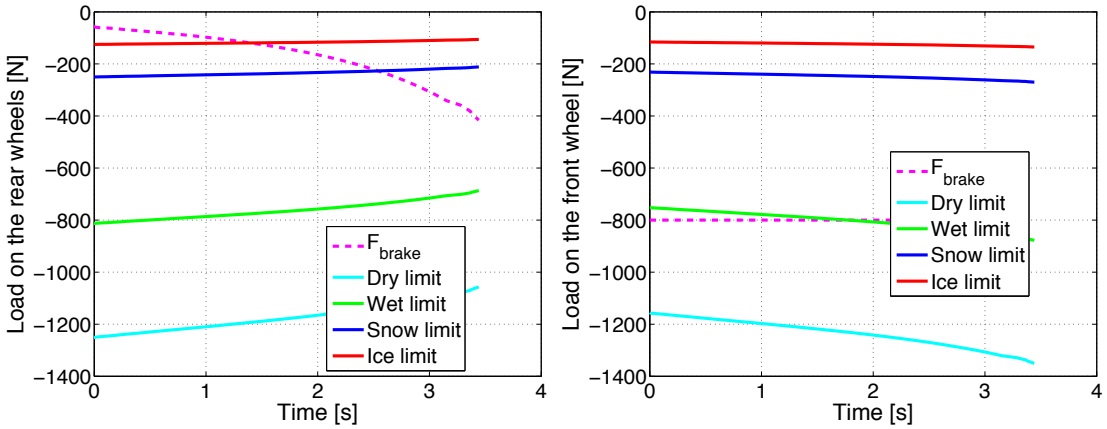

(a) Adherence of the rear wheels

(b) Adherence of the front wheel

Figure 2.16: Tires adherence during braking.

STEADY TURNING

The last output file gives the lateral load transfer on the rear wheels during a steady turning maneuver.
For the reference vehicle the lateral load transfer has been calculated considering a curve radius of $24\ m$ (see Table 2.1). In Fig. 2.17 the lateral load transfer has been normalized respect to the static load on each rear wheel and it has been calculated for different tilting angles of the front frame. It is worth noticing that when the tilting angle is $30°$ the centrifugal acceleration is $5.3\ m/s^2$ and the load transfer is 50% of the static load on each wheel. Roll-over takes place when the load transfer is equal to the static load on each wheel.

The lateral load transfer of the three-wheeled vehicle with linkage and with the mass distribution of Fig. 2.13 is compared with the lateral load transfer of a similar vehicle with simple pivot. The connection with the four-bar linkage decreases the load transfer with a significant reduction in the risk of roll-over.

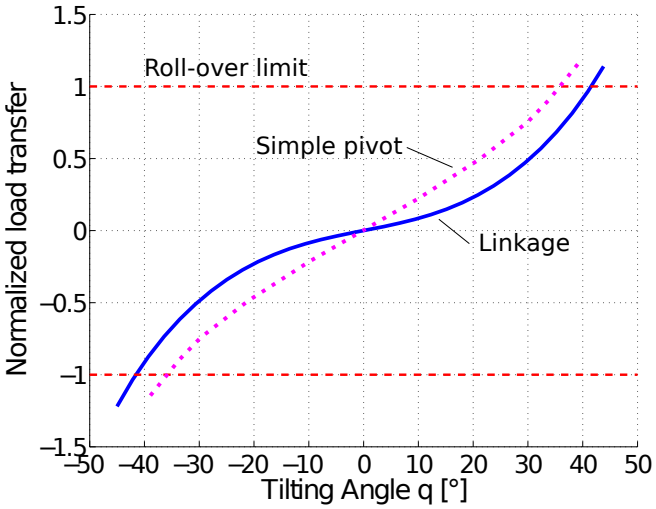

Figure 2.17: Steady turning

Chapter 3

SYNCHRONOUS ELECTRIC MACHINES

The design of synchronous reluctance machines involves a lot of variables that usually lead to unpredictable machine performance. It is difficult to achieve a proper rotor barrier design that yields satisfactory results, in terms of torque ripple, average torque, etc. Geometry optimizations could be required to find optimum solutions on the basis of some objective functions. However, a good knowledge of the machine performance behavior due to rotor geometry variables is necessary to start with the machine design, as well as to know what has to be changed for obtaining the desired performance.
The first part of the chapter deals with a novel analytical approach aimed to minimize the torque ripple of Synchronous Reluctance (REL) machines. The second part shows further investigations on the REL machine (e.g. behaviors with different number of flux-barriers per pole and with different rotor saturation levels).

The contents of this chapter have been taken from my personal scientific publications: [6,7].

The REL machine, sketched in Fig. 3.1, is used in applications in which synchronous speed, high dynamics and fault-tolerant capability are needed. The transversely laminated REL rotor exhibits a low rotor inertia, since it is formed by several flux-barriers. In addition, thanks to the synchronous operating speed, there are no rotor losses, so that only stator losses have to be taken into account.

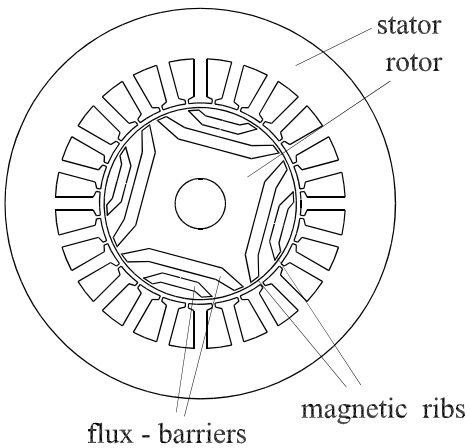

Figure 3.1: Sketch of a REL machine.

When Permanent Magnets (PMs) are inset in each rotor flux-barrier, the resulting configuration is called PM assisted synchronous reluctance (PMAREL) machine [10–12], or Interior PM (IPM) machine, depending on the quantity of flux due to the PMs, as shown in Fig. 3.2. The adoption of PMs leads to some beneficial effects: the saturation of the rotor iron bridges, the increase of the motor torque and the increase of the power factor. Sometimes the use of PMs is required in applications in which the power factor needs to be high.

The use of rotor with a high anisotropy allows Ferrite PMs to be used instead of rare-earth PMs, which became very expensive in recent years [13]. In this case, a high reluctance torque component is required.

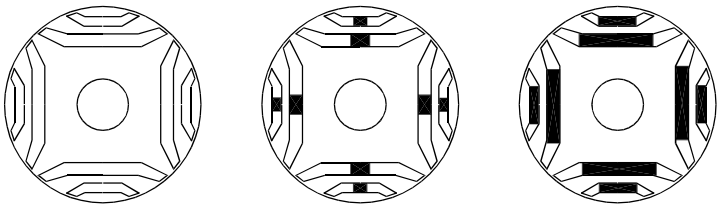

Figure 3.2: Basic configuration of synchronous motors: REL, PMAREL, and IPM motor

When dealing with synchronous REL motors, one issue is the reduction of the torque ripple, that for this kind of motors is sometimes difficult to be achieved. The interaction between the spatial harmonics of the electric loading and the rotor anisotropy (that has to be necessarily high) causes a high torque ripple that is intolerable in the most of applications. A lot of variables affect both average torque and torque ripple of REL machines, for example the stator and rotor geometry, the saturation of the rotor and stator paths, and so on [14–16].

To obtain a smooth torque, the rotor skewing is commonly adopted in PM machines, however it is not enough in synchronous reluctance machines. In addition, when PMs are used, only a stepped-skewing of the rotor is possible. The latter is split in two or more pieces and each of them is skewed with respect to the others.

This chapter deals with a new strategy to design the rotor of a REL motor so as to reduce the torque ripple. The proposed strategy combines a suitable choice of the position of the flux-barrier ends with the design of different geometries of the flux-barriers.

To the aim of reducing the torque ripple of a motor with an anisotropic rotor, an accurate analysis of the causes that generate the torque ripple is necessary before their design. Therefore, an accurate analytical model of the motor torque production based on the rotor geometry is developed. The results of this analytical model are compared and validated by those obtained by a finite element model.

Then, the analytical model is adopted to determine the dependence of torque harmonics on the geometry of the rotor flux-barrier ends. The geometrical variables are:

- the angle of the flux-barrier ends;
- possible differences between the flux-barriers under the adjacent poles;
- the length of the flux-barriers;
- the shape of the flux-barrier ends (size, distance from the other flux-barriers and from the air-gap).

3.1 REFERENCES

As far as the electric and magnetic quantities of the motor, the reference axes are shown in Fig. 3.3.

The stator reference axis corresponds to the a-phase axis. It is placed along the x-axis of the reference system. The b-phase axis leads the a-phase axis of $2\pi/3$ electrical radians, while the c-phase axis leads the a-phase axis of $4\pi/3$ electrical radians.

The positive rotor direction is in the counterclockwise direction. The rotor position is represented by the d- and the q-axis that are locked with the rotor. The d-axis is chosen along the path of the higher permeance of the rotor, and the q-phase axis leads the d-phase axis of $\pi/2$ electrical radians.

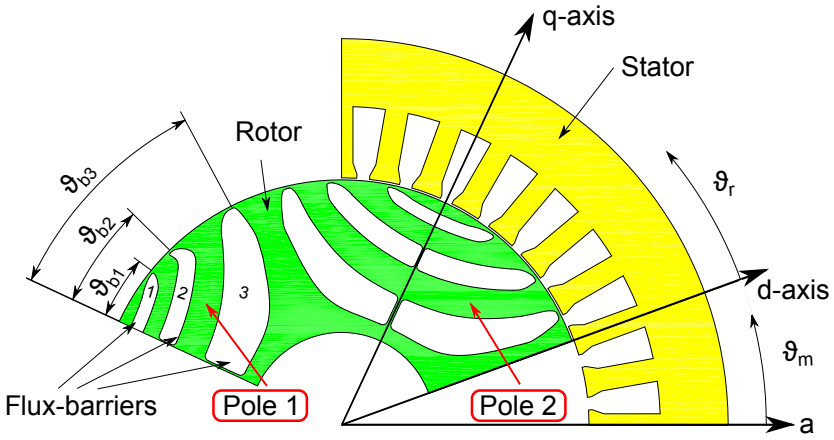

Figure 3.3: Reference used in the REL motor analysis.

3.2 ANALYTICAL MODEL OF THE STATOR

3.2.1 ELECTRICAL LOADING

A slotless stator is considered, in which the conductors within the slots are replaced by a conductive sheet, of infinitesimal thickness, placed on the inner surface of the stator. Along this sheet a distribution of a density of conductors $n_d(\vartheta_s)$ is considered, equivalent to the actual distribution of the coils within the slots, as reported in Fig. 3.4.

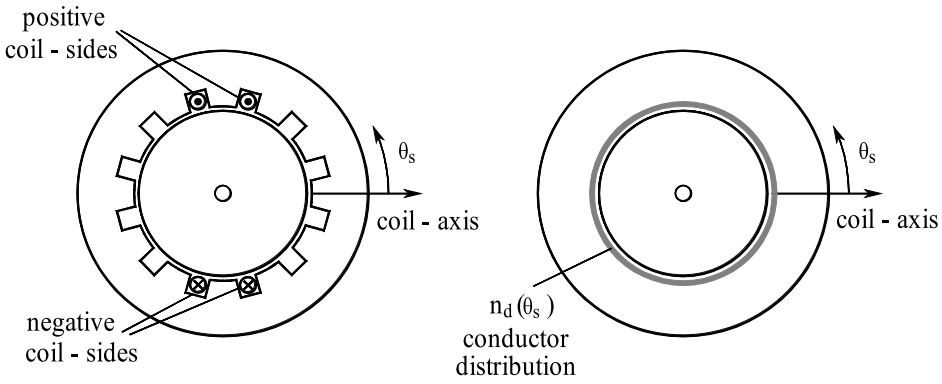

Figure 3.4: Conductor density distribution.

In the same way, a linear current density distribution along the conductive sheet can be considered when the current is carried by the actual coils. This linear current density distribution is also called electrical loading. In the stator reference frame, it is given by:

$$K_s(\vartheta_s) = \sum_{\nu} \hat{K}_\nu \sin(\nu p \vartheta_s - p\vartheta_m - \alpha_i^e) \tag{3.1}$$

$$= \sum_{\nu} \hat{K}_\nu \sin(\nu p \vartheta_s - \omega t - \alpha_i^e) \tag{3.2}$$

with

ν	the harmonic order,
$\hat{K}_\nu$	the peak value of electric loading harmonic of ν order, in (A/m),
p	the number of pole pairs,
ϑ_s	the coordinate angle (mechanical degrees), in the stator reference frame,
ϑ_m	the angular position of rotor (mechanical degrees),
α_i^e	the phase angle of the current (electrical degrees), shown in Fig. 3.5.

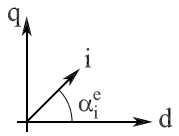

Figure 3.5: Electrical angle α_i^e of the stator current vector.

The fundamental distribution of the electric loading, according to one phase carrying current, is shown in Fig. 3.6. According to the adopted conventions, positive electric loading means that the linear current density is in the same direction of the z-axis (i.e. it goes from the paper sheet to the reader).

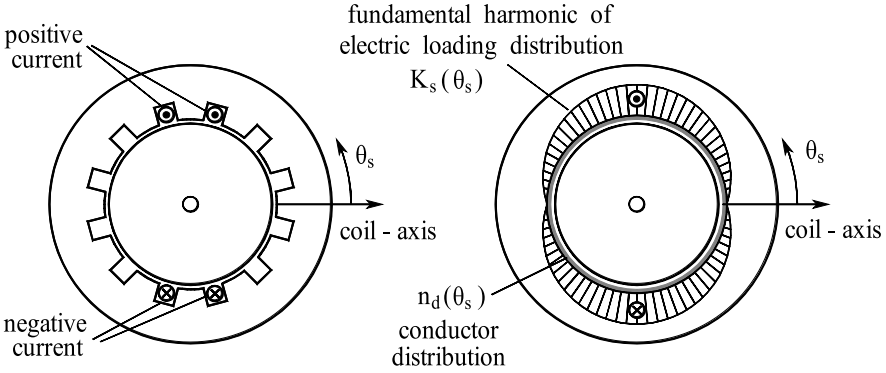

Figure 3.6: Electric loading distribution.

The symbol ν can be positive or negative (it has to be considered with sign). Adopting a standard three-phase winding, with an integer number of slot per pole per phase, only harmonics of odd order exist, non multiple of three. Then ν can be expressed as $\nu = 6k + 1$ with k integer with sign, i.e. $k = 0, \pm 1, \pm 2, ...$, so that $\nu = +1, -5, +7, -11, +13, ...$

The angle α_i^e indicates the initial phase of the (sinusoidal) current waveform. It also corresponds to the phase of the current spatial vector.

Considering only the fundamental component, some distributions of the electric loading are drawn in Table 3.1. Only the positive part of each distribution is shown. The flux lines corresponding to the stator electrical loading are also shown.

Table 3.1: Examples of the relationship between the electric loading distribution and the rotor position.

$p\vartheta_m = 0$ $\alpha_i^e = 0$ $K_s(\vartheta_s) = \hat{K}_1 \sin(p\vartheta_s)$	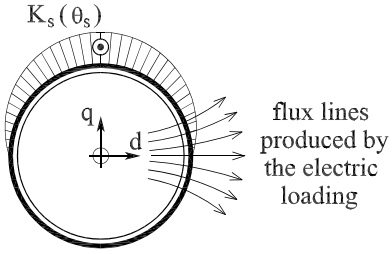
$p\vartheta_m = 0$ $\alpha_i^e > 0$ $K_s(\vartheta_s) = \hat{K}_1 \sin(p\vartheta_s - \alpha_i^e)$	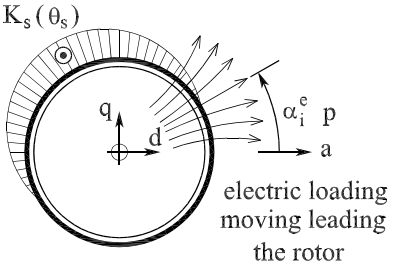
$p\vartheta_s > 0$ $\alpha_i^e = 0$ $K_s(\vartheta_s) = \hat{K}_1 \sin(p\vartheta_s - p\vartheta_m)$	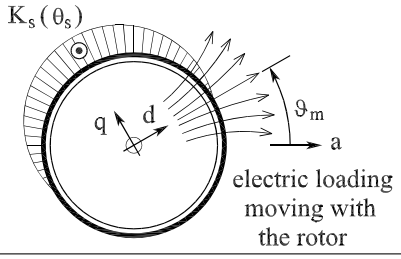

The rotor position is represented by the label d that indicates the d-axis of the rotor.

In the first case, $p\vartheta_m = 0$ means that the d-axis of the rotor is parallel to the stator reference a-phase axis. The position $\alpha_i^e = 0$ means that the distribution $K_s(\vartheta_s)$ produces flux lines parallel to the rotor d-axis.

In the second case, the rotor remains fixed to the stator ($p\vartheta_m = 0$). Conversely, the angle α_i^e is greater than zero. This means that the distribution $K_s(\vartheta_s)$ produces flux lines leading the rotor d-axis.

In the third case, the rotor moves of a mechanical angle $\vartheta_m > 0$ with respect to the stator. Since the angle α_i^e remains equal to zero, the flux lines remain parallel to the rotor d-axis. According to a constant α_i^e and to $\omega t = p\vartheta_m$, this implies that the distribution $K_s(\vartheta_s)$ moves synchronous with the rotor in order to maintain the same flux line distribution with respect to the rotor.

3.2.2 STATOR MAGNETIC POTENTIAL

In the stator reference frame the stator magnetic potential is given by:

$$U_s(\vartheta_s) = \int K_s(\vartheta_s) \frac{D}{2} d\vartheta_s \tag{3.3}$$

Since $K_s(\vartheta_s)$ is a periodic function, the integral ends can be omitted.

3.2.3 QUANTITIES IN THE ROTOR REFERENCE FRAME

It is convenient to express the quantities above in the rotor reference frame, defined by the angular coordinate ϑ_r. According to Fig. 3.3, ϑ_r is linked to the stator angular coordinate ϑ_s by:

$$\begin{aligned} p\vartheta_s &= p\vartheta_r + p\vartheta_m \\ &= p\vartheta_r + \omega t \end{aligned} \tag{3.4}$$

It is worth noticing that during steady-state operations, the rotor position is linked to the rotor speed by the relationship $p\vartheta_m = \omega t$, where $\vartheta_m = 0$ at the time $t = 0$. In the following, the angle ωt will be used to identify the rotor position.

Substituting $p\vartheta_s$ into the equations (3.1) and (3.3), they result:

$$K_s(\vartheta_r) = \sum_{\nu} \hat{K}_\nu \sin[\nu p\vartheta_r + (\nu - 1)\omega t - \alpha_i^e] \tag{3.5}$$

and

$$U_s(\vartheta_r) = \int K_s(\vartheta_r)\frac{D}{2}d\vartheta_r \tag{3.6}$$

$$= \sum_{\nu} -\frac{\hat{K}_\nu}{\nu}\frac{D}{2p}\cos[\nu p\vartheta_r + (\nu - 1)\omega t - \alpha_i^e] \tag{3.7}$$

The distribution of the magnetic potential along the stator periphery is shown in Fig. 3.7.

As a consequence of the stator magnetic potential, a magnetic flux flows in the rotor. Referring to Fig. 3.8a the rotor "island", bordered by these flux-barriers, assume a magnetic potential, proportional to the flux-barrier reluctance and the flux. The distribution of such a rotor magnetic potential is shown in Fig. 3.8a as well. Finally, the air-gap flux density can be computed as the difference between the two magnetic potentials, as in Fig. 3.8b.

In the following the study will be carried out referring separately to rotor with one and three flux-barriers per pole.

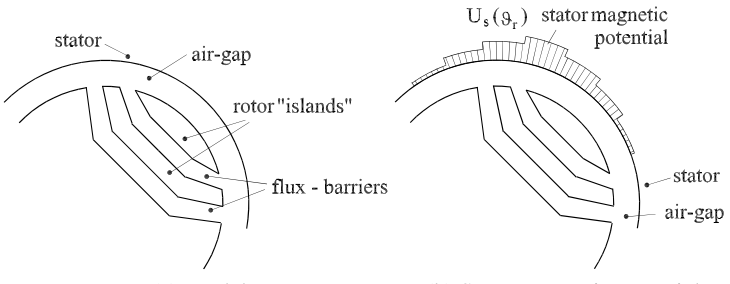

(a) Model (b) Stator magnetic potential

Figure 3.7: Magnetic potential along the stator periphery.

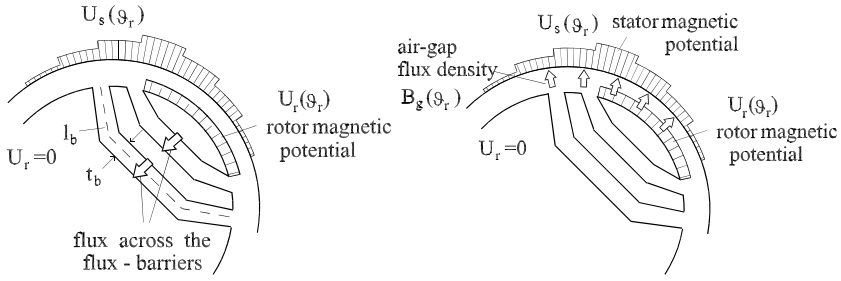

(a) Rotor magnetic potential (b) Air-gap flux density

Figure 3.8: Rotor magnetic reaction and air-gap flux density.

3.3 ROTOR WITH ONE FLUX-BARRIER PER POLE

3.3.1 ROTOR MAGNETIC POTENTIAL AND AIR-GAP FLUX DENSITY

Fig. 3.9 shows the geometrical reference of the flux-barrier used in the analysis. The d-axis is considered in the classical way used for the synchronous reluctance motor, along which the permeance of the magnetic path is maximum.

The symbol ϑ_b indicates the half-angle of the flux-barrier, expressed in mechanical degrees.

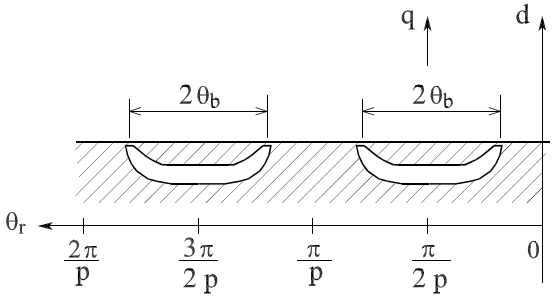

Figure 3.9: Geometrical references of the flux-barriers.

Neglecting the magnetic voltage drop in the stator iron path, the air-gap flux density distribution is given by:

$$B_g(\vartheta_r) = \mu_0 \frac{-U_s(\vartheta_r) + U_r(\vartheta_r)}{g} \tag{3.8}$$

The magnetic potential of the rotor $U_r(\vartheta_r)$ can be considered constant in each magnetic "island" bordered by the flux-barrier and the air-gap (labelled as U_{r1}), and null elsewhere.

From the air-gap flux density distribution (3.8), the magnetic flux crossing the flux-barrier results in:

$$\begin{aligned}\phi_b &= \int_{\frac{\pi}{2p}-\vartheta_b}^{\frac{\pi}{2p}+\vartheta_b} -B_g(\vartheta_r) L_{stk} \frac{D}{2} d\vartheta_r \\ &= \mu_0 \frac{L_{stk} D}{2g} \left[\int_{\frac{\pi}{2p}-\vartheta_b}^{\frac{\pi}{2p}+\vartheta_b} U_s(\vartheta_r) d\vartheta_r - 2\vartheta_b U_{r1} \right]\end{aligned} \tag{3.9}$$

where U_{r1} has been brought out by the integral sign, since it is constant in the integration path.

The magnetic reluctance of the flux-barrier is given by:

$$R_b = \frac{t_b}{\mu_0 L_{stk} l_b} \tag{3.10}$$

The length of the flux-barrier l_b can be approximated as the distance between the two extremes along the stator bore periphery, i.e. $l_b \simeq \vartheta_b D$, thus the magnetic reluctance (3.10) becomes:

$$R_b \simeq \frac{t_b}{\mu_0 L_{stk} \vartheta_b D} \tag{3.11}$$

The rotor magnetic potential can be computed as the flux crossing the flux-barrier times its reluctance, thus U_{r1} can be expressed as a function of $U_s(\vartheta_r)$, as:

$$\begin{aligned} U_{r1} &= \phi_b R_b \\ &= \mu_0 \frac{L_{stk} D}{2g} \left[\int_{\frac{\pi}{2p}-\vartheta_b}^{\frac{\pi}{2p}+\vartheta_b} -U_s(\vartheta_r) d\vartheta_r + 2\vartheta_b U_{r1} \right] \frac{t_b}{\mu_0 L_{stk} l_b} \\ &= \frac{D}{2g} \frac{t_b}{l_b} \left[\int_{\frac{\pi}{2p}-\vartheta_b}^{\frac{\pi}{2p}+\vartheta_b} -U_s(\vartheta_r) d\vartheta_r + 2\vartheta_b U_{r1} \right] \end{aligned} \tag{3.12}$$

from which U_{r1} can be expressed as:

$$U_{r1} \left(1 + \frac{D}{2g} \frac{t_b}{l_b} 2\vartheta_b \right) = \frac{D}{2g} \frac{t_b}{l_b} \int_{\frac{\pi}{2p}-\vartheta_b}^{\frac{\pi}{2p}+\vartheta_b} U_s(\vartheta_r) d\vartheta_r \tag{3.13}$$

To the aim of simplifying the expression above, the following term is stated:

$$a = \frac{\frac{D}{2g} \frac{t_b}{l_b}}{1 + \frac{D}{2g} \frac{t_b}{l_b} 2\vartheta_b} \tag{3.14}$$

This dimensionless coefficient is a function of the rotor geometry only, in fact it depends on the bore diameter D, the air-gap thickness g, the barrier thickness t_b, the barrier length l_b, and the barrier half-angle ϑ_b.

With the approximation $l_b \simeq \vartheta_b D$, the coefficient a becomes:

$$a \simeq \frac{\frac{t_b}{2g\vartheta_b}}{1 + \frac{t_b}{g}} \tag{3.15}$$

Thus U_{r1} can be rewritten as:

$$
\begin{aligned}
U_{r1} &= a \int_{\frac{\pi}{2p}-\vartheta_b}^{\frac{\pi}{2p}+\vartheta_b} U_s(\vartheta_r) d\vartheta_r \\
&= a \sum_{\nu} -\frac{\hat{K}_\nu}{\nu} \frac{D}{2p} \frac{1}{\nu p} \sin\left[\nu p \vartheta_r + (\nu-1)\omega t - \alpha_i^e\right] \Bigg|_{\frac{\pi}{2p}-\vartheta_b}^{\frac{\pi}{2p}+\vartheta_b} \\
&= -aD \sum_{\nu} \frac{\hat{K}_\nu}{(\nu p)^2} \cos(\lambda_\nu) \sin(\nu p \vartheta_b)
\end{aligned} \tag{3.16}
$$

where:

$$
\lambda_\nu = \frac{\nu\pi}{2} + (\nu-1)\omega t - \alpha_i^e \tag{3.17}
$$

With the assumption of harmonics of odd order only, the addendum $\nu\pi$ produces a change in the sign of the magnetic potential, as shown in Fig. 3.10. It results to be of opposite sign under every successive pole.

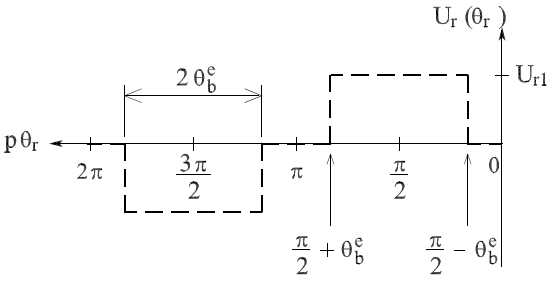

Figure 3.10: Rotor magnetic potential distribution.

3.3.2 TORQUE COMPUTATION

The torque is obtained by integrating the Lorentz's force density $B_g(\vartheta_r)K_s(\vartheta_r)$ along the air-gap surface, and multiplying the result by the radius $D/2$. By means of the convention defined before, see Fig. 3.3, it is

$$
\begin{aligned}
\tau_m &= -\frac{D}{2} \int_0^{2\pi} B_g(\vartheta_r) K_s(\vartheta_r) \frac{DL_{stk}}{2} d\vartheta_r \\
&= -\frac{D}{2} \int_0^{2\pi} \mu_0 \frac{-U_s(\vartheta_r) + U_r}{g} K_s(\vartheta_r) \frac{DL_{stk}}{2} d\vartheta_r \\
&= \frac{\mu_0}{g} \frac{D^2 L_{stk}}{4} \left[\underbrace{\int_0^{2\pi} U_s(\vartheta_r) K_s(\vartheta_r) d\vartheta_r}_{A} + \underbrace{\int_0^{2\pi} -U_r(\vartheta_r) K_s(\vartheta_r) d\vartheta_r}_{B} \right]
\end{aligned} \tag{3.18}
$$

The first integral of (3.18), i.e. the term A, is null since the Fourier series expansions of $U_s(\vartheta_r)$ and $K_s(\vartheta_r)$ are orthogonal functions. Thus the integral in a period of their product is null [1].

[1] In fact

$$
\int_0^{2\pi} \left[\cos(p\vartheta_r + \lambda_1) + \cos(5p\vartheta_r + \lambda_5) + \ldots\right] \left[\sin(p\vartheta_r + \lambda_1) - \sin(5p\vartheta_r + \lambda_5) + \ldots\right] d\vartheta_r = 0
$$

Then, only the second integral of (3.18), labelled B, will be considered. The torque results in:

$$\tau_m = \frac{\mu_0}{g}\frac{D^2 L}{4}\int_0^{2\pi} -U_r(\vartheta_r)K_s(\vartheta_r)d\vartheta_r \tag{3.19}$$

It is worth noticing that:

- $U_r(\vartheta_r)$ is a function piece-wise defined; it assumes a value different from zero only in the intervals $(\pi/2 - \vartheta_b^e, \pi/2 + \vartheta_b^e)$ and $(3\pi/2 - \vartheta_b^e, 3\pi/2 + \vartheta_b^e)$ and null elsewhere (see Fig. 3.10);
- $U_r(\vartheta_r)$ has opposite values under every other pole (this is true with the assumption of harmonics of odd order only);
- thanks to the motor symmetry, only two poles can be considered in the computation, and the quantities of the whole system are achieved by multiplying the result of the computation by the number of pole pairs p.

After some manipulations the torque (3.18) becomes:

$$\tau_m = \frac{\mu_0}{g}\frac{D^2 L_{stk}}{4}U_{r1}(-2p)\int_{\frac{\pi}{2p}-\vartheta_b}^{\frac{\pi}{2p}+\vartheta_b} K_s(\vartheta_r)d\vartheta_r \tag{3.20}$$

Finally, substituting the relationships of the electrical loading (3.5) and the rotor magnetic potential (3.16), the motor torque becomes:

$$\tau_m = a\mu_0\frac{D^3 L_{stk}}{g}\sum_\nu \frac{\hat{K}_\nu}{(\nu p)^2}\ \cos\lambda_\nu \sin(\nu p\vartheta_b)\sum_\xi \frac{\hat{K}_\xi}{\xi}\ \sin\lambda_\xi \sin(\xi p\vartheta_b) \tag{3.21}$$

In (3.21) the parameters ν and ξ are used in order to avoid to confuse the harmonic components of the two series expansions.

It is worth noticing that only the fundamental terms give rise to a constant torque, while all the others cause a time-varying torque. Thus the mean torque is due only to the two fundamental terms, while the other terms cause a torque ripple.

3.4 ROTOR WITH THREE FLUX-BARRIERS PER POLE

For the study of the rotor with three flux-barriers per pole, the same notation used for the rotor with one and two flux-barrier per pole will be used. In addition the subscript "1" will be used for the inner flux-barrier, the subscript "2" will be used for the middle flux-barrier and the subscript "3" will be used for the outer flux-barrier.

The electrical loading and the stator magnetic potential are given by (3.5) and (3.6) respectively.

It is convenient to consider the magnetic lumped-parameter network shown in Fig. 3.11. The reluctances R_{b1}, R_{b2} and R_{b3} are given by (3.10), with adequate subscript.

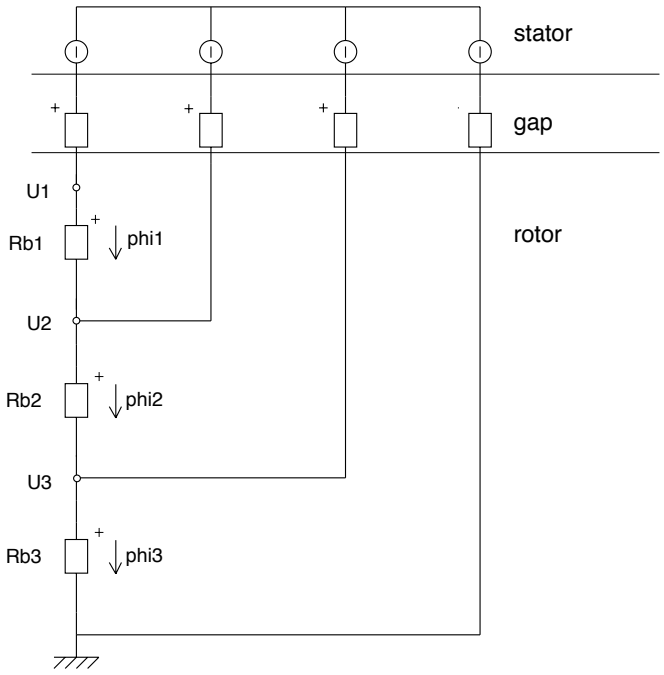

Figure 3.11: Magnetic lumped-parameter network for a three flux-barriers per pole rotor.

3.4.1 ROTOR MAGNETIC POTENTIALS

The magnetic potential of the rotor "island" bordered by the inner flux-barrier is:

$$\begin{aligned} U_{r1} &= \phi_{b1} R_{b1} + U_{r2} \\ &= a \int_{\frac{\pi}{2p}-\vartheta_{b1}}^{\frac{\pi}{2p}+\vartheta_{b1}} U_s d\vartheta_r + b\, U_{r2} \end{aligned} \tag{3.22}$$

The coefficient a is the one stated in (3.14) whereas b is:

$$b = \frac{1}{1 + \dfrac{D}{2g}\dfrac{t_{b1}}{l_{b1}} 2\vartheta_{b1}} \tag{3.23}$$

The magnetic potential of the rotor "island" bordered by the middle flux-barrier is computed by means of the flux crossing through the flux-barrier itself.
By considering:

$$\phi_{b2} = \frac{U_{r1} - U_{r2}}{t_{b1}} \mu_0 L l_{b1} \tag{3.24}$$

$$B_g = \mu_0 \frac{(U_s - U_{r2})}{g} \tag{3.25}$$

and by defining the terms:

$$den = \left(1 - (b-1)\frac{l_{b1}}{t_{b1}}\frac{t_{b2}}{l_{b2}} + \frac{D}{g}\frac{t_{b2}}{l_{b2}}(\vartheta_{b2} - \vartheta_{b1})\right) \tag{3.26}$$

$$c = a\frac{\frac{l_{b1}}{t_{b1}}\frac{t_{b2}}{l_{b2}}}{den} \tag{3.27}$$

$$d = \frac{\frac{D}{2g}\frac{t_{b2}}{l_{b2}}}{den} \tag{3.28}$$

$$z = \frac{1}{den} \tag{3.29}$$

the magnetic potential U_{r2} is:

$$\begin{aligned} U_{r2} &= \phi_{b2}R_{b2} + U_{r3} \\ &= c\int_{\frac{\pi}{2p}-\vartheta_{b1}}^{\frac{\pi}{2p}+\vartheta_{b1}} U_s d\vartheta_r + d\left(\int_{\frac{\pi}{2p}-\vartheta_{b2}}^{\frac{\pi}{2p}-\vartheta_{b1}} U_s d\vartheta_r + \int_{\frac{\pi}{2p}+\vartheta_{b1}}^{\frac{\pi}{2p}+\vartheta_{b2}} U_s d\vartheta_r\right) + zU_{r3} \end{aligned} \tag{3.30}$$

The magnetic potential of the rotor "island" bordered by the outer flux-barrier is computed by means of the flux crossing through the flux-barrier itself.
By considering:

$$\phi_{b3} = \frac{U_{r2} - U_{r3}}{t_{b2}}\mu_0 L l_{b2} \tag{3.31}$$

$$B_g = \mu_0\frac{(U_s - U_{r3})}{g} \tag{3.32}$$

and by defining the terms:

$$den2 = \left(1 - (z-1)\frac{l_{b2}}{t_{b2}}\frac{t_{b3}}{l_{b3}} + \frac{D}{g}\frac{t_{b3}}{l_{b3}}(\vartheta_{b3} - \vartheta_{b2})\right) \tag{3.33}$$

$$m = c\frac{\frac{l_{b2}}{t_{b2}}\frac{t_{b3}}{l_{b3}}}{den2} \tag{3.34}$$

$$n = d\frac{\frac{l_{b2}}{t_{b2}}\frac{t_{b3}}{l_{b3}}}{den2} \tag{3.35}$$

$$q = \frac{\frac{D}{2g}\frac{t_{b3}}{l_{b3}}}{den2} \tag{3.36}$$

the magnetic potential U_{r3} is:

$$\begin{aligned} U_{r3} &= \phi_{b3}R_{b3} \\ &= m\int_{\frac{\pi}{2p}-\vartheta_{b1}}^{\frac{\pi}{2p}+\vartheta_{b1}} U_s d\vartheta_r \qquad +n\left(\int_{\frac{\pi}{2p}-\vartheta_{b2}}^{\frac{\pi}{2p}-\vartheta_{b1}} U_s d\vartheta_r + \int_{\frac{\pi}{2p}+\vartheta_{b1}}^{\frac{\pi}{2p}+\vartheta_{b2}} U_s d\vartheta_r\right) \\ &\qquad\qquad +q\left(\int_{\frac{\pi}{2p}-\vartheta_{b3}}^{\frac{\pi}{2p}-\vartheta_{b2}} U_s d\vartheta_r + \int_{\frac{\pi}{2p}+\vartheta_{b2}}^{\frac{\pi}{2p}+\vartheta_{b3}} U_s d\vartheta_r\right) \end{aligned} \tag{3.37}$$

After some manipulations the rotor magnetic potential U_{r1}, U_{r2} and U_{r3} results in:

$$U_{r1} = -\sum_{\nu} \frac{\hat{K}_\nu}{(\nu p)^2} D\rho_1 \cos\lambda_\nu \tag{3.38}$$

$$U_{r2} = -\sum_{\nu} \frac{\hat{K}_\nu}{(\nu p)^2} D\rho_2 \cos\lambda_\nu \tag{3.39}$$

$$U_{r3} = -\sum_{\nu} \frac{\hat{K}_\nu}{(\nu p)^2} D\rho_3 \cos\lambda_\nu \tag{3.40}$$

where:

$$\begin{aligned}\rho_1 =& \Big[(a + b(c - d + z(m - n)))\sin(\nu p\vartheta_{b1}) + \\ &+ (b(d + z(n - q)))\sin(\nu p\vartheta_{b2}) + bzq\sin(\nu p\vartheta_{b2})\Big]\end{aligned} \tag{3.41}$$

$$\begin{aligned}\rho_2 =& \Big[(c - d + z(m - n))\sin(\nu p\vartheta_{b1}) + \\ &+ (d + z(n - q))\sin(\nu p\vartheta_{b2}) + qz\sin(\nu p\vartheta_{b3})\Big]\end{aligned} \tag{3.42}$$

$$\rho_3 = [(m - n)\sin(\nu p\vartheta_{b1}) + (n - q)\sin(\nu p\vartheta_{b2}) + q\sin(\nu p\vartheta_{b3})] \tag{3.43}$$

3.4.2 TORQUE COMPUTATION

Similarly to the rotor with one flux-barrier per pole, the motor torque is computed as:

$$\begin{aligned}\tau_m &= \frac{D}{2}\int_0^{2\pi} B_g(\vartheta_r)K_s(\vartheta_r)\frac{D}{2}Ld\vartheta_r = \frac{D^2}{4}L2p\int_0^{\pi/p} B_g(\vartheta_r)K_s(\vartheta_r)d\vartheta_r \\ &= K_{tau}\sum_{\nu}\frac{\hat{K}_\nu}{\nu^2}\cos\lambda_\nu\Big[\rho_1\sum_{\xi}\frac{\hat{K}_\xi}{\xi}\sin\lambda_\xi\sin(\xi p\vartheta_{b1}) + \\ &+ \rho_2\sum_{\xi}\frac{\hat{K}_\xi}{\xi}\sin\lambda_\xi\left[\sin(\xi p\vartheta_{b2}) - \sin(\xi p\vartheta_{b1})\right] \\ &+ \rho_3\sum_{\xi}\frac{\hat{K}_\xi}{\xi}\sin\lambda_\xi\left[\sin(\xi p\vartheta_{b3}) - \sin(\xi p\vartheta_{b2})\right]\Big]\end{aligned} \tag{3.44}$$

where:

$$K_{tau} = -\frac{2hD}{p^2} = \mu_0\frac{D^3L}{g}\frac{1}{p^2} \tag{3.45}$$

3.5 VALIDATION OF THE ANALYTICAL MODEL WITH THREE FLUX-BARRIERS PER POLE

In this thesis only the model with three flux-barriers per pole will be validated by means of Finite Elements (FE) analysis. The analytical models with one and two (not presented in this thesis) flux-barriers per pole have been previously presented in [17–19].

The reference REL motor is characterized by the data reported in Table 3.2.

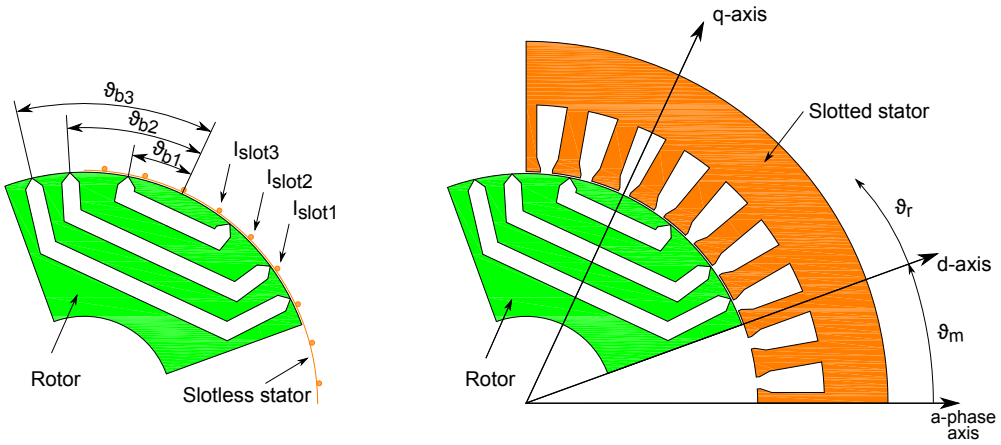

(a) Slotless model (b) Slotted model

Figure 3.12: Reference used in the REL motor analysis.

Table 3.2: Geometrical parameters of the considered REL machine

Specification	Symbol	Value	Unit
Pole pairs	p	2	
Stator slots	Q_s	36	
Stator outer diameter	D_e	150	mm
Stator inner diameter	D	96	mm
Stack length	L_{stk}	70	mm
Air gap thickness	g	0.4	mm

A first FE model, Fig. 3.12a, has been developed in order to satisfy all the assumptions stated in the analytical formulation, substituting the stator slots with an equivalent distribution of Q current points. This is to eliminate the effect of the stator slotting and to match better the hypothesis of the analytical model. This FE model has been used to verify the matching between the results obtained by means of numerical and FE simulations. The results are shown in Figs. 3.13a and 3.13b, respectively. These two curves present the torque for different rotor positions. The torque obtained in 3.13b matches that predicted by the analytical model. In fact, the two curves present the same peak-to-peak torque ripple ($\Delta\tau$), period and shape. Only the average value (τ_{avg}) is a little bit lower in the FE results due to the finite iron permeability.

With the aim of evaluating the effect of rotor saturation, the model of Fig. 3.12a has been adopted assuming nonlinear iron. Fig. 3.13c shows the torque obtained in this case by means of FE simulations. The effect of the introduction of saturation is that $\Delta\tau$ increases of 27% and τ_{avg} decreases of 29% respect to the case in Fig. 3.13b. The shape and the period of the waveform remain similar to the case in Fig. 3.13b.
In order to consider the effect of a slotted stator, a second FE model has been developed, see Fig. 3.12b, introducing the actual stator. Linear iron is adopted in both stator and rotor. The results are shown in Fig. 3.13d. The slotting leads to a $\Delta\tau$ of 3.27 Nm which is equivalent to 51% more than in the case in Fig. 3.13b whereas the τ_{avg} is less than 27%. A slotted stator affects the $\Delta\tau$ more than the rotor saturation, changing the waveform shape, but maintaining

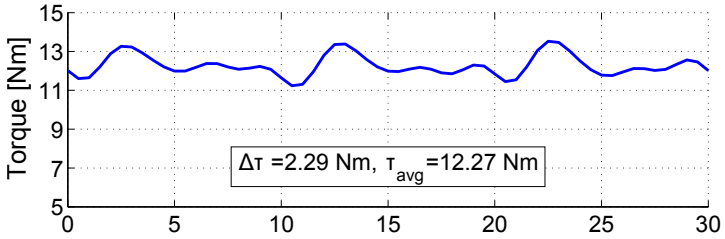

(a) Analytical results

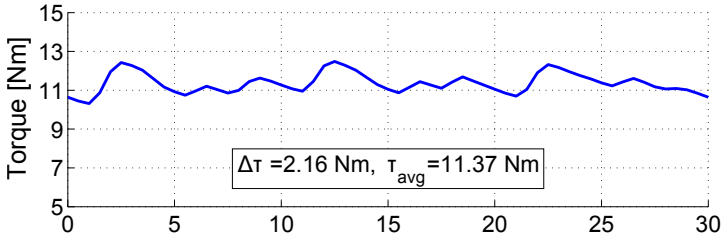

(b) FEM results: only linear rotor

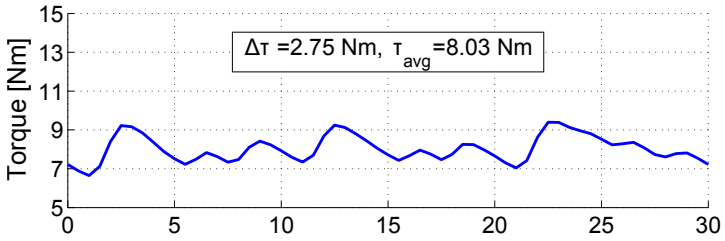

(c) FEM results: only nonlinear rotor

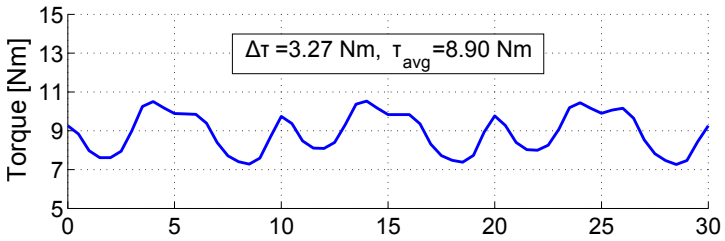

(d) FEM results: linear rotor and stator

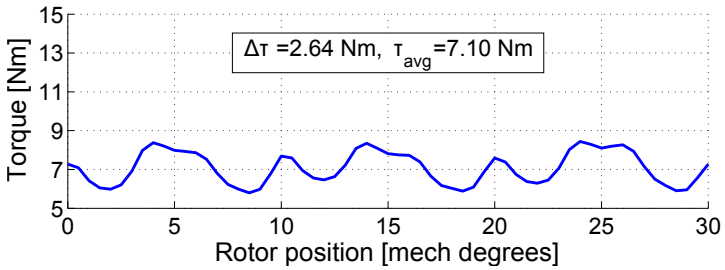

(e) FEM results: nonlinear rotor and stator

Figure 3.13: Validation of the analytical model by means of FEM analysis.

the period, respect to the cases in Fig. 3.13b and in Fig. 3.13c. In order to consider such an effect on the torque ripple, a proper stator slot geometry should be made. Since the stator geometry is a constraint, this issue has not been taken into account in this study.
Finally, the last graph of Fig. 3.13 shows the torque obtained considering nonlinear stator and rotor in the FE model in Fig. 3.12b. The effects of the saturation and of the slotting are a

reduction of τ_{avg} that becomes 38% less than the case in Fig. 3.13b, and an increase of $\Delta\tau$, becoming 22% higher than the case in Fig. 3.13b.

Table 3.3 reports a summary of these results. It is worth noticing that the effects of the saturation and the stator slotting together are beneficial on the torque ripple, compared to cases in Fig. 3.13c and in Fig. 3.13d in which these effects are independent. In any case, the analytical model yields a satisfactory prediction of the torque ripple behavior.

Table 3.3: Analytical model validation

Case	$\Delta\tau$	τ_{avg}	Assumptions
a)	100%	110%	Analytical
b)	100%	100%	FE slotless, linear rotor
c)	127%	71%	FE slotless, nonlinear rotor
d)	151%	73%	FE slotted, linear stator and rotor
e)	122%	62%	FE slotted, nonlinear stator and rotor

3.6 ROTORS WITH DIFFERENT NUMBER OF BARRIERS PER POLE: INVESTIGATION ON $\Delta\tau$ AND τ_{avg}

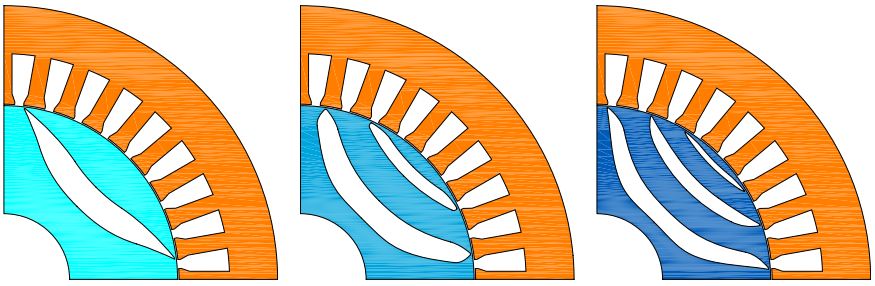

(a) 1 flux-barrier per pole (b) 2 flux-barriers per pole (c) 3 flux-barriers per pole

Figure 3.14: REL motor layouts with different number of flux-barriers per pole.

The purpose of this Section is to analyze the variation of $\Delta\tau$ and τ_{avg} with rotors composed of one, two and three flux-barriers per pole (see Fig. 3.14), maintaining the same stator arrangement including the three-phase winding. By means of the analytical model of such configurations a proper design has been carried out with the aim of reducing $\Delta\tau$ as much as possible. For each solution the shape and the angles of the flux-barrier ends have been optimized. The layouts of these machines are presented in Fig. 3.14.
Fig. 3.15 collects the FE results obtained with the three rotor configurations presented above. Fig. 3.14a shows the torque for different rotor positions produced by the rotor with one flux-barrier per pole. This configuration exhibits the highest $\Delta\tau$ (52% respect to the average torque) and the lowest τ_{avg} ($5.93\ Nm$). Fig. 3.14b reports the torque produced by the rotor with two flux-barriers per pole. These results confirm that the two barriers configuration allows to reduce the $\Delta\tau$ and increase the τ_{avg}. In fact, the $\Delta\tau$ is 33% of the average torque, that is about $7.1\ Nm$. Finally, Fig. 3.15c shows that the rotor with three flux-barriers per pole yields the lowest $\Delta\tau$ (20%) with the highest τ_{avg} ($7.19\ Nm$).

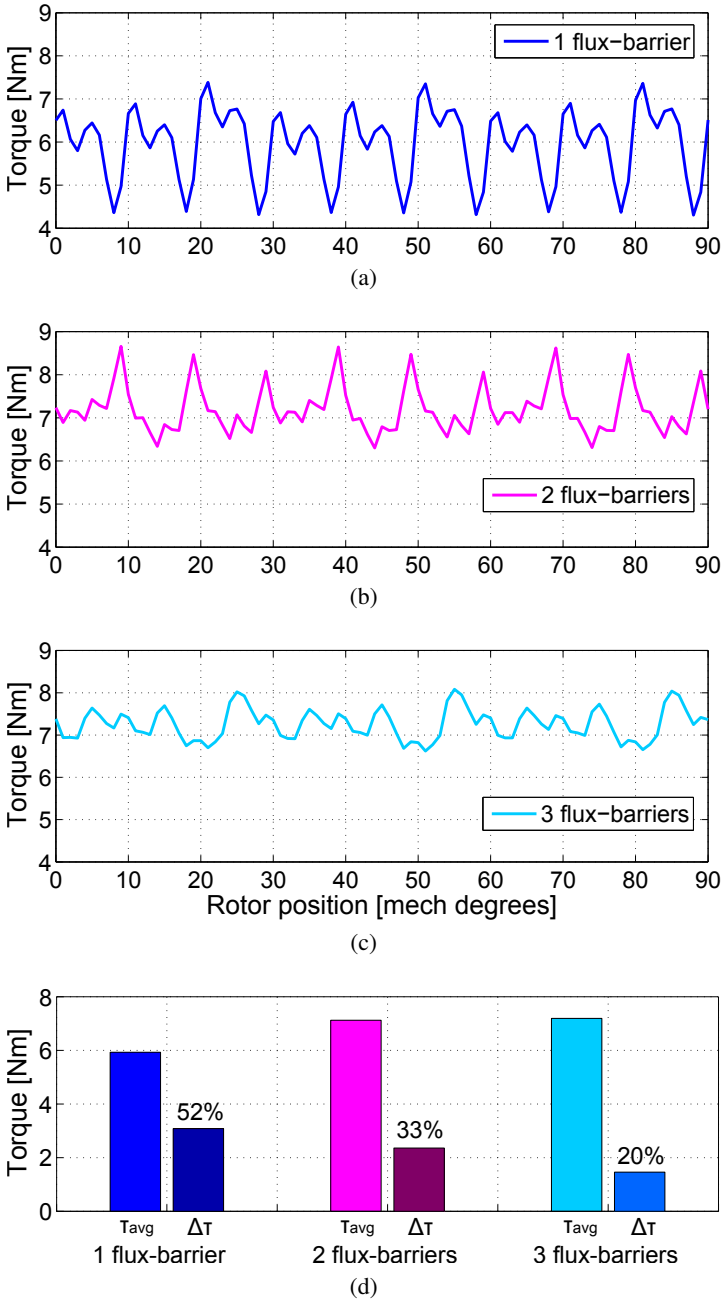

Figure 3.15: Torque comparison among rotors with 1, 2 and 3 flux-barriers per pole.

3.7 FURTHER IMPROVEMENTS BY MEANS OF THE MACHAON CONFIGURATION

As shown in Section 3.6, the solution with three flux-barrier per pole gives more benefits in terms of $\Delta\tau$ and τ_{avg}. It has been chosen as reference for further improvements. The analytical model presented in Section 3.4 is used to obtain some design maps that show the torque ripple (according to different harmonic orders) for various angles of the flux-barrier ends. Such maps allow the best design solution to be chosen.

The improvement in terms of maximum τ_{avg} and minimum $\Delta\tau$ has been carried out by means of the maps presented in Figs. 3.16 and 3.17. These maps collect the amplitudes (in Nm) estimated for the 18^{th} harmonic (that is, the slot harmonic of order Q_s/p) for different

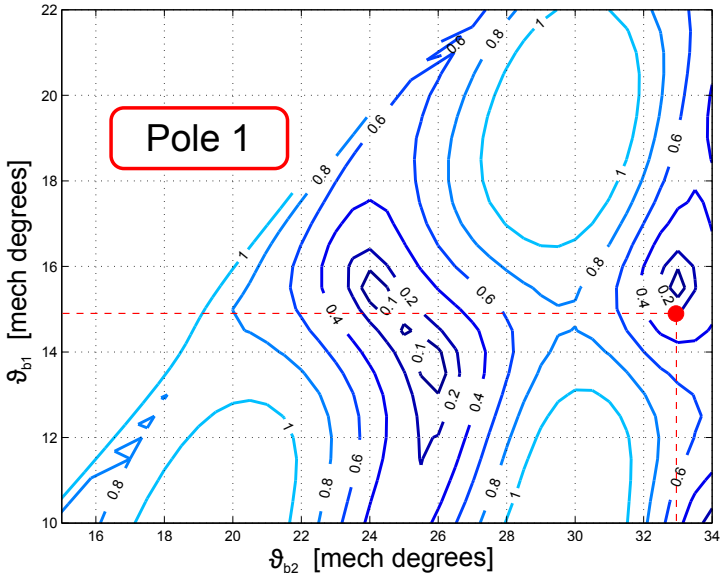

Figure 3.16: Torque ripple for the 18^{th} harmonic, $\theta_{b3} = 39\ mech\ deg$, solution A.

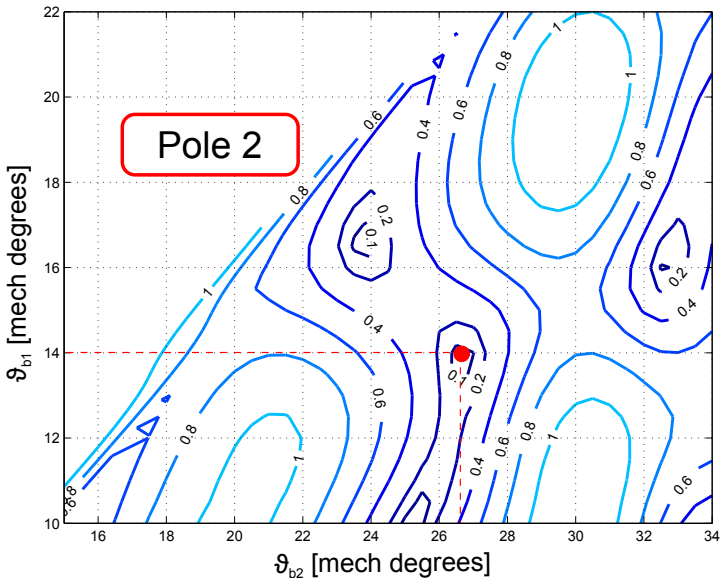

Figure 3.17: Torque ripple for the 18^{th} harmonic, $\theta_{b3} = 41.4\ mech\ deg$, solution B.

angles ϑ_{b1} and ϑ_{b2}. Since the rotor has three flux-barriers per pole, the map in Fig. 3.16 is obtained for fixed values of ϑ_{b3}. From the analytical model, two minimum $\Delta\tau$ conditions have been found.

One of them has been obtained with $\vartheta_{b3} = 39\ mech\ deg$. Let's refer to this solution as *solution A*. The other has been shown in Section 3.4 and it has been obtained with $\vartheta_{b3} = 41.4\ mech\ deg$. Let's refer to this solution as *solution B*. These angles minimize the torque ripple with the considered configuration of stator and rotor (i.e., same number of poles, slots and flux–barriers per pole). The difference between these two configurations is a slight decrease of both τ_{avg} and $\Delta\tau$ for the former solution (*solution A*).

A "Machaon" configuration is composed of two poles of the first type and two other poles of another type, [17, 20]. Fig. 3.18 shows the layouts of the machines designed for the *solution*

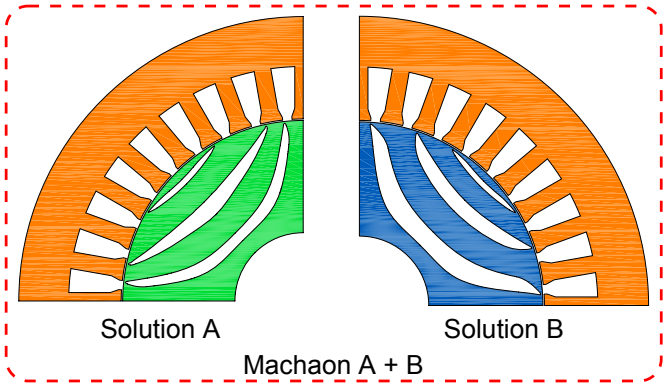

Figure 3.18: Solution A and B.

A and *B*. This solution combines two arrangements in one rotor with their advantages.

The minimum $\Delta\tau$ can be obtained minimizing the contribution of the slot harmonic, that is, 18^{th} harmonic, that in this case gives the highest contribution on $\Delta\tau$.

In our case the *solution A* has been improved by means of the map of Fig. 3.16 in which the optimal couple of angles ϑ_{b1} and ϑ_{b2} has been chosen to guarantee the lowest $\Delta\tau$. The same approach has been used for the *solution B* by means of the map of Fig. 3.17. It is verified that the the lowest $\Delta\tau$ achieved with the maps of the 18^{th} harmonic is in agreement with the absolute minimum due to all the harmonics.

Fig. 3.19 collects the FE results of the configurations a, b and *A+B* (Machaon). The *solution A* presents the lowest $\Delta\tau$ (12% respect to the average torque) and low τ_{avg} (6.8 Nm). The *Solution B* is characterized by $\Delta\tau = 20\%$ and $\tau_{avg} = 7.19\ Nm$. Combining these two solutions a Machaon (a+b) arrangement has been obtained gaining a $\Delta\tau = 15\%$ and a $\tau_{avg} = 7.12\ Nm$. The benefit of such a configuration is also highlighted in the harmonics spectrum of the torque that has been calculated for different rotor positions (mech deg) and it is shown in Fig. 3.19.

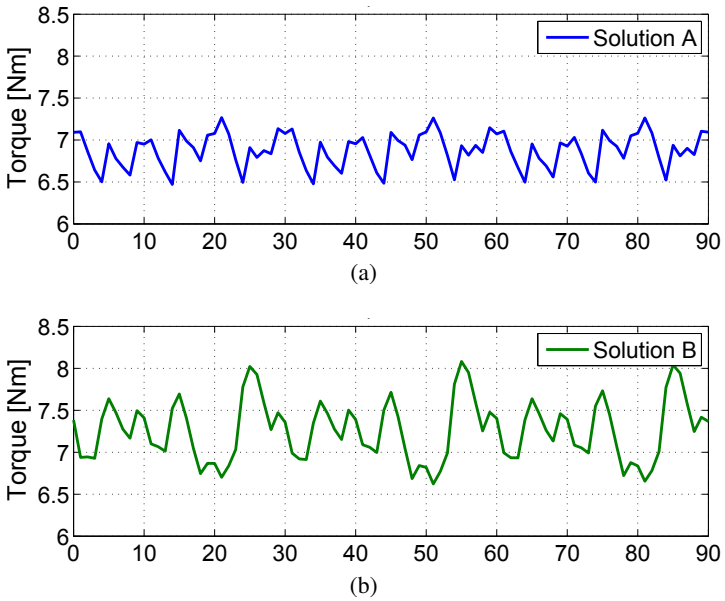

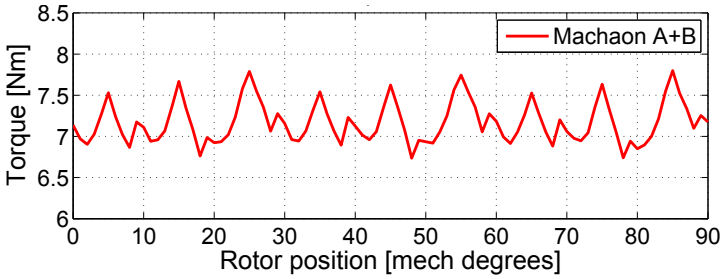

(c)

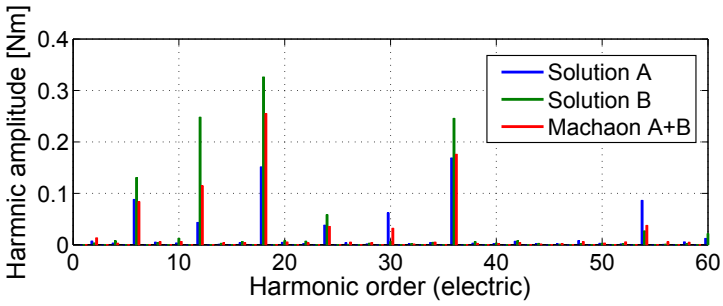

(d)

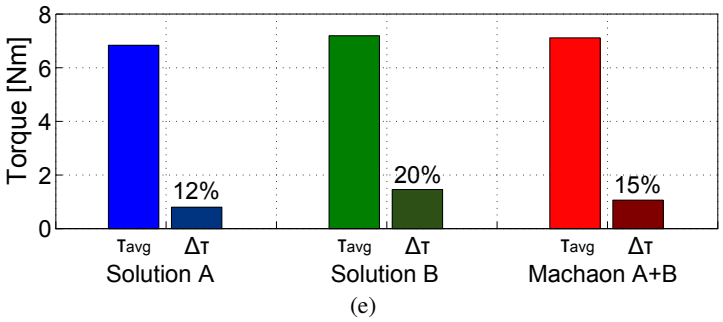

(e)

Figure 3.19: Torque improvement by means of the Machaon configuration.

3.8 SATURATION EFFECTS

This section investigates the effect of different levels of saturation of the magnetic rotor path, comparing the performance of some synchronous reluctance machines. The effect of the insertion of permanent magnets is also investigated. The comparison has been carried out on the basis of FE analysis, considering average torque, torque ripple, power factor, torque and power versus speed curves and efficiency. A prototype has been tested to compare the simulation results with the experimental measurements.

Iron saturation affects the rotor position detection by means of high frequency signal injection [21]. Sometimes such effects are not predictable, and an optimization is required so as to determine the optimal rotor geometry. A proper machine design should consider these effects and their impact on the machine performance, to get a good initial machine design. Effects of the rotor saturation on the machine performance have not been deeply investigated yet.

Table 3.4 summarizes the main parameters of the two REL motors considered in the following. Simulations have been performed using two different four-poles rotors designed with

Table 3.4: Geometrical parameters of the considered synchronous REL machines

Specification	Symbol	REL 1	REL 2	Unit
Pole number	$2p$	4	4	
Stator slots	Q_s	36	36	
Stator outer diameter	D_{es}	150	200	mm
Stator inner diameter	D_{is}	95	125	mm
Stack length	L_{stk}	70	40	mm
Air gap thickness	g	0.35	0.35	mm

different geometries per pole [17,20]. Every rotor has three flux-barriers per pole and different angles of the flux-barrier ends. These angles have been optimized so as to minimize the torque ripple. The "Machaon" configuration is adopted. In order to take into account the thickness of the flux-barriers, from which depends the level of saturation of the machine, a coefficient k_{air} has been defined:

$$k_{air} = \frac{\sum_i t_{bi}}{(D_r - D_{sh})/2} \tag{3.46}$$

where, the terms t_{bi} are the thicknesses of the flux-barriers, D_r is the external rotor diameter and D_{sh} is the shaft diameter, as represented in Fig. 3.20

Referring to Fig. 3.21 the rotor on the top is formed by flux-barriers with $k_{air} = 0.35$ and the rotor on the bottom by $k_{air} = 0.65$. The angles of the flux-barrier ends have been fixed to 14, 20 and 40 deg for the first pole and 14, 28.5 and 40 deg for the second pole, for both the configurations.

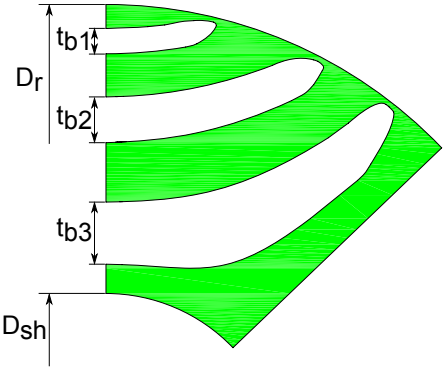

Figure 3.20: Explanation of the coefficient k_{air}.

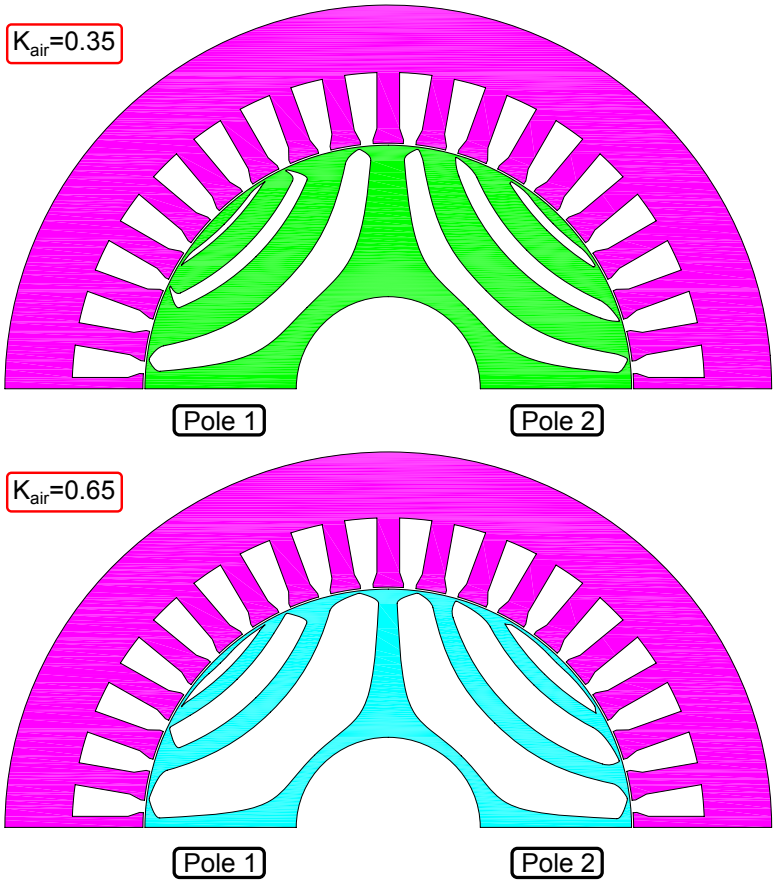

Figure 3.21: Machines layouts for $k_{air} = 0.35$ and $k_{air} = 0.65$ configurations ("Machaon" structures).

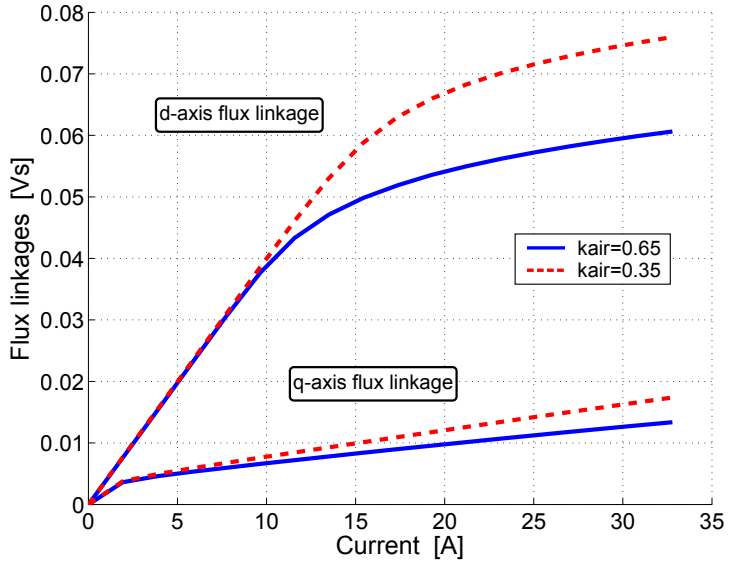

Figure 3.22: The d-axis and q-axis flux linkages for $k_{air} = 0.35$ and $k_{air} = 0.65$ configurations.

3.8.1 FLUX LINKAGES

The results carried out by means of FE analysis highlight differences in term of torque ripple, average torque and power, flux linkages, losses and power factor (PF). Increasing the level

of saturation by enlarging the thickness of flux-barriers (i.e., increasing k_{air}) the level of the flux density in the rotor increases. On the other hand, the phenomenon is reverse in the stator because the amplitude of the flux density decreases due to the saturation. The behavior of the flux linkages is shown in Fig. 3.22. It shows that, with higher k_{air} (that is, with larger flux-barrier thicknesses), the q-axis flux linkage decreases greatly (about 30%). However, the d-axis flux linkage also decreases at higher current due to iron saturation. The actual decrease corresponds to about three times the decrease of q-axis flux linkage. Coefficient k_{air} has to be chosen according to the stator geometry (e.g. tooth width and back-iron height) and in this way it is possible to define a coefficient $k_{air,s}$ related to the stator geometry as follow:

$$k_{air,s} = \frac{p_s - w_t}{p_s} \tag{3.47}$$

in which p_s is the stator slot pitch defined as: $p_s = \pi\ D_{is}/Q_s$ and w_t is the stator tooth width. It is evident that the k_{air} of the rotor should be close to the $k_{air,s}$ of the stator, so as the machine results to be equally saturated.
It is interesting to determine the convenience of having $k_{air} > k_{air,s}$ or $k_{air} < k_{air,s}$. In order to highlight the differences, two extreme cases are considered. Since the stator $k_{air,s} = 0.46$, the rotor coefficients have been selected to be $k_{air} = 0.35$ and $k_{air} = 0.65$ respectively. In order to limit the iron losses $k_{air,s}$ should be close to k_{air}.

3.8.2 TORQUE RIPPLE, MEAN TORQUE AND POWER AND POWER FACTOR

The expression of the torque for REL machine is:

$$T = \frac{3}{2}\ p\ (\lambda_d\ i_q - \lambda_q\ i_d) + \frac{d\ W_{mc}(i_d, i_q, \vartheta_m)}{d\ \vartheta_m} \tag{3.48}$$

where W_{mc} in the magnetic coenergy that is a function of $i_d,\ i_q$ and ϑ_m. The first part of (3.48) gives the average value of the torque, whereas the second one takes into account the coenergy variation with the rotor position, used to estimate the torque ripple of the machine.
As (3.48) shows, the torque strictly depends on the difference between the d- and q-axis flux linkages, whose variation with k_{air} is reported in Fig. 3.22.

Fig. 5.25 shows the motor torque and power versus speed for the two REL motors. The optimal current vector trajectory is achieved by means of the MTPA, FW and Maximum Torque Per Voltage (MTPV) points. The torque and the power decrease as the k_{air} increases. This points out that the main impact of k_{air} is the decrease of d-axis flux linkage due to iron saturation.
Due to the saturation the maximum torque-per-ampere (MTPA) trajectory changes if the k_{air} increases from 0.35 to 0.65. The optimal current phase angle α_i^e in the nominal conditions is equal to $54\ deg$ with $k_{air} = 0.35$ and equal to $57\ deg$ with $k_{air} = 0.65$.

The flux-barrier thicknesses influence the torque ripple as well. Fig. 3.24 shows that when $k_{air} = 0.35$ the maximum peak-to-peak ripple is equal to $2.71\ Nm$ and when $k_{air} = 0.65$ the ripple reduces to $2.13\ Nm$. The effect of the higher rotor saturation is that the amplitude of the higher torque harmonics decreases as can be seen for harmonics 18, 36 and 54 of Fig. 3.24.

It is worth noticing that the choice of the rotor k_{air} has a direct impact on the stator iron losses. In fact, when k_{air} increases, the flux density is limited by rotor saturation. As a consequence, the stator tooth iron losses and the back-iron losses decrease as k_{air} increases as shown in Fig. 3.25.

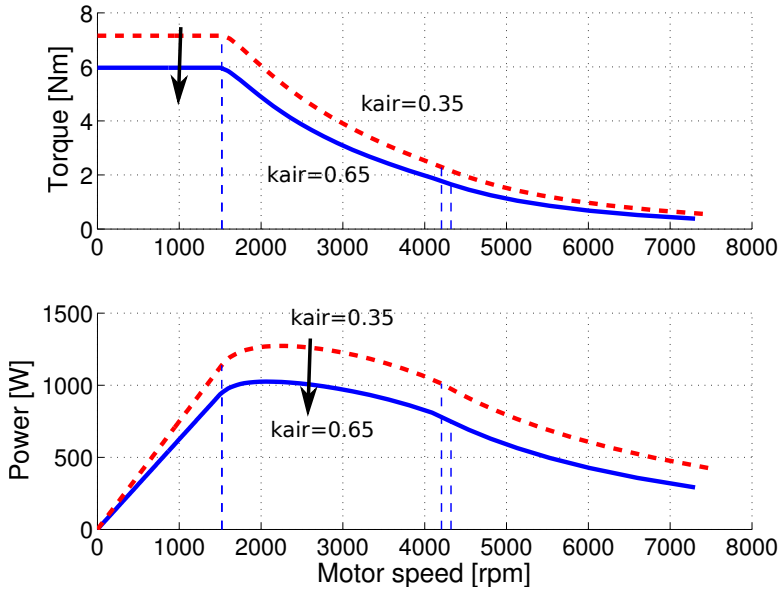

Figure 3.23: Torque and power for $k_{air} = 0.35$ and $k_{air} = 0.65$ configurations, when the current vector moves along the optimal trajectory.

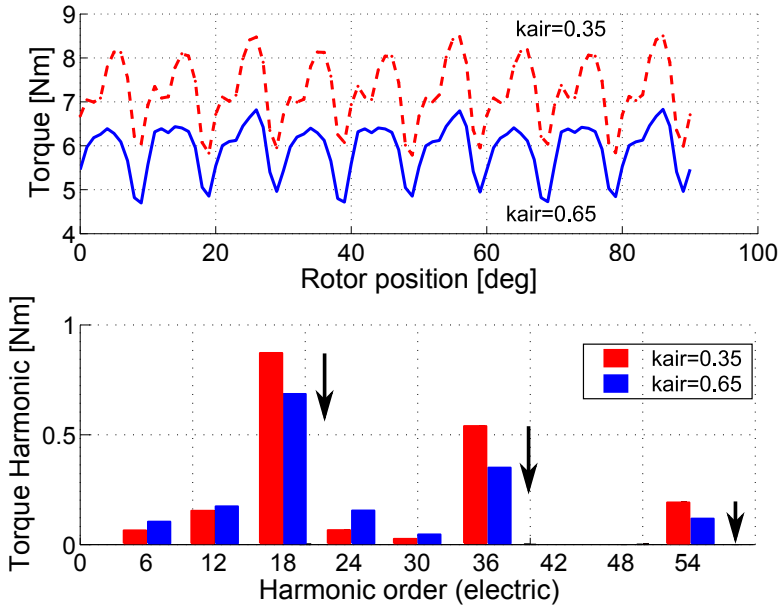

Figure 3.24: Torque ripple for $k_{air} = 0.35$ and $k_{air} = 0.65$ configurations.

The voltage phase angle variation is not so relevant because both the d- and q-axis flux linkages decrease as the saturation increases. As a result, the power factor becomes slightly higher with higher coefficient k_{air} as shown in Fig. 3.26.

The efficiency does not change significantly with the saturation because with higher levels of saturation (i.e. higher k_{air}) the iron losses decrease (as Fig. 3.26) together with the mechanical power (as Fig. 5.25) delivered by the machine. Therefore, both output power and losses decrease with k_{air}, so that the two motors exhibit similar efficiency.

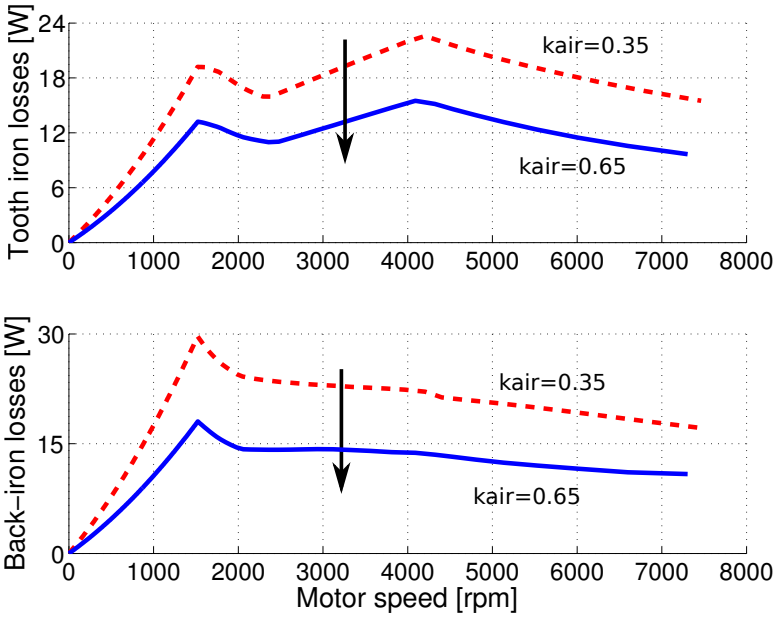

Figure 3.25: Stator iron losses for $k_{air} = 0.35$ and $k_{air} = 0.65$ configurations, when the current vector moves along the optimal trajectory.

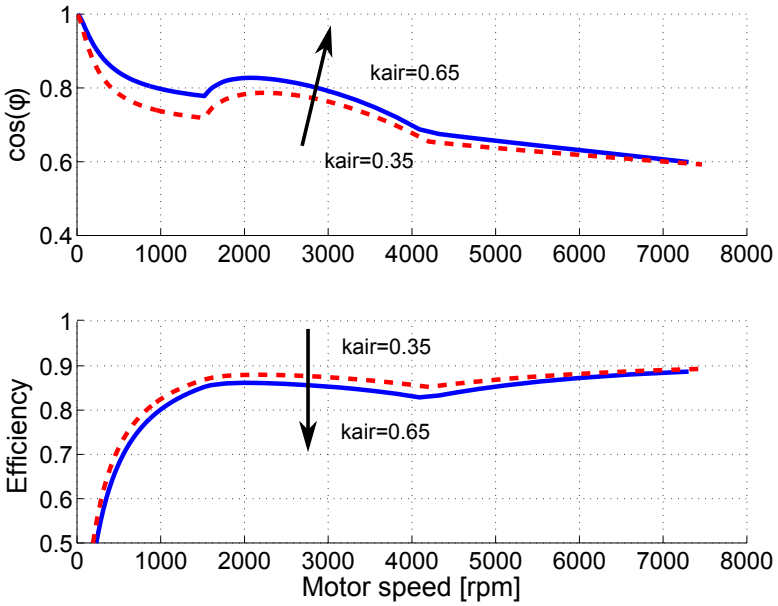

Figure 3.26: Power factor and efficiency for $k_{air} = 0.35$ and $k_{air} = 0.65$ configurations, when the current vector moves along the optimal trajectory.

3.9 THE PMAREL MOTOR

In this Section a rotor structure with an optimized $k_{air} = 0.45$ (see Fig. 3.28 top) has been chosen so as to achieve good behaviors of torque, power factor and efficiency versus speed. The effects of PMs insertion in the rotor barriers is taken into account. The layout that have been studied is shown in the bottom of Fig. 3.28, introducing Ferrite PMs inside the flux-barriers. They are low cost rare-earth-less PMs.

In the design of the PMAREL layout it has been taken into account the equivalent magnet

flux linkage source current I_{ch} also called characteristic current, [22–24]. In an IPM machine, I_{ch} is defined as:

$$I_{ch} = \frac{\Lambda_{pm}}{L_d} \tag{3.49}$$

where Λ_{pm} is the magnetic flux linkage due to the PMs and L_d is the d-axis machine inductance. It is computed imposing a negative d-axis current so as to achive a zero flux linkage. Fig. 3.27 shows the flux density plots in the machine when it is fed by the $I_d = -I_{ch}$. It is worth noticing that such a current forces the flux density lines due to the assisting PMs to remain into the rotor. In the considered machine I_{ch} results to be $0.76\ I_n$.

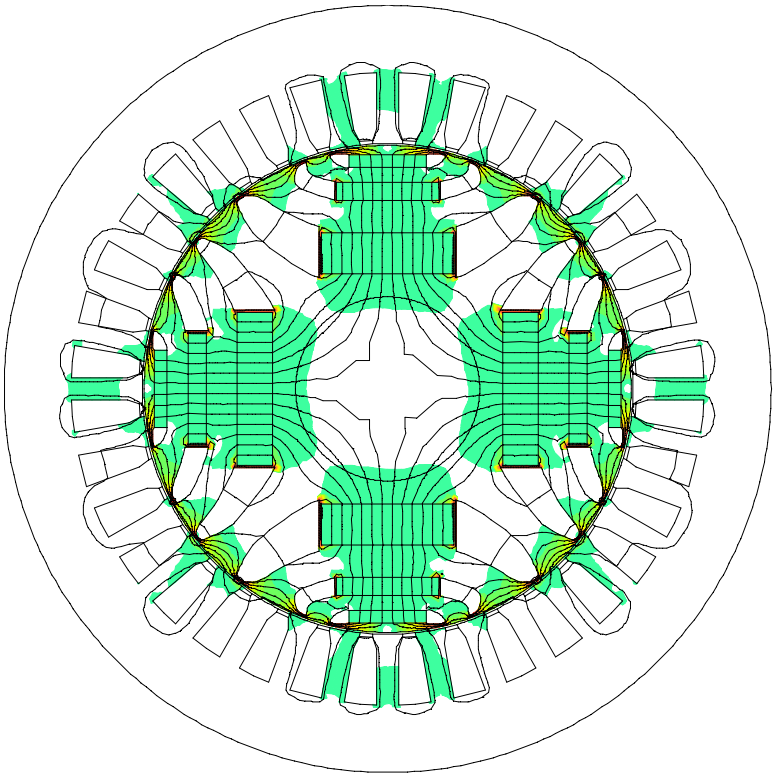

Figure 3.27: Flux density plots feeding the machine with $I_d = -I_{ch}$.

Fig. 3.29 shows the improvement of the torque behavior versus speed due to the adoption of Ferrite PMs. The base torque improvement is about 25%. It is worth noticing that the power in FW operations increases up to $1500\ W$ and remains constant up to the maximum speed. Such a behavior is due to the fact that the I_{ch} has been chosen close to the I_n. These behaviors have been obtained following the MTPA trajectory, FW region I (constant current, constant voltage) as well as FW region II (decreasing current, constant voltage), also called MTPV trajectory. Vertical dashed lines separate operating regions I and II. It is worth noticing that the PMAREL configuration does not reach the FW region II in the whole speed range considered.

Another important effect of adding PMs is presented in Fig. 3.30, that shows the increase of the power factor. The power factor stands always above 0.8 and always higher than the REL machine. The power factor improvement is more beneficial as the speed increases. It means that the size of the converter could be lower for the same base torque adopting the PMAREL solution.
As shown in the bottom of Fig. 3.30 the efficiency of the PMAREL is also higher of that of the REL machine.

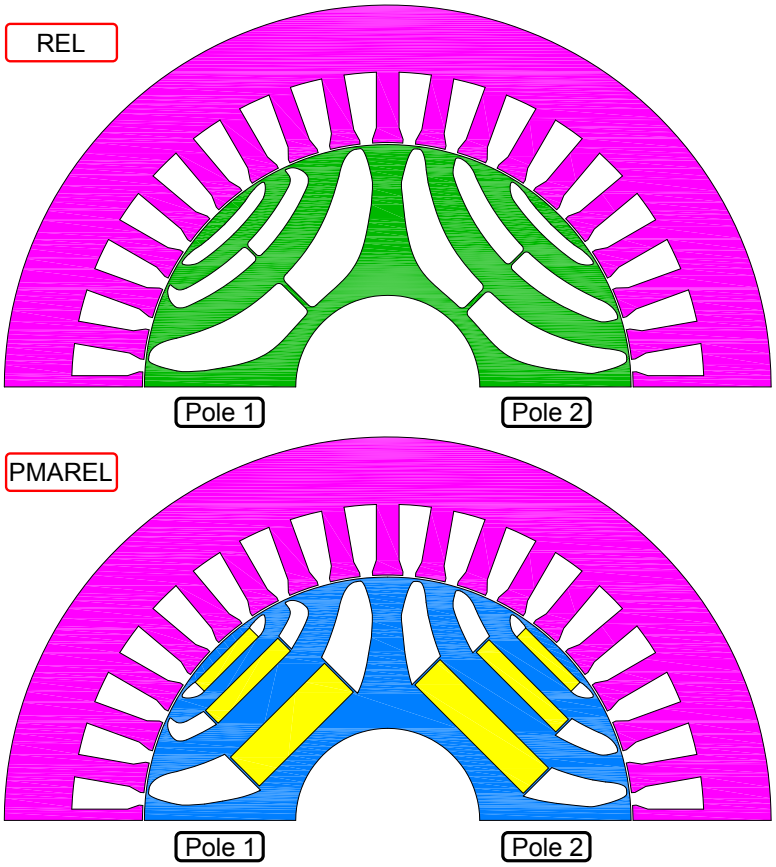

Figure 3.28: PMAREL and REL machines layouts (”Machaon” structures).

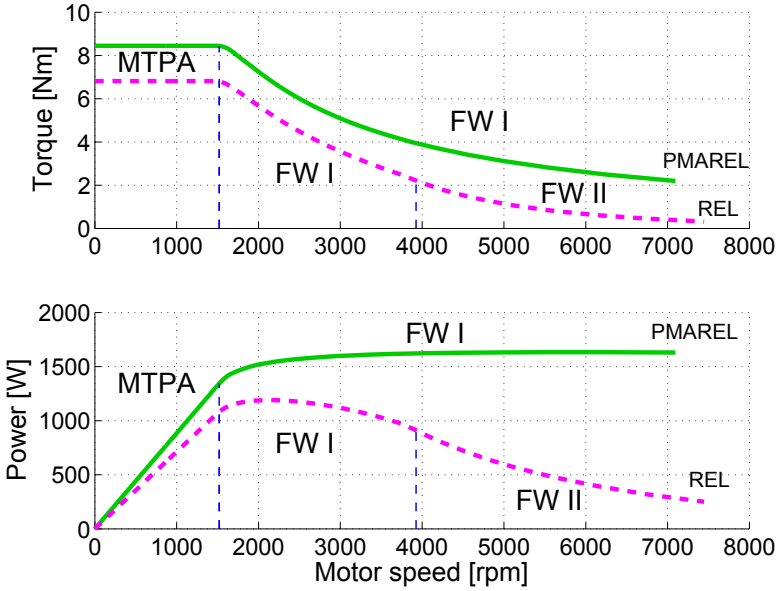

Figure 3.29: Torque and power for PMAREL and REL configurations, when the current vector moves along the optimal trajectory.

Fig. 3.31 shows the torque ripple comparison between REL and PMAREL motors. It is worth noticing that the higher torque harmonic is that of 36-th order. This is due to the choice of the ”Machaon” rotor structure, that has been optimized so as to reduce the torque harmonic

of order 18-th (the first slot harmonic).
Besides the increase of the average torque, as seen above, the insertion of PMs also yields a slight decrease of the torque ripple from 35% to 31%.

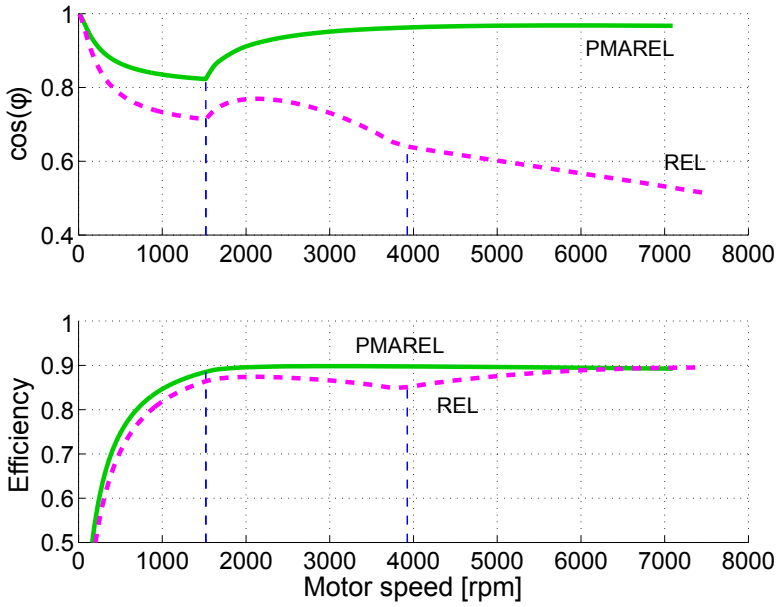

Figure 3.30: Power factor and efficiency for PMAREL and REL configurations, when the current vector moves along the optimal trajectory.

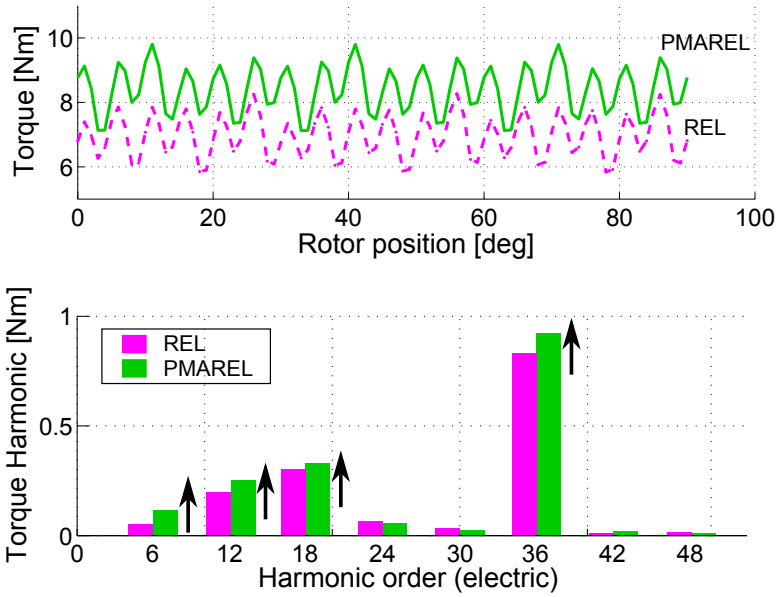

Figure 3.31: Torque ripple for PMAREL and REL configurations without skewing.

Fig. 3.32 and 3.33 show efficiency maps for the REL and the PMAREL configurations, respectively. Each map has been carried out by estimating all the power losses (copper, iron and mechanical losses) along the optimal current vector trajectories for each current value. The assistant of PMs gives advantages in terms of power factor and efficiency. The maximum efficiency of the REL motor is equal to $88\ \%$. The maximum efficiency of the PMAREL motor is instead equal to $92\ \%$. In addition, the PMAREL solution operates at high efficiency in a

wide speed-torque range, as shown in Fig. 3.33.

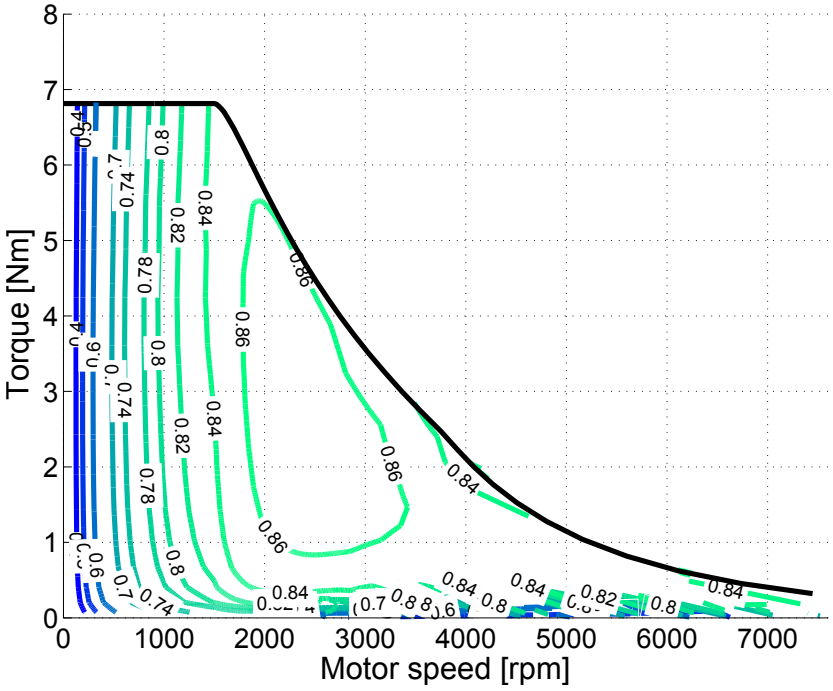

Figure 3.32: Efficiency map of the REL machine.

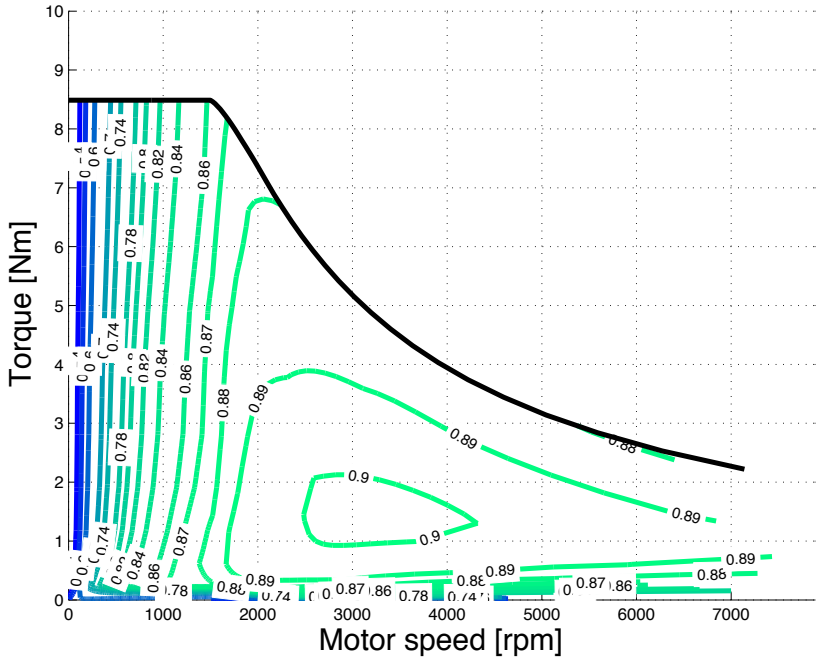

Figure 3.33: Efficiency map of the PMAREL machine.

3.9.1 SATURATION EFFECTS DUE TO THE PHASE CURRENT VARIATION

Iron saturation strongly depends on the rotor geometry (i.e. flux-barriers thickness) and on the current *I*. In order to study the effect of the current, the PMAREL configuration of Fig. 3.28 has been taken into account.
FE simulations have been performed with three current values: I_n, $2I_n$ and $3I_n$, along the MTPA trajectory. Fig. 3.34 shows the torque versus rotor position. The harmonic amplitudes increase with the current increasing, especially at low harmonic orders. Increasing the current, the torque ripple decreases from 32% with $I = I_n$ to 22% with $I = 3I_n$ due to the corresponding increase of the average torque.
Referring to Fig. 3.35 the torque at base speed increases with the current increasing, whereas the FW capability decreases with the current increasing. In FW operations the torque halves at $4500\ rpm$ for $I = I_n$ and at $2500\ rpm$ for $I = 3I_n$.The effect of torque decreasing is also evident from the behavior of the power versus speed. The higher the current, the higher the power drop.

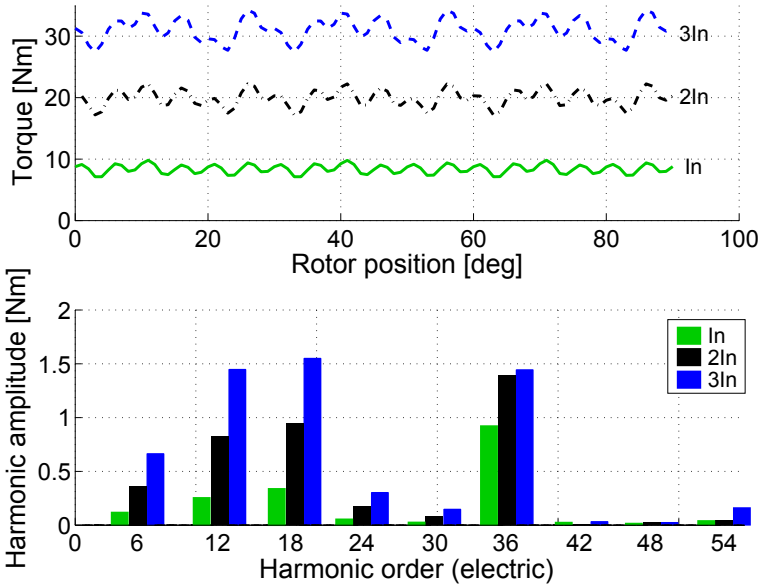

Figure 3.34: Torque ripple for PMAREL with I_n, $2I_n$ and $3I_n$ without skewing.

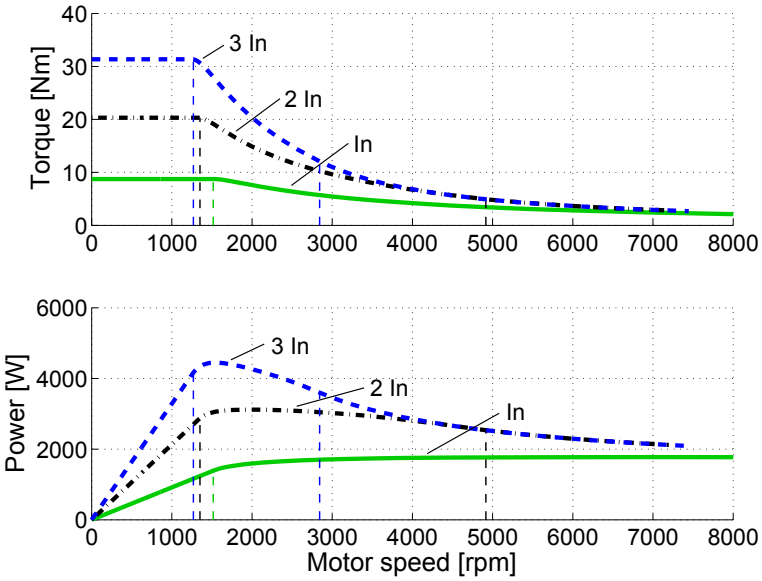

Figure 3.35: Torque and power for PMAREL with I_n, $2I_n$ and $3I_n$, when the current vector moves along the optimal trajectory.

3.10 EXPERIMENTAL RESULTS

The experimental results reported in this section are referred to the *REL 2* machine, see Table 3.2.
The prototype is a pure REL machine with "Machaon" rotor configuration and the layout is presented in Fig.3.36. The coefficient k_{air} is 0.49 and the coefficient $k_{air,s}$ is 0.41. The geometry of the flux-barriers has been chosen so as to allow rectangular PMs to be inset in the rotor, if necessary. The rotor of the machine has been manufactured with a continuous skewing of 10 deg since there are no PMs into the flux-barriers.

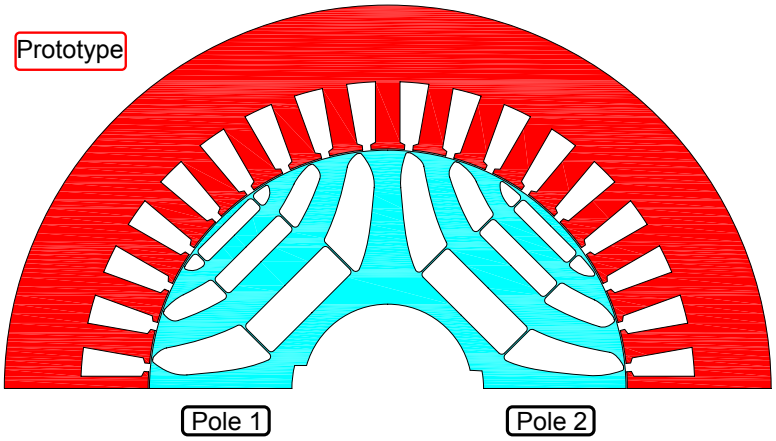

Figure 3.36: Layout of the REL prototype.

Some experimental tests have been performed in an appositely test bench composed of an induction machine coupled with the REL motor under examination. During the tests torques, voltages and temperatures have been acquired.

Two types of tests have been performed:

- MTPA angles have been carried out with four different values of current.
- The constant torque loci of the machine in the d-q current plane has been achieved.

The first test has been performed with the aim to obtain the torque versus current vector angle. For given current amplitude, the torque during a whole revolution of the rotor has been sampled repeating the measures varying the current angles from 0 to 90 deg. This procedure has been carried out for four different current amplitudes (5, 10, 15 and 20 A). Fig. 3.37 shows the average torque versus the current vector angle. The dashed line shows the torque variation due to the ripple achieved with a current of 15 A. It is worth noticing that the torque ripple changes slightly with the current angle, in particular it becomes higher in proximity of the MTPA angle. Red circles show the angles in which the torque is maximum for any given current amplitude.

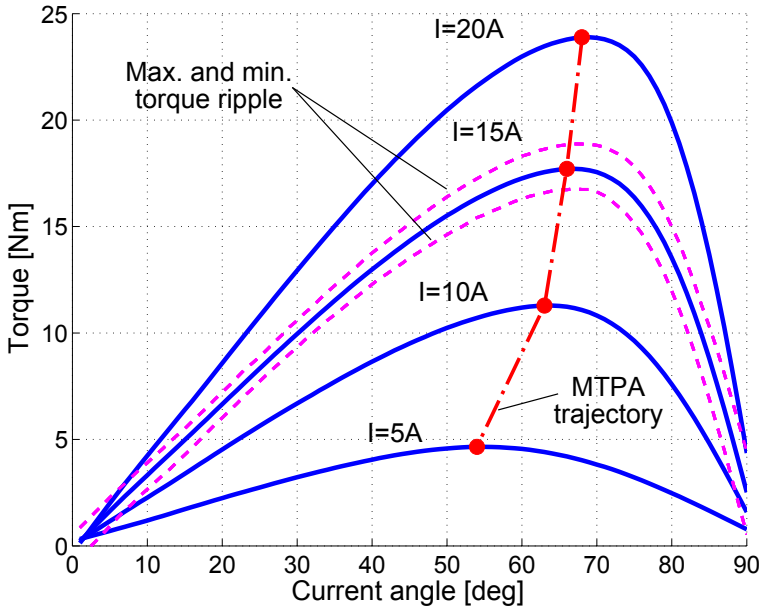

Figure 3.37: Torque variation for different current angles of the REL prototype (experimental results).

Fig. 3.38 shows the torque versus rotor position behavior at nominal current (10 A). The solid line shows the experimental measurement whereas the dashed line shows FE results. The comparison gives a satisfactory agreement. The estimated average torque is 11.6 Nm with a torque ripple of 7.5% whereas the experimental results show that the mean torque is 11.3 Nm and the torque ripple is 9.1%.

The second test has been performed imposing different values of d- and q-axis currents. For each current combination the torque has been sampled along a whole revolution of the rotor. Fig. 3.39 shows the constant torque loci achieved from the experimental results (dashed lines) and those obtained with FE simulations (solid lines). Dashed circles show the current amplitudes. It is worth noticing that with low levels of saturation the FE results match properly the experimental results. There are slightly differences at high overload operating conditions.

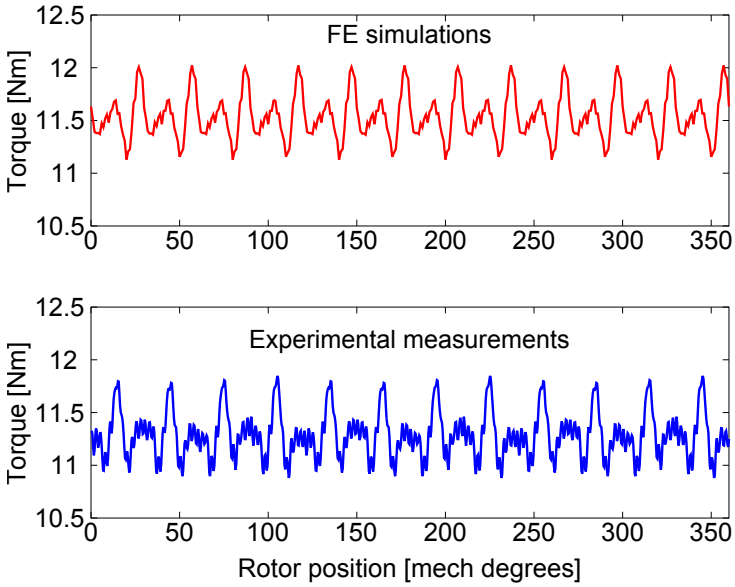

Figure 3.38: Torque ripple comparison between REL prototype and FE simulations (with skewing).

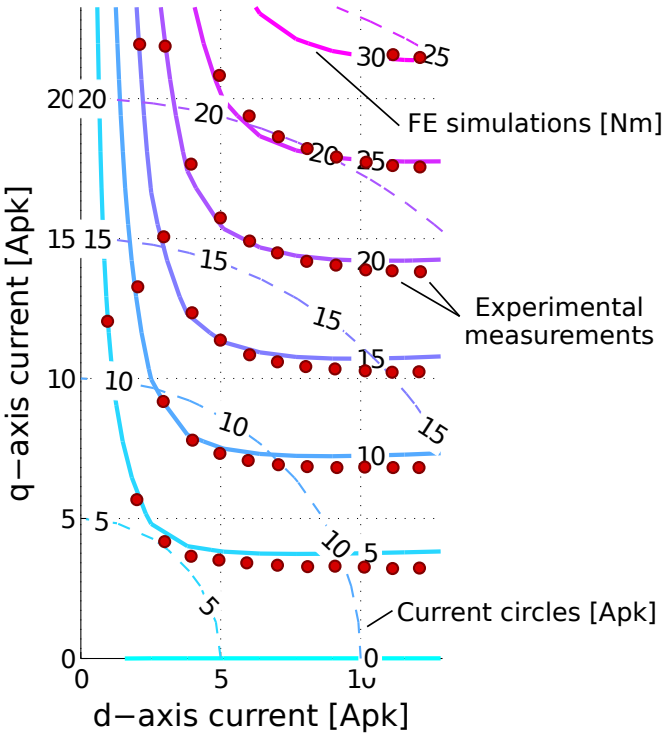

Figure 3.39: Constant torque loci comparison between FE simulations and experimental measurement.

Chapter 4

DYNAMICS OF SYNCHRONOUS ELECTRIC MACHINES

Torque ripple may excite torsional vibrations of the motor and of the system composed of motor shaft and load. This problem has particular importance in the case of the reluctance motor, since the flux barriers reduce the stiffness of the rotor and in particular torsional stiffness. For this reason an exploratory dynamic FE analysis has been carried out. In the first part of the chapter the rotor has been studied with the aim of highlighting the effect of flux barriers on natural frequencies and modes. In the second part of the chapter the rotor has been analyzed in order to evaluate the mechanical deformations due to the forces acting on it.

The contents of this chapter have been taken from my personal scientific publications: [6,7].

4.1 ROTOR VIBRATION MODES

The following analysis have been carried out considering the solutions A, B and $A+B$ of the REL motor presented in Section 3.7. First the rotor alone has been studied with the aim of highlighting the effect of flux barriers on natural frequencies and modes. The rotor of the prototype motor will be composed of a stack of iron sheets pressed together and fixed to a threaded shaft by means of a couple of nuts. In order to simulate the behavior of the rotor mounted on a very stiff shaft, the annular abutment surfaces, in which there is the contact between the rotor and the nuts, are considered to be fixed. Fig. 4.1 shows the first modes of vibration of rotor A, the red (dark) color represents the largest resultant displacement, whereas the blue (light) color represent zero displacement. Natural frequencies are summarized in Table 4.1. The first mode is a torsional mode of vibration of the rotor and it is characterized by large deflections of the four spokes in the same tangential direction. The second mode shows a couple of spokes (the vertical and the left one) with tangential deflections in one direction and the other couple with tangential deflections in the opposite direction. The third mode of vibration in similar to the second one. Finally, the fourth and the fifth mode are complex 3D modes.

Rotor B exhibits modes of vibration and natural frequencies similar to the rotor A, Fig. 4.3a represents the torsional mode. The Machaon rotor is not axial-symmetrical. The natural frequency of the torsion mode, which is represented in Fig. 4.3b, is slightly lower than in rotors A and B. The second and third modes are again characterized by tangential deflections of the spokes in different directions. Owing to the lack of symmetry, they show larger differences in shape and frequency than the corresponding modes of the axial-symmetrical rotors. Since

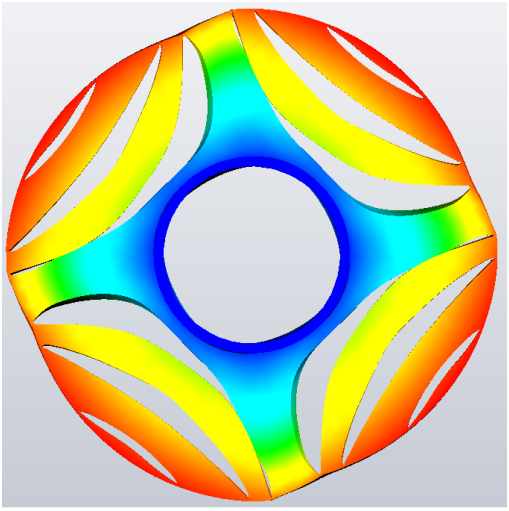

(a)

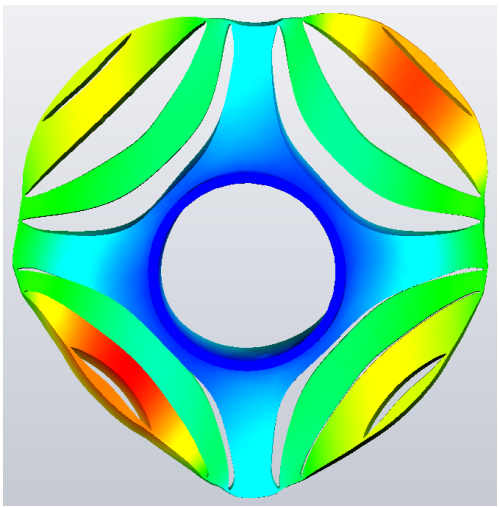

(b)

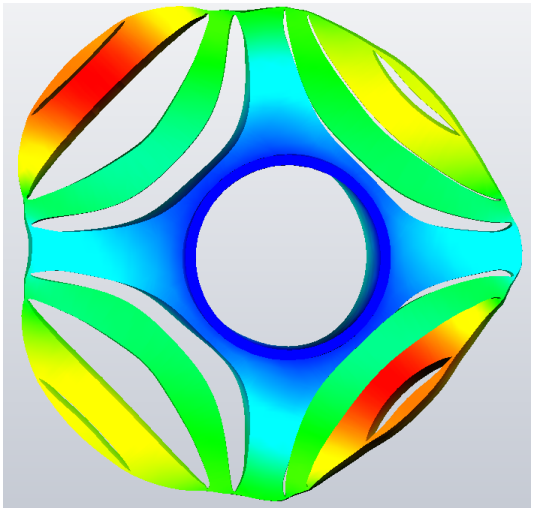

(c)

Figure 4.1: Vibration modes (1^{st}, 2^{nd} and 3^{rd}) of the solution A

the first modes of vibration of the rotors are dominated by the flexure of spokes, centrifugal force caused by rotor rotation has a stiffening effect and may lead to an increase in natural frequencies [25–27]. The presence of torsional modes of the rotor in the range $2500 - 2600\ Hz$ may alter significantly the torsional dynamics of the whole system composed of the reluctance motor, the shaft and the load. Actually the natural frequency of the first torsional mode of the whole system depends on the torsional stiffness of the shaft and on the inertia of the load. If the rotor of the load is very stiff and large, the simplest model for the study of torsional vibrations can assume the shaft fixed at one end, see Fig. 4.2.

In this case, if the rotor is rigid and deformability is concentrated in the shaft (diameter d=36 mm and length L=85mm), the natural frequency of the torsion mode results to be about $3000\ Hz$. When both the rotor and the shaft are not rigid a large reduction in the natural frequency of the first torsion mode is expected. For this reason a FE analysis of the whole system with the constraints represented in Fig. 4.2 has been carried out considering the "Machaon" rotor and a steel shaft (d=36 L=85mm). Fig. 4.4 shows the torsional mode of the whole system, Table 4.1 summarizes the natural frequencies of the whole system. The natural frequency of

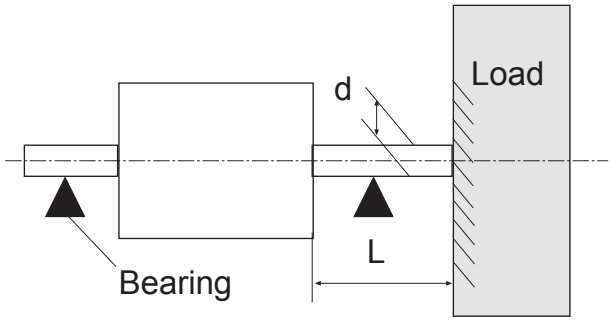

Figure 4.2: Scheme of the motor-load system.

the first torsional mode is about 1050 Hz and it is rather lower than the ones shown by the two subsystems (rotor and shaft) alone. The higher frequencies correspond to more complex modes that involve flexural deformation of the rotor and shaft. Similar results have been obtained simulating the behavior of the other rotors mounted on the same shaft. Fig. 3.19 shows that the relevant harmonics of torque ripple are the 6^{th}, 12^{th}, 18^{th} and 36^{th}, which correspond to excitation frequencies of 600 Hz, 1200 Hz, 1800 Hz and 3600 Hz respectively. With solution *B* and "Machaon" the harmonic is the 18^{th} (1800 Hz), whereas with solution *A* the most important harmonic is the 36^{th} (3600 Hz). If the torsional behavior of the whole system is considered, excitations at 3600 Hz and 1800 Hz are above the natural frequency of the first torsional mode. Excitation at 1200 Hz caused by the 12^{th} harmonic of torque ripple is the most dangerous, since it is rather close to the natural frequency of the torsional mode. From this point of view, rotor *A*, which exhibits the lowest harmonic at 1200 Hz has the best dynamic behavior in the reference constraint conditions. Excitation at 600 Hz due to the 6^{th} harmonic is well below the typical natural frequencies of the system.

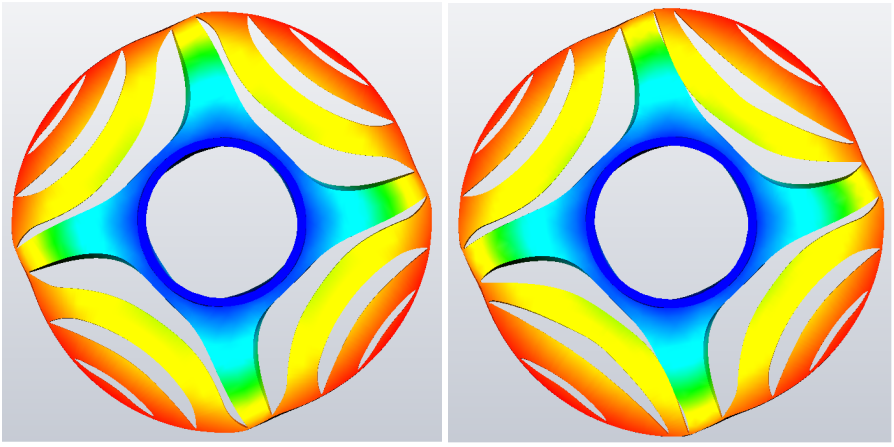

(a) (b)

Figure 4.3: Vibration modes (1^{st}) of the solutions B and A+B

Table 4.1: Vibration frequencies [Hz]

Mode	Solution A	Solution B	A+B (Machaon)	A+B (+shaft)
1	2602	2609	2587	1026
2	4047	3905	3676	2559
3	4052	3952	4055	2621
4	4990	4717	4556	3571
5	5037	4738	4584	4349

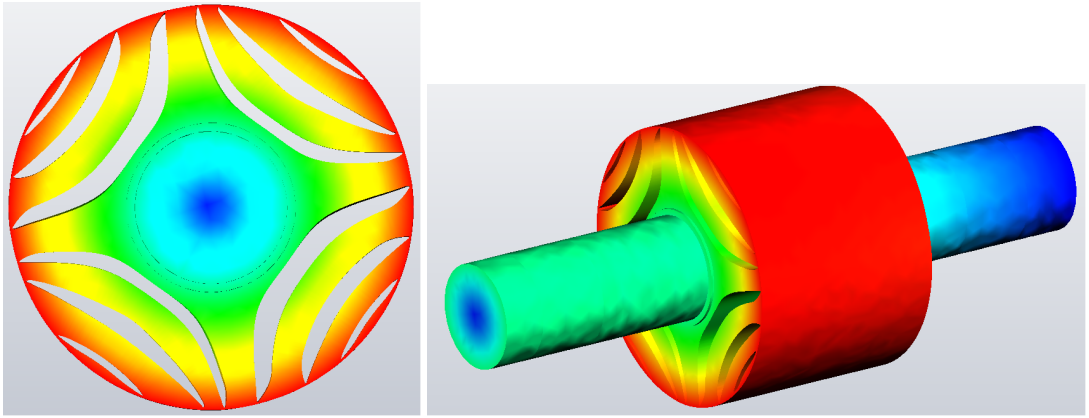

(a) (b)

Figure 4.4: Vibration modes (1^{st}) of the solution A+B + shaft

4.2 MECHANICAL STRESS

The following analysis have been carried out considering the REL motor prototype presented in Section 3.10. The layout shown in Fig. 3.36 has been verified by means of mechanical FE simulations in order to verify the ribs and to investigate possible displacements of the external diameter of the rotor so as not to compromise the air gap.
The considered loads in the radial direction are centrifugal and magnetic forces whereas in the tangential direction is the electromagnetic torque. The constraints have been applied only on the inner surface of the rotor, considering an infinite shaft stiffness.
Simulations have been performed in two conditions:

1. at maximum torque (20 Nm) and rated speed (1400 rpm) to verify the effect of the torque, as shown in Fig. 4.6;
2. at maximum speed (3000 rpm) and overload torque (5.7 Nm) to check the effect of centrifugal forces, as shown in Fig. 4.7.

Fig. 4.5 shows the points in which mechanical simulations have been performed.

Simulation results show that the maximum deformation is 20 μm when the maximum torque is applied. Deformations of these entities do not compromise the shape of the rotor and its flux-barriers.

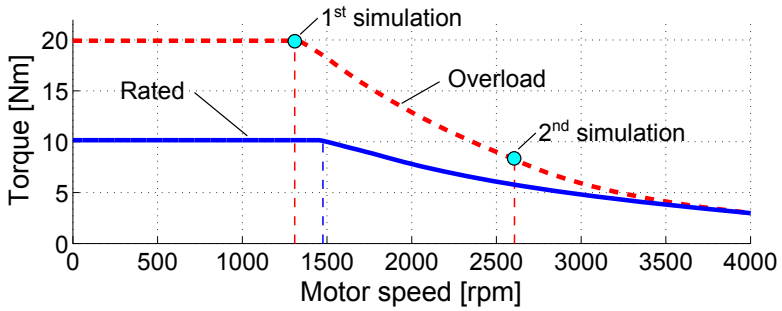

Figure 4.5: Conditions of simulation.

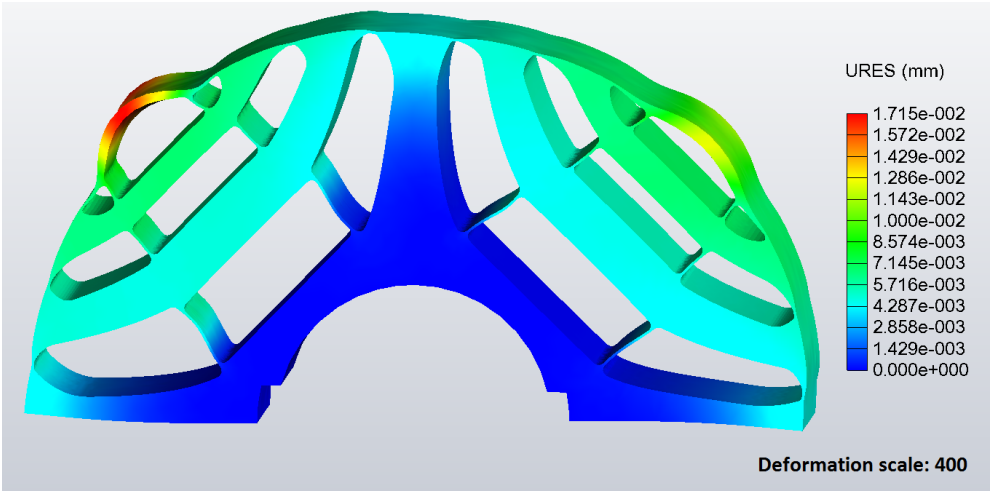

Figure 4.6: Deformation analysis of the rotor, when the speed is 1400 rpm and the torque is 20 Nm.

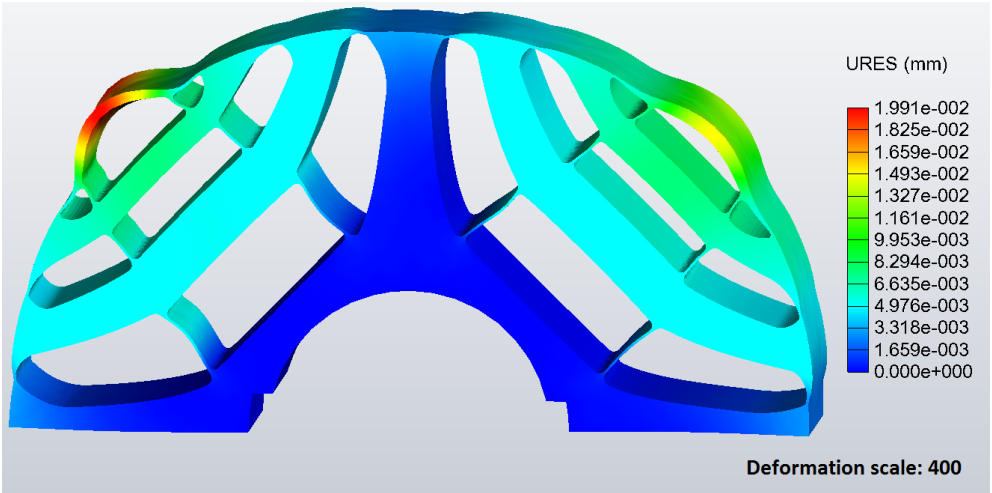

Figure 4.7: Deformation analysis of the rotor, when the speed is 3000 rpm and the torque is 10 Nm.

Chapter 5

APPLICATIONS

Nowadays in developed and developing countries the problems of pollution, traffic jam and lack of energy sources are becoming more and more important; for this reason there is a significant development of electric and hybrid technologies for road transportation.
The reduction in traffic and in energy consumption requires the development of small vehicles with a narrow track and three wheeled vehicles in the next future may play an important role in urban mobility.
The introduction of an electric or hybrid propulsion system in a small vehicle is a challenge and a chance for the vehicle designers.
Electric or hybrid propulsion is a challenge, because some heavy components have to be accommodated in a narrow room and because the dynamic behavior of a two- three-wheeled vehicle is strongly influenced by the added masses (the mass of the electric components is comparable with the mass of the chassis), specific dynamic studies are needed to maintain the handling and stability properties of conventional vehicles equipped with internal combustion (i.c.) engines (as seen in Chapter 2). Electric or hybrid propulsion is a chance, because electric motors and electronic controls make possible some technical solutions that would be very difficult if an i.c. engine were adopted. For example a hub motor can be fitted on the front wheel of a scooter without particular difficulties.

This chapter deals with three particular cases study. The first two applications are tilting three-wheeled vehicles which have been developed at Motorcycle Dynamics Research Group (MDRG) of Padova University. They are characterized by a particular mechanical connection between the tilting module and the non-tilting module and they are suited both to an advanced electric propulsion system and to a hybrid propulsion system. The third application is a mild hybrid motorcycle prototype, realized in collaboration with Aprilia Racing company.

5.1 HY-SNAKE

Tilting three-wheeled vehicles equipped with one front wheel that tilts, two rear wheels that do not tilt and a pivot that connects the front module with the rear (non-tilting) module are very simple but have some mechanical limits [28].
In cornering there is load transfer ΔN in the lateral direction between the wheels of the non-tilting module. ΔN is proportional to the height of the centre of mass of the rear module and inversely proportional to the track width. Hence, narrow track vehicles (which are very useful for urban mobility) are prone to rollover if the cornering speed is large and the mass distribution is not optimized.
The trajectory of the centre of mass of the tilting module is essentially an arc of circumference with the centre in the pivot. Hence the capsize motion of the front frame is unstable as the capsize motion of a motorcycle.
The front wheel has a camber angle, which is very close to the tilting angle of the front module, hence a large amount of the front cornering force is generated by the camber thrust without side-slip. As a result the vehicle has an over-steer behaviour that has to be corrected [29]. Some prototypes are equipped with a rear steer system [30].
There are roll-steer phenomena that modify the directional behaviour of the vehicle.
If the tilting module is connected to the non-tilting module by means of a linkage, the complexity of the vehicle increases, but the designer has more design parameters that make it possible to overcome some of the limits of simpler tilting three-wheeled vehicles.

At MDRG of Department of Industrial Engineering the research on tilting three-wheeled vehicles equipped with linkages has begun some years ago with the development of a prototype equipped with an i.c. engine [31]. The present prototype, which is shown in Fig. 5.1 is suited both to electric and to hybrid propulsion system. The front module, which is tilting, includes the front wheel, the handle-bar, the saddle and the foot-rests. Some components of the propulsion system can be located in a container between the legs of the rider. The rear module, which does not tilt, includes two wheels and most of the components of the propulsion system located in a container between the two wheels. The lower part of the front module (near the foot-rests) is connected to the upper part of the rear module by means of four revolute joints and two rockers. Therefore, the two modules of the vehicle and the two rockers make a four-bar linkage. The front module is the connecting rod of this linkage which translates and rotates with respect to the rear module in the plane perpendicular to the axes of the revolute joints. At every instant an instant centre exists, which is defined by the intersection between the axes of the two rockers. The instant tilting axis is parallel to the axes of the revolute pairs of the four-bar linkage and passes through the instant centre.

The high performance electric vehicle shown in Fig. 5.1 is named E-Snake [32] and it is the reference vehicle for the project "Hy-Snake" in terms of layout of the chassis. The goal is to design a rage extender three-wheeled vehicle equipped with linkage.

The contents of this chapter have been taken from my personal scientific publication [5].

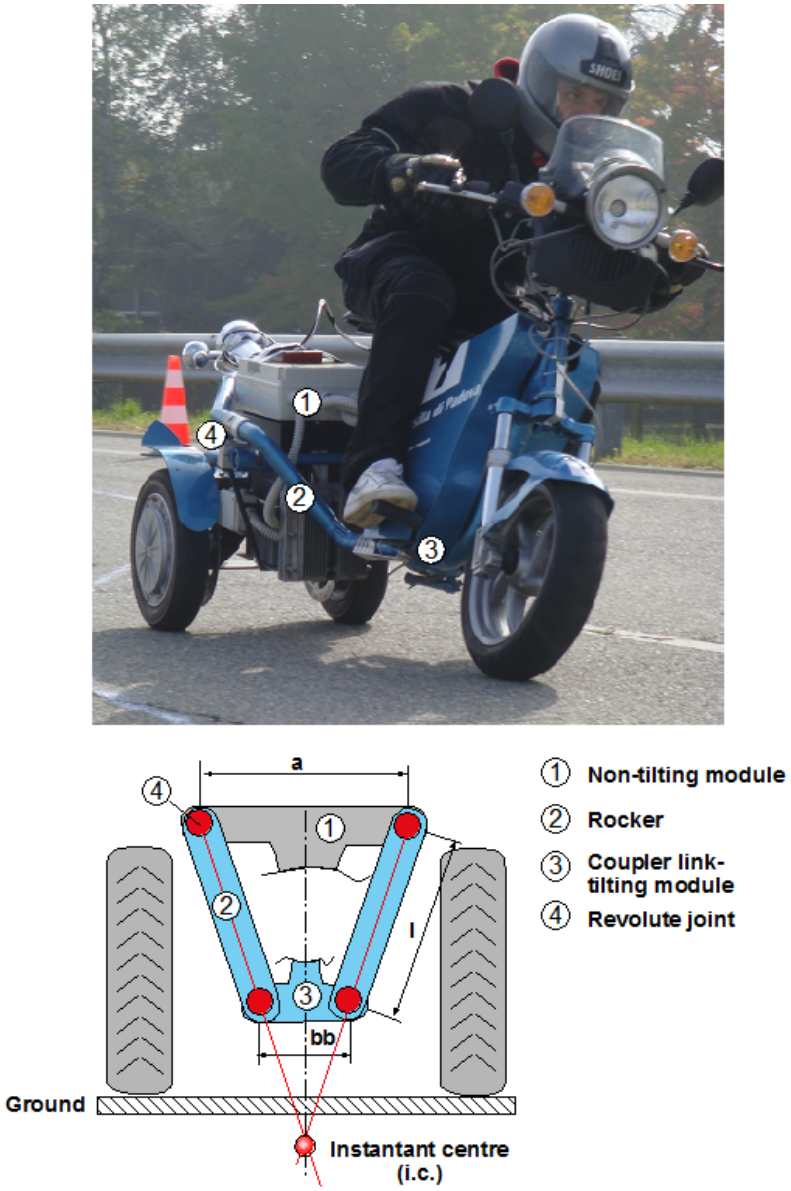

Figure 5.1: Three-wheeled vehicle with the four-bar linkage.

5.1.1 POWER-TRAIN OVERVIEW

The principal feature of Hy-Snake is the series hybrid propulsion system. A scheme of such a power-train is shown in Fig. 5.2.
The vehicle is equipped with two IPM motors placed in the rear frame, the rated torque and rated power of each motor at 1500 rpm are 15 Nm and 2.4 kW respectively. A chain connects each motor to the corresponding wheel, a differential is not needed.
In order to improve the performance of the vehicle in terms of acceleration and hill starting ability, the front wheel can be equipped with an additional hub motor with rated torque of 45 Nm at 640 rpm.
Each motor (IPM and in-wheel motors) is fed by a DC/AC converter connected to the 48 V DC bus.
The front frame is also equipped with an ICE (rated power of 3.3 kW at 2800 rpm) coupled with a Surface Permanent Magnet (SPM) generator which is able to produce a rated power of

2.8 kW. This SPM machine is connected to the 48 V DC bus and is suited to feed the electrical motors when the vehicle is running on sub-urban roads or when the charge of the energy storage system is low.
In particular, there are in the rear frame 13 cells of lithium polymer batteries. They are connected in series in order to reach the voltage of the DC bus.

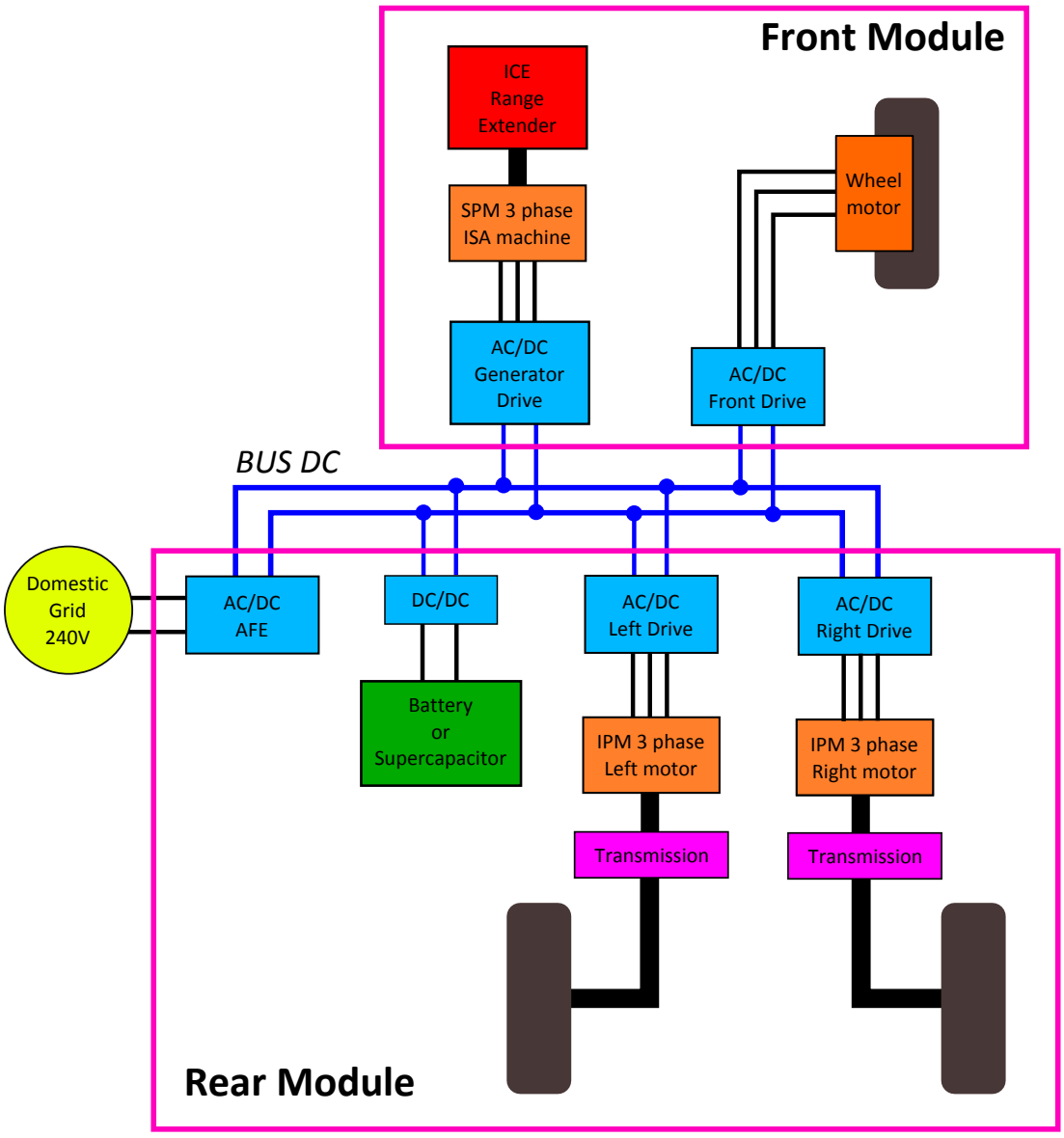

Figure 5.2: Power-train of the Hy-Snake vehicle.

5.1.2 CHASSIS DESIGN

As said before, E-Snake is the reference vehicle. It means that the chassis of Hy-Snake will be similar to the reference one. The aim is to modify the rear frame in order to place the two IPM motors on-board. A careful study has been made to the aim of optimizing the space of the rear frame without increasing the track of the reference vehicle. The design has been also focused on the simplicity of manufacturing and assembling of the parts of the chassis. The main design steps have been reported in the following.

The first proposal is totally made with round tubes and the layout is very similar to the one of the E-snake, as shown in Fig. 5.3. The main drawback of this arrangement is due to the tubes section. Their circular section make difficult the construction of the whole structure.

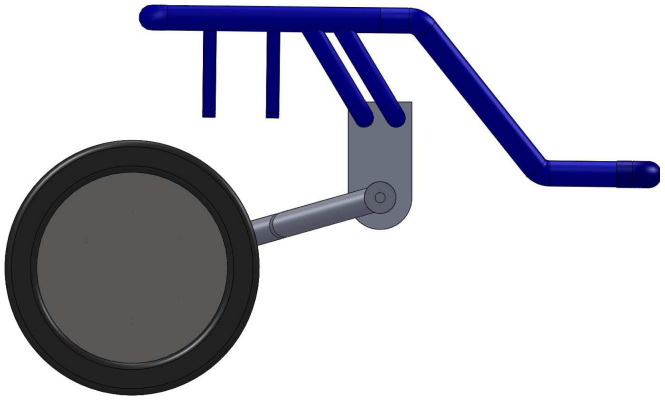

(a)

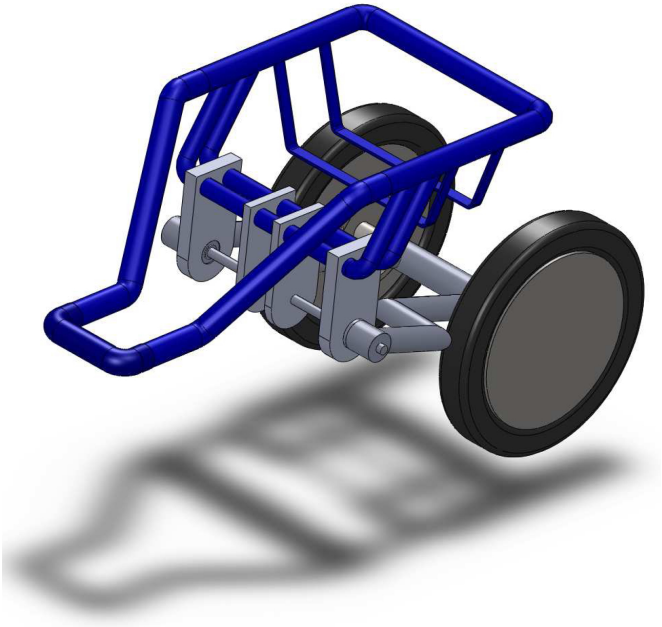

(b)

Figure 5.3: Rear frame with round tubes.

The second proposal is characterized by square tubes, see Fig. 5.4. This feature make easier the construction because the tubes can be welded together without particular problems.

The four-bar linkage is changed, because now the rokers are in vertical position. However the kinematics of the mechanism is not changed.
Finally, the longitudinal kinematic of the whole rear frame is changed, because of its new geometry.

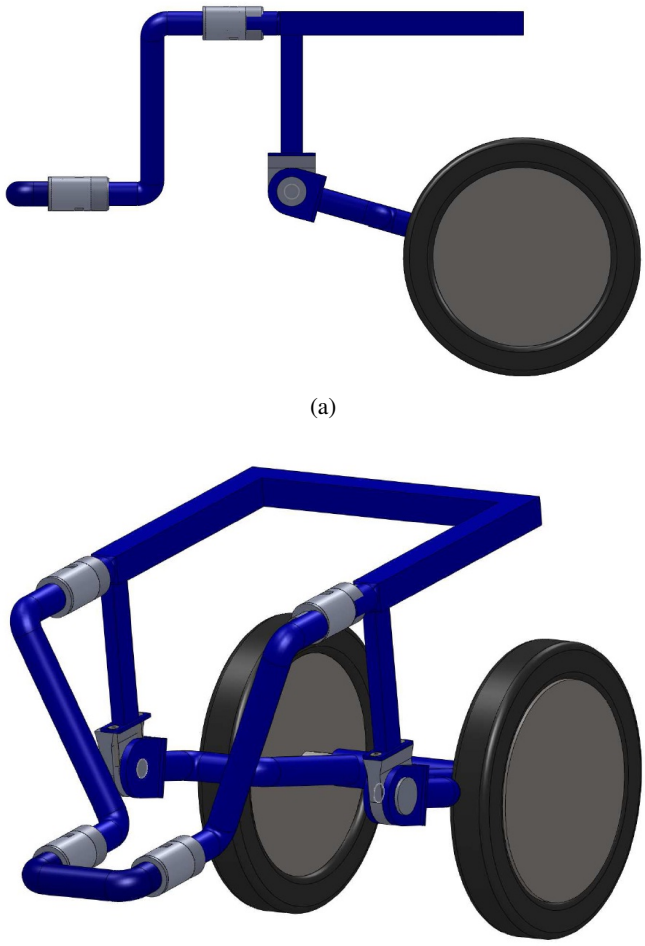

(a)

(b)

Figure 5.4: Rear frame with square tubes.

Finally the third proposal is a fine tuning of the second one, see Fig. 5.5. Improvements are related to the stiffness of the whole structure and to the easy assembly method. The welded parts are minimized and almost all the junctions are realized by screws and bolts.
The final layout allows to place two EMs on the same axis of rotation of the rear fork. This makes possible to connect the EMs to the rear wheels by means of a chain. Oscillations due to load transfers do not compromise the distance between EMs and wheels.

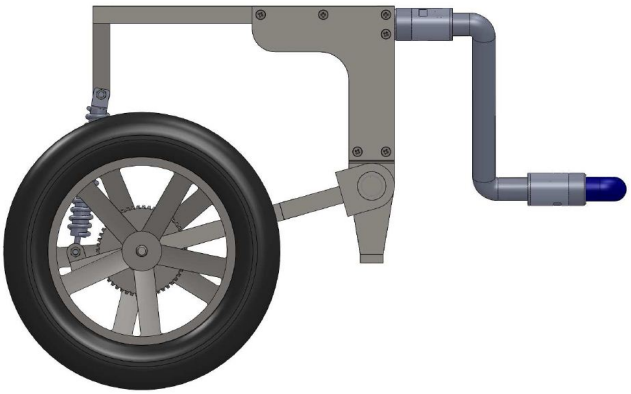

(a)

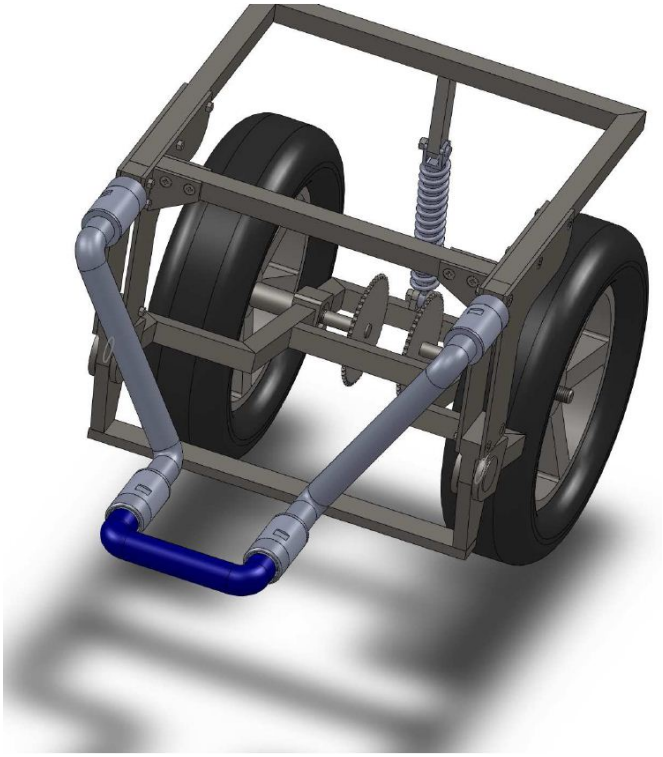

(b)

Figure 5.5: Final layout of the rear frame with square tubes.

The front frame of Hy-Snake is very similar to the one of E-Snake. Only the caster angle has been adjusted in order to limit the wheelbase of the whole vehicle. The whole vehicle is shown in Fig. 5.6.

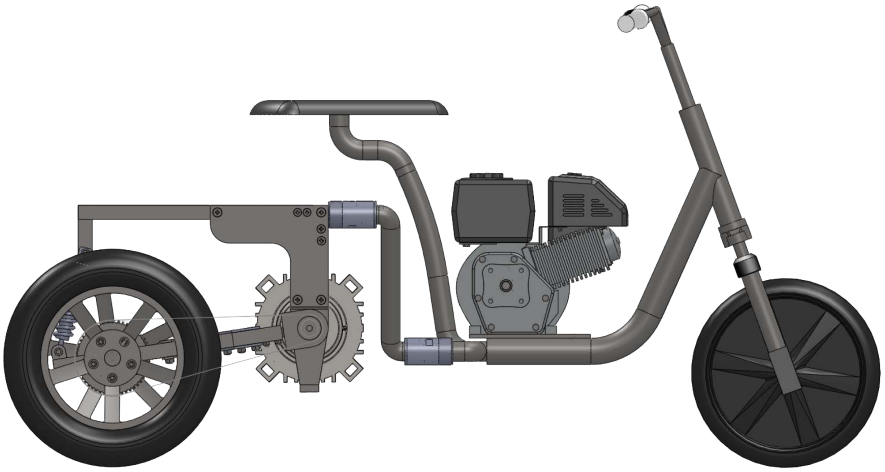

Figure 5.6: Final layout of Hy-Snake.

5.1.3 OPTIMIZATION OF THE FOUR-BAR LINKAGE

To the aim of optimizing the dynamic behavior (handling and safety) of the vehicle, a specific study has been made. In particular, the position of the electrical components (which are a significant part of the total weight of the vehicle) and the four-bar linkage (which governs the vehicle stability) geometry have been optimized.

First, a careful estimation of the weights and the volumes of the electrical components has been made. Table 5.1 collects the weights of the electrical components on board.

Table 5.1: Electrical components

Component	Weight [kg]
IPM motors	26.0
Drives for IPM motors	6.7
In-wheel motor	14.0
Drive for in-wheel motor	1.4
ICE	16.0
SPM generator	7.5
Drive for SPM generator	1.7
Battery pack	14.3
Cables & connections	5.0
Total	92.6

Then the electrical components have been positioned in the vehicle according with their volumes and weights as shown in Fig. 5.7. Also a rider of $80\ kg$ and a payload of $70\ kg$ have been taken into account. Red dots indicate the CoMs of each component.
This step is very important, since the total CoM has to be well known to study the dynamics of such a vehicle (and two-wheeled vehicles in general).
Thanks to the Matlab® code presented in Chapter 2 the stability of the vehicle has been studied and optimized by adjusting the four-bar linkage geometry.

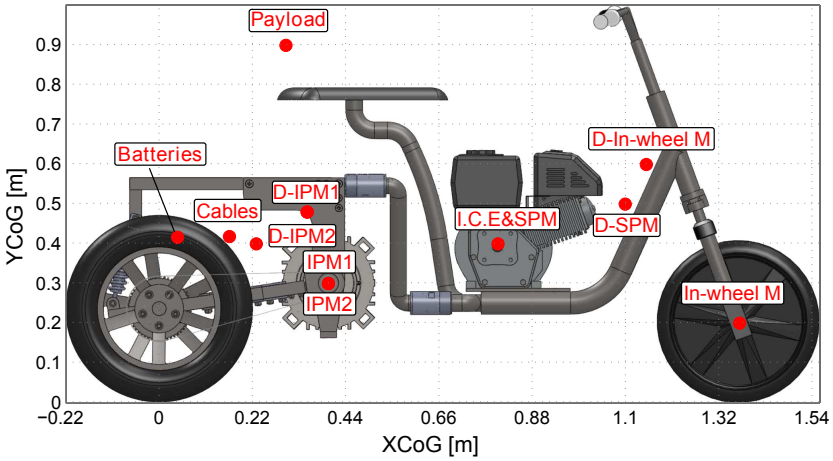

(a)

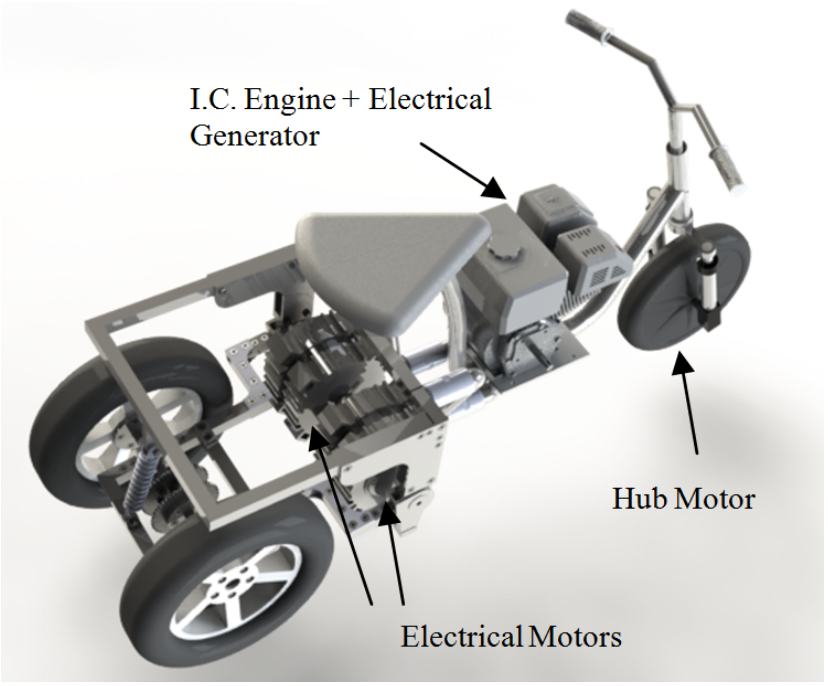

(b)

Figure 5.7: Position of the electrical components on-board.

Figs. 5.8 and 5.9 deal with stability and equilibrium properties of the hybrid vehicle and represent the trajectory of the centre of mass of the front frame and the lateral load transfer respectively. The vehicle is in the standard configuration with the rider and a payload of 70 kg. The curves are parametrized for different lengths of the coupler link (from $0.146\ m$ to $0.186\ m$), whereas the rocker's length and the position of the revolute joints on the non tilting module are kept constant. This means that the instant tilting axis lowers when the length of the coupler link increases, see Fig. 5.1 . Fig. 5.8 shows that the radius of curvature of the trajectory of the centre of mass increases when the coupler's length increases, with a benefit in terms of stability of the vehicle.
Fig. 5.9 shows that the load transfer decreases when the coupler's length increases, with an advantage in terms of equilibrium in steady turning maneuvers. These results show that it is possible to design a safe three-wheeled vehicle well suited to urban and sub-urban mobility.

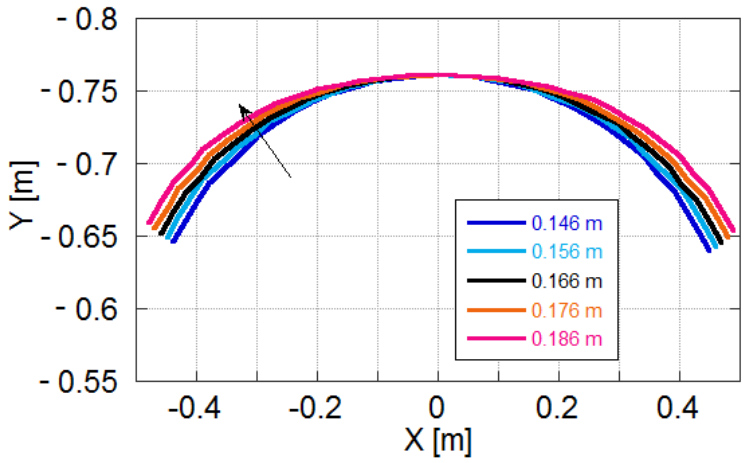

Figure 5.8: Trajectory of the center of mass of the front frame for different length of the coupler link.

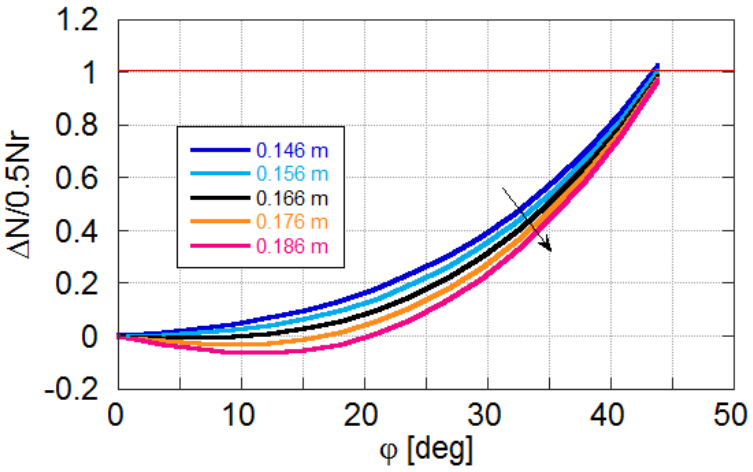

Figure 5.9: Lateral load transfer for different length of the coupler link.

The final geometry of the four-bar linkage is shown in Table 5.2.

Table 5.2: Hy-snake linkage dimensions.

Element	[mm]
Frame (rear module) height	530
Frame length	408
Rockers length	315
Connecting rod length	156

5.1.4 IPM MOTORS

The EM performances have been carried out by means of FE analysis. Simulations have been made with the purpose of maximizing the torque of the EMs with the limitations in terms of space. A particular magnet configuration has been studied to reach the maximum ratio between torque and volume.

Table 5.3: IPM parameters (one motor).

Specification	Symbol	Value	Unit
Max torque	T_{max}	30	Nm
Max speed	n	3000	rpm
Max power	P_{max}	5000	W
Phase current @ T_{max}	I_p	184	A_{pk}
Phase voltage @ ω_{base}	V_p	48	V_{pk}
Pole pairs	p	2	
Stator slots	Q_s	36	
Ext. diameter	D_e	223	mm
Rotor diameter	D_r	139	mm
Air-gap	g	0.5	mm
Iron length	L_{stk}	45	mm
Weight (no case)		13	kg

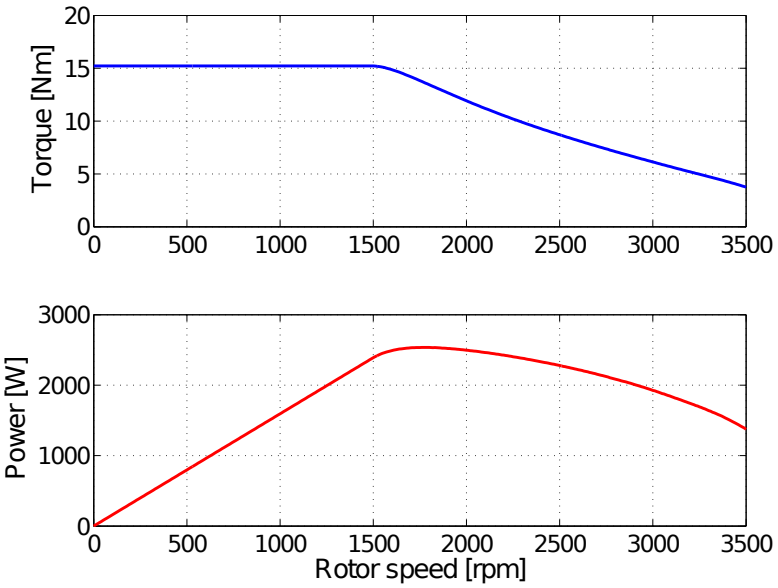

Figure 5.10: Torque and power of one IPM motor.

Table 5.3 collects the main parameter of one IPM motor, whereas Fig. 5.10 shows the torque and the mechanical power of such a motor. Fig. 5.11 shows a magneto-static FE analysis of the IPM machine when it is fed by the rated current.

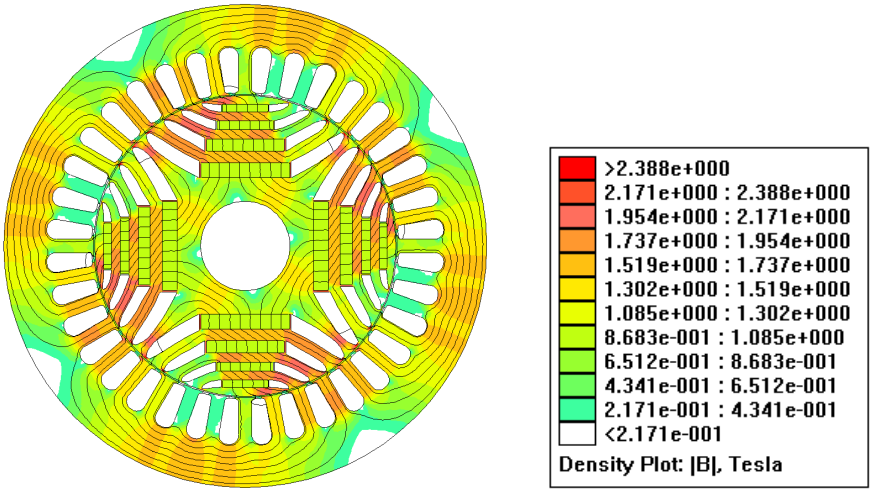

Figure 5.11: Final layout of Hy-Snake.

5.1.5 FINAL PERFORMANCES

Some simulated results are presented to show the potentialities of this vehicle.
Fig. 5.12 shows the total traction force of the vehicle at the wheels. The dotted line represents the force exerted by the front in-wheel motor. The torque of such an EM has been measured experimentally. The solid line represents the force exerted by the two IPM motors and the bold line shows the total traction force at the wheels. The intersection between the latter and the dashed line (that represents the resistant forces) give the maximum speed of the vehicle, that is about 70 km/h.

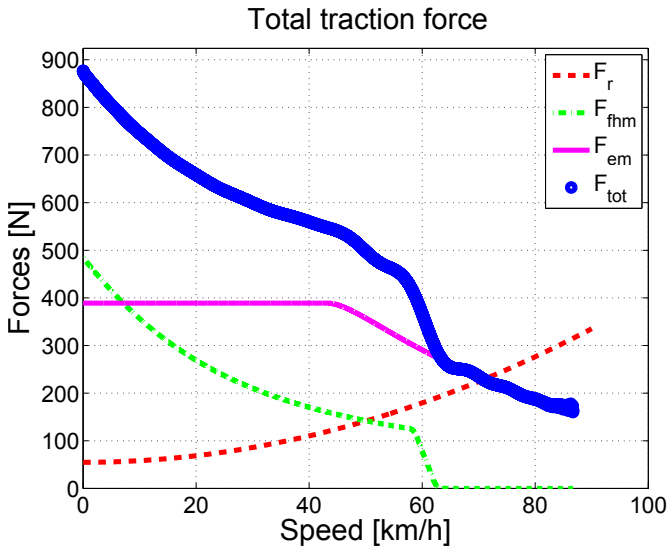

Figure 5.12: Total traction force of the vehicle.

Fig. 5.13 deals with hill starting ability (road grade of 10%) and shows the benefit given by the front-in-wheel motor. Without payload the traction force of the rear motors is hardly enough to overcome the gravity and friction forces and the motors do not reach the rated speed. In this condition the presence of the front motor makes it possible to achieve an acceleration five times higher. With payload (70 kg) the vehicle is able to start only if there is the front

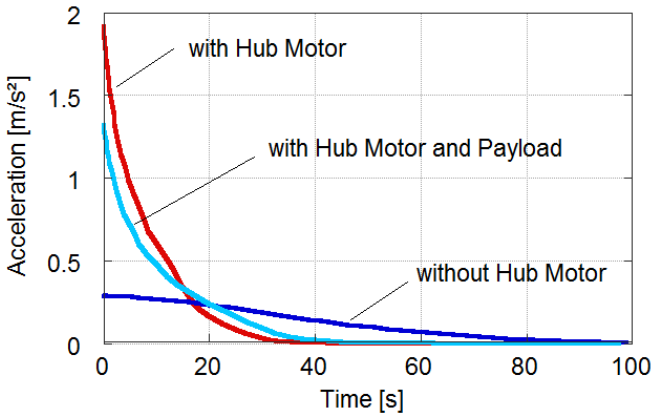

Figure 5.13: Acceleration with road grade of 10%.

in-wheel motor.

The range of the vehicle in urban environment has been estimated considering the ECE-15 cycle (previously presented in Fig. 2.12a). This cycle is also suited to calculate the efficiency of regenerative braking. The estimated range is $40\ km$ in only electric mode and $43\ km$ with regenerative braking. The estimated range in sub-urban environment is about $125\ km$ with a cruise speed of $50\ km/h$. This range is estimated only with the energy generated on-board (without batteries).

Table 5.4: Range results.

Modality	Range $[km]$
Only electric mode	40
With regenerative braking	43
Only with generation on-board @ $50\ km/h$	125

5.2 VELOMOBILE

The project *Velomobile* deals with a research program in the field of urban mobility. Velomobiles or bicycles cars are human-powered vehicles, enclosed for improving aerodynamic performance and protection from weather and collisions. They are derived from recumbent bicycles and tricycles, with the addition of a full fairing (aerodynamic shell) [33].

The purpose of this work is to design and to develop a three wheeled velomobile equipped with a hybrid human-electric propulsion system. The expected performances are maximum speed 70 km/h, maximum acceleration 0.8 m/s^2 and large efficiency of the electrical machine (EM) and of the drive, in order to maximize the range of the vehicle (100 km in electric mode).

The mechanical layout has been developed in order to improve safety: the front frame is tilting and it is connected to the non-tilting rear frame by means of a particular linkage.

The hybrid propulsion system has been developed taking into account the small power involved in this application and the efficiency issues. The advantages of a parallel hybrid propulsion system with full decoupling between human and electric power are described. Then the components of the propulsion system are discussed with special emphasis on the motor.

REL machines are gaining much interest as a candidate for Electric Vehicles (EV) and Human Hybrid Electric Vehicles (HHEV) for its simple and rugged construction, ability of extremely high-speed operation, and hazard-free operation [16, 34]. In view of these characteristics, a particular REL motor has been designed for HHEV applications.

The contents of this chapter have been taken from my personal scientific publication [35], which has won the price as best paper on EV at EVER 2013 conference.

5.2.1 GENERAL LAYOUT OF THE VEHICLE

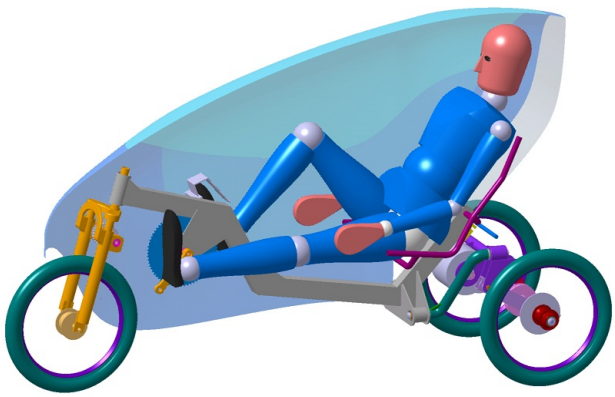

Figure 5.14: CAD 3D of the proposed velomobile.

The modern velomobiles derive from the combination of a recumbent bicycle with a shell. The recumbent bicycle reduces the frontal area and consequently aerodynamic resistance. The shell also improves the aerodynamic performance, it gives protection from rain and wind. At last, it makes safer the vehicle in case of collision. The presence of the shell makes difficult the use of feet to guarantee equilibrium at zero or very low speed (e.g. when stopping at a cross road). For these reasons most velomobiles are equipped with three wheels. There are velomobiles with two front wheels and one rear wheel or with one front wheel and two rear wheels. The former solution is similar to a car because it requires a steering mechanism. The

latter requires a simple steering system similar to the bicycle one. Typically, the velomobiles have a narrow track that gives advantages in terms of reduction of space to run and to park, but it limits the maximum speed in curve. Actually, if centrifugal force is large, the narrow track leads to a large transverse load transfer between the wheels that can cause the rollover of the vehicle. To the aim of overcoming the rollover problem, some tilting velomobiles have been proposed. The first part of the research was aimed to select the best layout for a hybrid velomobile. The demanded performances and the previous experience in the field of three-wheeled vehicles [5, 36] suggested to develop a semi-tilting vehicle with a tilting front module that includes the front wheel, the rider and the shell and a rear module that includes two wheels that do not tilt. Without the electric propulsion system the mass of the tilting module is about 80% of the total. The main advantages of this layout are:

- When the vehicle negotiates a curve, the moment generated by the centrifugal force of the tilting module is balanced by the moment generated by the gravity force (like in bicycles) and the risk of rollover is reduced.
- There is only one tilting front wheel that can be simply supported like a bicycle wheel and can be steered by a simple mechanism.
- There is a lot of room at low level between the two rear wheels, it can be used for accommodating weighty electric components.

The main limits of this layout together with the corresponding solutions are described in the following:

- When velocity is very small, the tilting mechanism has to be locked, to guarantee equilibrium without the intervention of the rider's feet. In this case, the presence of an electric energy source makes easier the development of a locking device based on an electromagnet.
- The transmission of human power from the pedals to the wheels requires a special mechanism. If human power has to be transmitted to the rear wheels, the mechanism has to compensate for the tilting motion. If the human power has to be transmitted to the front wheel, the mechanism has to compensate for the steering motion. The second solution seems to be well suited into a parallel hybrid propulsion system, because it makes possible to use simultaneously electric power delivered to the rear wheels and human power delivered to the front wheel, without requiring a planetary gear transmission to combine the two power fluxes.
- The tilting motion of the shell may lead to interference with the non-tilting rear module. This problem has been solved with a careful design with the aid of simulation tools.

5.2.2 HUMAN HYBRID POWER TRAIN

The possible missions of the vehicle have been defined and the specifications in terms of torque, power and energy consumption have been stated. The torque requirement is related to the maximum acceleration, maximum road grade and total mass, which has been defined with the aid of the first CAD model of the vehicle. The power requirement is related to maximum speed and resistances: aerodynamic drag, internal frictions and rolling resistance. Specific experimental tests have been carried out by means of a rotating disk machine [37] to identify the rolling resistance coefficient of bicycle tires. Table 5.5 summarizes the parameters for the calculation of resistances and the total mass of the vehicle without the electric components i.e. EM, drive and batteries.

Table 5.5: Parameters for the calculation of resistances

Specification	Value	Unit
Drag coefficient	0.15	–
Frontal section area	1	m^2
Rolling resistance coefficient	0.0025	–
Additional friction forces	2	N
Vehicle mass (without el. components)	22	kg
Rider mass	80	kg

A comparison between a series-hybrid and parallel-hybrid propulsion system has been carried out. The series-hybrid configuration includes an electric generator mechanically coupled with the pedals and an electric motor connected to the rear wheels. Since the power delivered by a medium cyclist is typically $250\ W$, [38] a small sized generator has to be adopted. Electric losses in this case are a significant fraction of input power. They decrease the global efficiency of the series power train, which has been estimated equal to $50\ \%$.

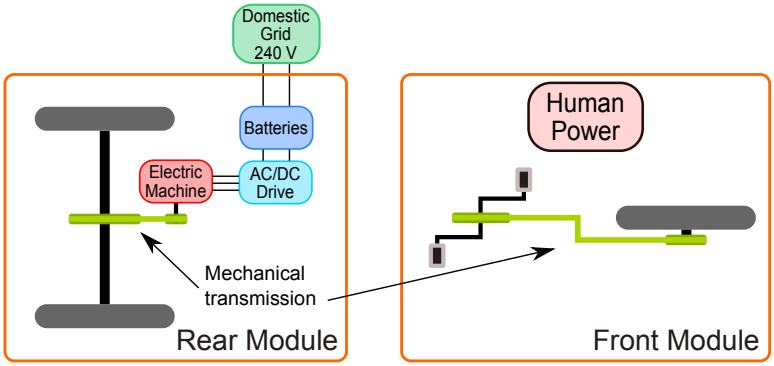

Figure 5.15: Parallel human-electric hybrid power train.

In the parallel hybrid propulsion system the human power is delivered through the pedals that are connected to the front wheel by means of a chain drive. Electric power is delivered by the battery that supplies the power converter and the EM, which is placed on the rear module and connected to the rear wheels by means of a differential gear, as shown in Fig. 5.15. The electric propulsion system makes possible regenerative braking and backward operations. With this solution, on one hand human power is not affected by the efficiency of the generator but

only by mechanical losses, on the other hand electric energy delivered by batteries is efficiently converted into mechanical power. The estimated efficiency of the parallel power train is 70 %.

5.2.3 DYNAMIC ANALYSIS

ADVANTAGES OF FOUR-BAR LINKAGE

The main problem involved in riding three wheeled velomobiles is rollover, even at moderate speed. To avoid this problem, the innovative solution developed in [31, 39] for three wheeled vehicles has been implemented in the velomobile.

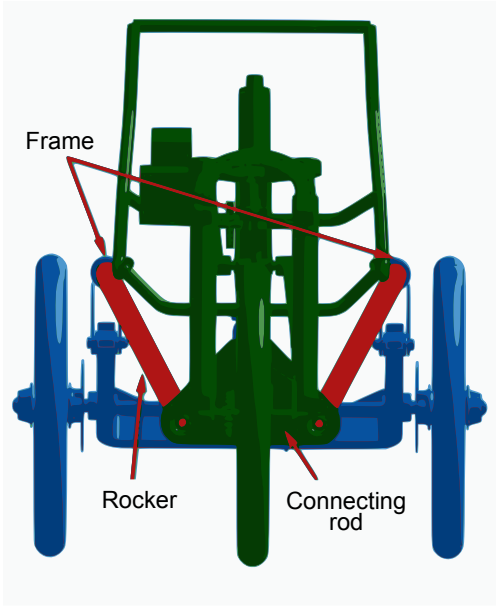

(a)

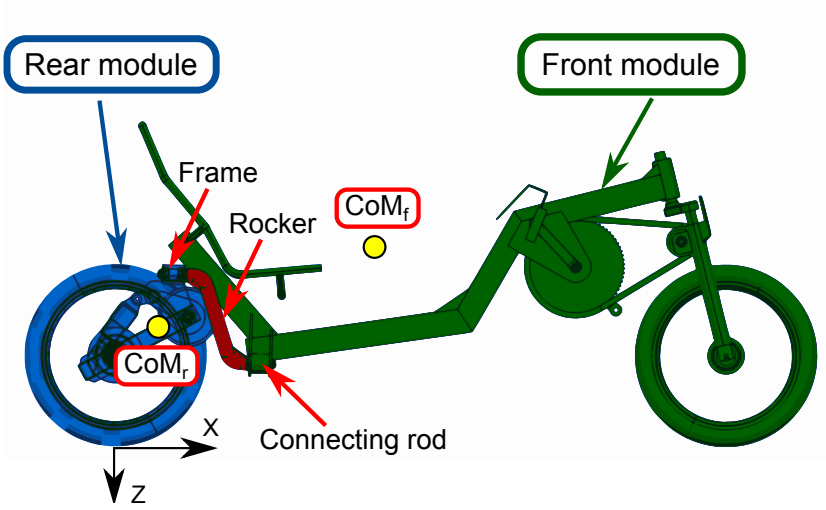

(b)

Figure 5.16: a) The four-bar linkage connection, b) Reference frame and CoM positions.

The front and rear modules of the velomobile are connected by a couple of rockers and four revolute joints as shown in Figs. 5.16a and 5.16b. In this way the rear module, the two rockers

and the front module form a four-bar linkage in which the front module is the connecting rod. The four-bar linkage (Fig. 5.16a) allows the front module of the vehicle to tilt, limiting the load transfer between the rear wheels.

The four-bar linkage gives several advantages with respect to the simple pivot joint because this linkage has an instant center of rotation that can be positioned at road level (or below the road) and moves where the vehicle tilts. By means of a proper design, the position of the instant center of rotation can be adjusted to achieve the desired compromise between stability and handling.

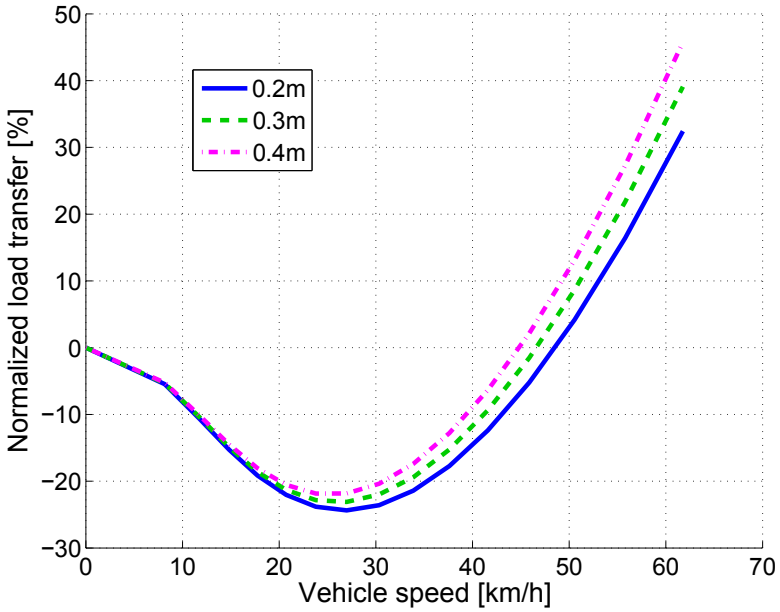

Figure 5.17: Effect of the elevation of the CoM of the rear module (Elevation increases from 0.2 to $0.4\ m$)

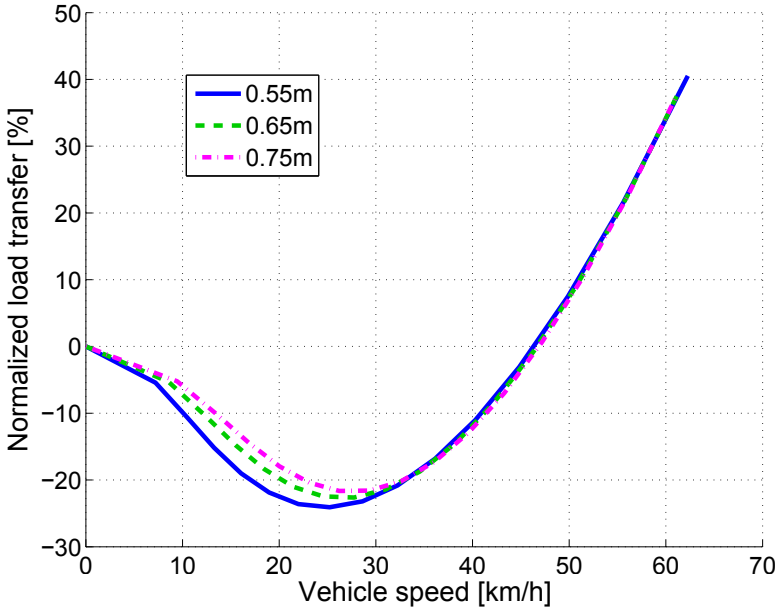

Figure 5.18: Effect of the elevation of the CoM of the front module (Elevation increases from 0.55 to $0.75\ m$).

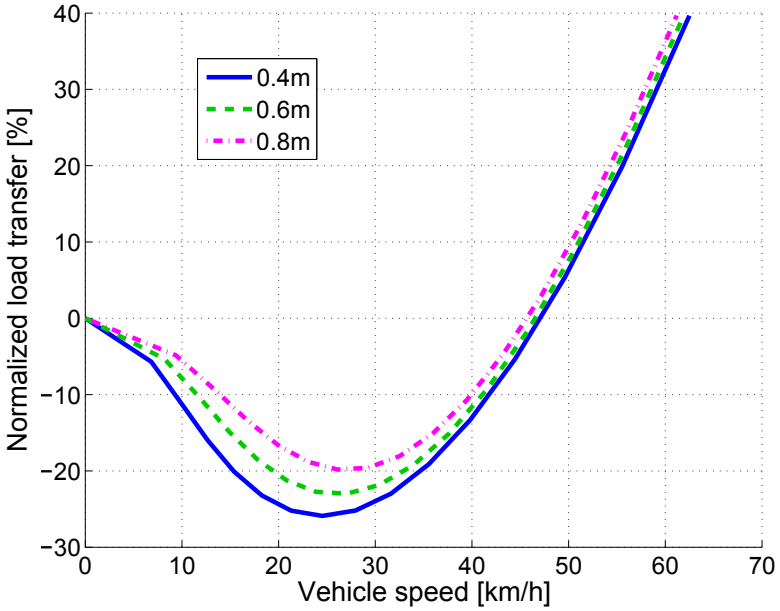

Figure 5.19: Effect of the advancement of the CoM of the front module (Distance from the axle of the rear module increases from 0.4 to 0.8 m).

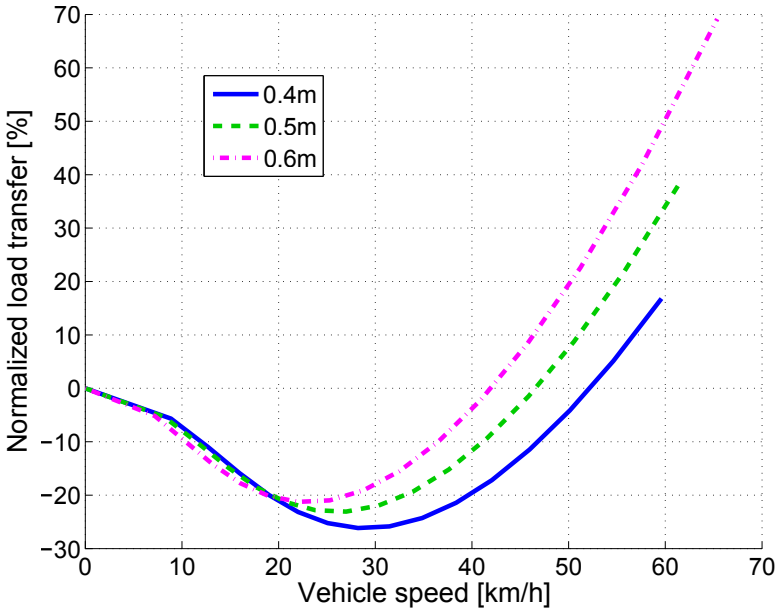

Figure 5.20: Effect of four-bar linkage elevation (from 0.4 to 0.6 m) without altering geometry.

A mathematical model has been developed to analyze the influence of the main parameters of the vehicle (mass distribution and linkage geometry) on rollover. Details of the model can be found in [5, 8]. Steady turning maneuver (curve radius equal to 30 m) at increasing speed, that requires increasing tilt angle, has been considered. Figs. 5.17, 5.18 and 5.19 show the effect of mass distribution on normalized load transfer, which is the ratio between the variation in tire load caused by dynamic effects and tire load in static conditions; when the normalized load transfer is 100% rollover begins. The velomobile here considered is equipped with a four bar linkage with the instant center located on the road plane when the tilt angle is zero. With this kind of linkage, the normalized load transfer is negative at low speed because the load on

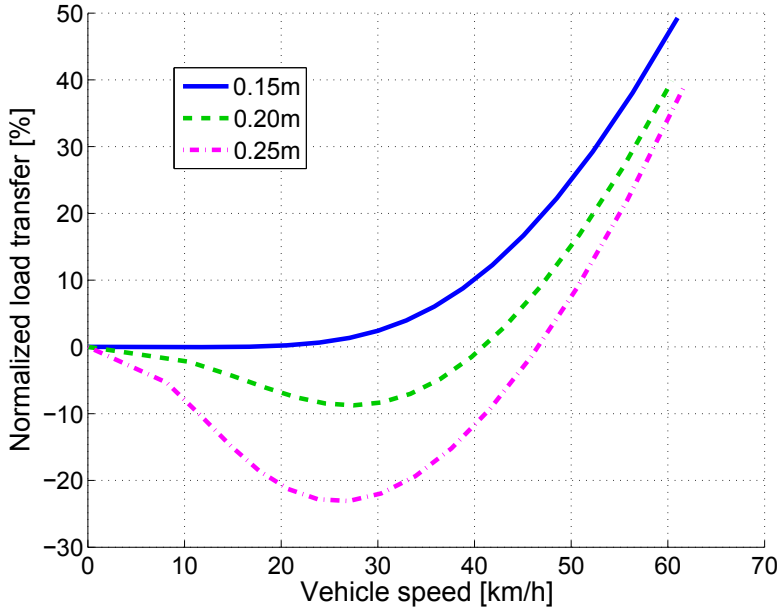

Figure 5.21: Effect of the geometry of the four-bar linkage connecting rod shortens from 0.25 to 0.15 m.

the inner wheel increases. The most important features of the tilting vehicle with linkage are summarized in Table 5.6 and 5.7.
If the elevation of the Center of Mass (CoM) of the rear module increases, the normalized load transfer between the rear wheels slightly increases at high speed, as shown in Fig. 5.17. If the elevation of the CoM of the front module increases, the negative normalized load transfer at low speed decreases in modulus and there is a negligible effect at high speed, as shown in Fig. 5.18. The longitudinal position of the CoM of the front module influences normalized load transfer and rises the curves, especially at low speed, as shown in Fig. 5.19. Figs. 5.20, 5.21 show the effect of the layout of the four bar linkage on normalized load transfer and rollover. If the whole linkage is raised from the road without altering the proportions between the links, normalized load transfer at high speed increases (Fig. 5.20). This condition happens when both front and rear module are raised of same quantity. Fig. 5.21 shows that, if the length of the connecting rod is shortened by reducing the distance between the two revolute joints on the tilting module, normalized load transfer moves toward positive values because the elevation of the instant center increases.

Table 5.6: Linkage Dimensions

Element	[mm]
Frame (rear module) height	500
Frame length	500
Rockers length	280
Connecting rod length	250

Table 5.7: Vehicle masses and CoM (rider included)

	m/m_{tot} [%]	Z [mm]	X [mm]
Front module (CoM_f)	81	-615	594
Rear module (CoM_r)	19	-302	102

MULTIBODY SIMULATIONS

A multibody model of the vehicle has been developed to confirm analytical results and to compare the three possible solutions: non tilting, tilting with pivot, tilting with four-bar linkage.

To compare the tilting solutions, the pivot joint and the connecting rod of the linkage have been positioned at the same height from the road (approximately $250\ mm$ over the road). The instant center of rotation of the linkage was approximately on the road.

Table 5.8: Steering pad performance

link type	[km/h]	radius [m]	load transfer [%]
rigid	24.8	38.5	59
pivot	25.0	31.5	19
4 bar	31.6	32.3	-6

The three vehicles, identical in trim and mass distribution, have been driven through similar steady turning maneuver (constant speed in circular path). Speeds and path radii are not identical because the different vehicles achieve slightly different equilibrium configurations in steady turning, but they are sufficiently similar for comparison purposes.

The results, which are summarized in Table 5.8, show large differences in load transfer between the rear wheels. As expected the worst case is achieved with the non tilting vehicle, in which the normalized load transfer reaches about 60%. Both the pivot and four-bar linkage solutions are safer compared with the non tilting vehicle, but only with the linkage the normalized load transfer is dramatically reduced. As a consequence, at higher speeds only the four-bar linkage solution can avoid rollover risks.

5.2.4 SYNCHRONOUS RELUCTANCE MACHINE

The EM designed for this application is a REL motor with inner rotor and outer stator whose section is sketched in Fig. 3.3. It is characterized by a rated torque of 7 Nm and a maximum peak power of 1.2 kW at 2100 rpm. The key parameters of the EM are summarized in Table 5.9. The EM is controlled by means of a traditional low-voltage bidirectional power converter (MOSFET based).

In the design of this REL motor, the main attention has been given both to minimize torque ripple and to maximize efficiency in order to extend the range of the vehicle.

By means of this model it has been possible to carry out simulations for choosing the optimal shapes of the flux-barriers. This model allows to determine the impact of flux-barrier geometry on the torque ripple. In addition it allows to highlight the torque harmonics of different order. The results are reported using maps, as that shown in Fig. 5.22 referring to the

Table 5.9: EM parameters.

Specification	Symbol	Value	Unit
Max torque	T_{max}	7	Nm
Max speed	n	3000	rpm
Max power	P_{max}	1200	W
Phase current @ T_{max}	I_p	42.28	A_{pk}
Phase voltage @ ω_{base}	V_p	28.24	V_{pk}
Pole pairs	p	2	
Stator slots	Q_s	36	
Ext. diameter	D_e	150	mm
Rotor diameter	D_r	95.2	mm
Air-gap	g	0.4	mm
Iron length	L_{stk}	70	mm
Weight (no case)		8.27	kg
Phase resistance	R_{ph}	44.9	$m\Omega$
Saliency	ξ	6	

torque ripple due to the 72^{th} harmonic. Optimal angles of the flux-barriers have been obtained from Fig. 5.22. The harmonic of such order corresponds to the second slot harmonic (the slot harmonics have order $\nu_{sh} = Q_s/p \cdot k$ where k is a positive integer). Fig. 5.22 presents constant torque ripple loci for different angles of the flux-barrier ends (for the first and the second barrier). The angle of the third flux-barrier end has been fixed to $\vartheta_{b3} = 38\ mech\ degrees$. A "Machaon" configuration has been adopted to further reduce the torque ripple, [40]. In this way two different poles have been designed by means of the angles specified in Fig. 5.22. A sketch of the REL motor is presented in Fig. 3.3 showing different flux-barrier geometries.

Fig. 5.23 shows the torque ripple versus rotor angle when different skew angles are applied. In particular, dashed lines highlight the torque ripple computed considering the whole rotor in the following positions: $-4, -2, 0, 2$ and $4\ mech\ degrees$. The solid line gives the mean value of the previous contributes. Referring to Fig. 5.23, the design optimization allows to reduce the torque ripple to 4% with respect to the rated torque, but not to cancel completely the phenomenon, even if a continuous skewing is adopted.

OPTIMAL CURRENT VECTOR TRAJECTORY

The results obtained by FE simulations have been analyzed in order to implement the optimal current vector control. Fig. 5.24 shows the optimal current vector control trajectory during the nominal (red solid line) and the overload (red dotted-dashed line) conditions in the d-q axis current plane. Due to saturation effects the optimum α_i^e along the MTPA trajectory is not constant and becomes higher than $45\ degrees$ (as in a non-saturated REL machine) as the current increases.

A key feature of the REL machines is that the maximum speed is only limited by mechanical stresses because there are no permanent magnets inside the flux-barriers. As a consequence REL machines can operate in a wide speed range. They are also safe because they are charac-

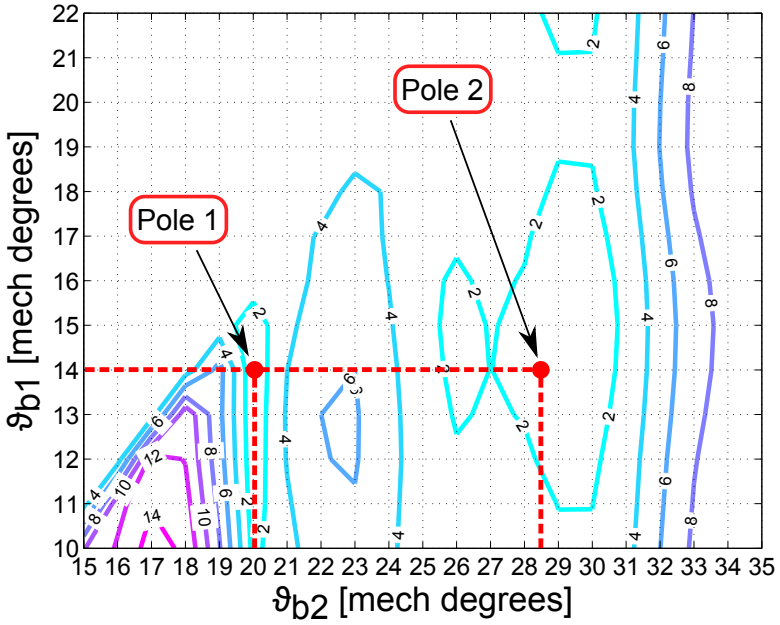

Figure 5.22: 72^{th} torque ripple harmonic map (mech period), $\vartheta_{b3} = 38\ mech\ degrees$.

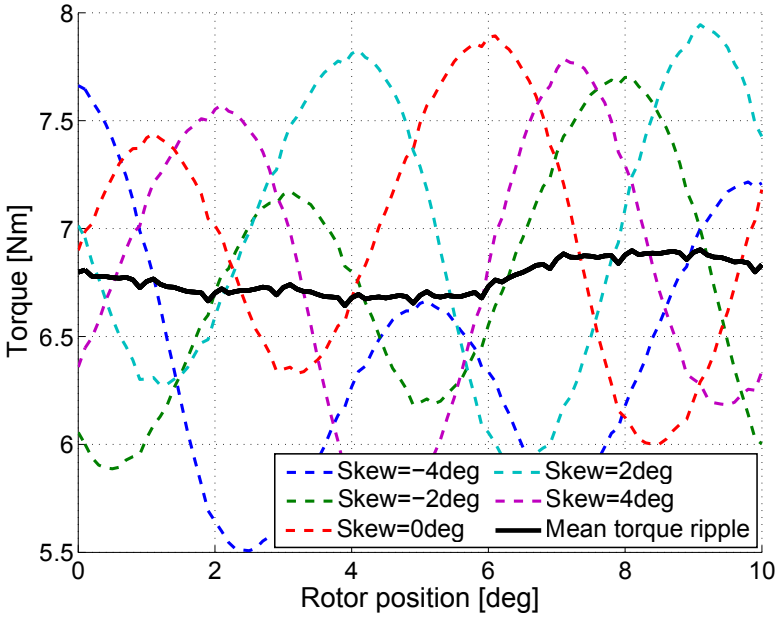

Figure 5.23: Torque ripple for different skew angles varying rotor position (only one slot rotation is shown, even if the period is three slots).

terized by no back electromotive-force (emf) and thus by zero short-circuit-currents in case of fault.

Fig. 5.25 reports the torque and power characteristics versus rotor speed. Solid lines indicate torque and power characteristics in rated conditions whereas dashed lines show the same quantities in overload conditions.

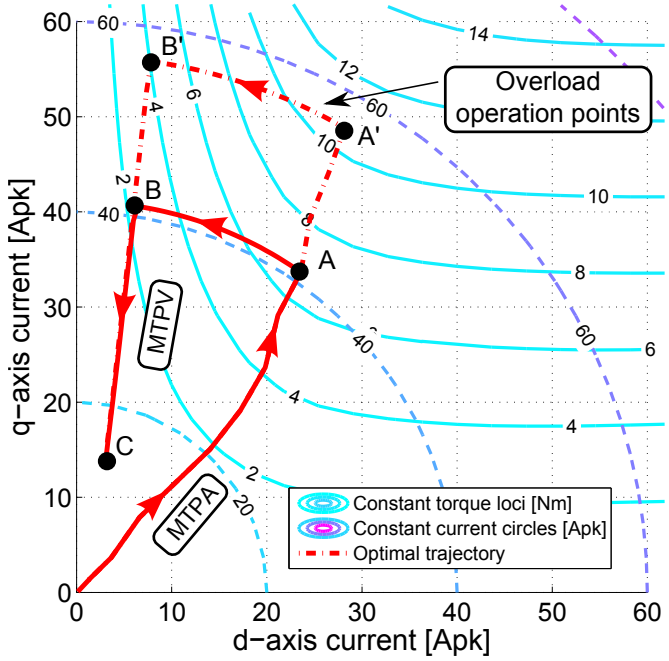

Figure 5.24: Optimal current vector trajectory with operating regions.

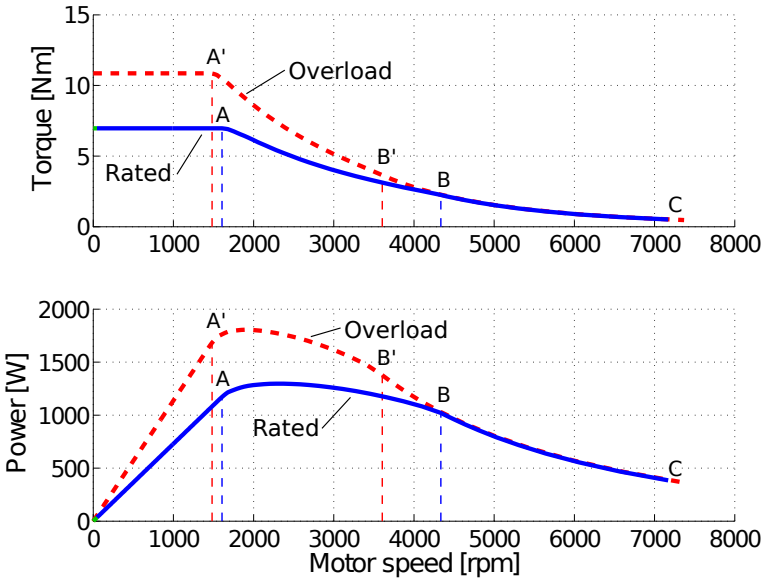

Figure 5.25: Torque and power of the REL motor, when the current vector moves along the optimal trajectory in rated and overload conditions.

EFFICIENCY MAP

In order to reduce the required motor torque (and hence its volume) the REL machine is connected to the rear wheels by a chain drive whose transmission ratio is equal to 4. A mechanical differential is required to allow relative rotations between the two rear wheels during cornering maneuvers. This configuration makes it possible to place the EM on the chassis (becoming a sprung mass) with advantages in terms of comfort of the vehicle.

The efficiency map of the REL motor in the plane of force versus forward speed is shown

in Fig. 5.36, to check the operation points of the EM. This map has been obtained by FE simulations taking into account copper losses, iron losses and mechanical losses. Referring to Fig. 5.36 the black solid line shows the nominal traction force (referred to the rear wheels) delivered by the REL motor whereas the dotted-dashed curve refers to the overload operating conditions. The equivalent forces referred to the rear wheels are computed as:

$$F_{traction} = \frac{T_{REL}\,\tau_{ratio}\,\eta_{chain}}{R_{rw}} \tag{5.1}$$

where T_{REL} is the REL motor torque, τ_{ratio} is the transmission ratio, η_{chain} is the efficiency estimated for the transmission (equal to $98\ \%$) and R_{rw} is the rear wheel radius (equal to $0.263\ m$).

The red dashed line shows the resistant forces (i.e. aerodynamic, rolling and additional forces, see Table 5.5) that the velomobile has to overcome in a straight running at constant speed (i.e. without considering the forces needed to accelerate the vehicle).

Considering that the working points belong the dashed line, corresponding to constant forward speeds of the vehicle, it is worth highlighting that the efficiency of the REL motor moves form 78 to $88\ \%$ when the forward speed is into the range $20 - 70\ km/h$.

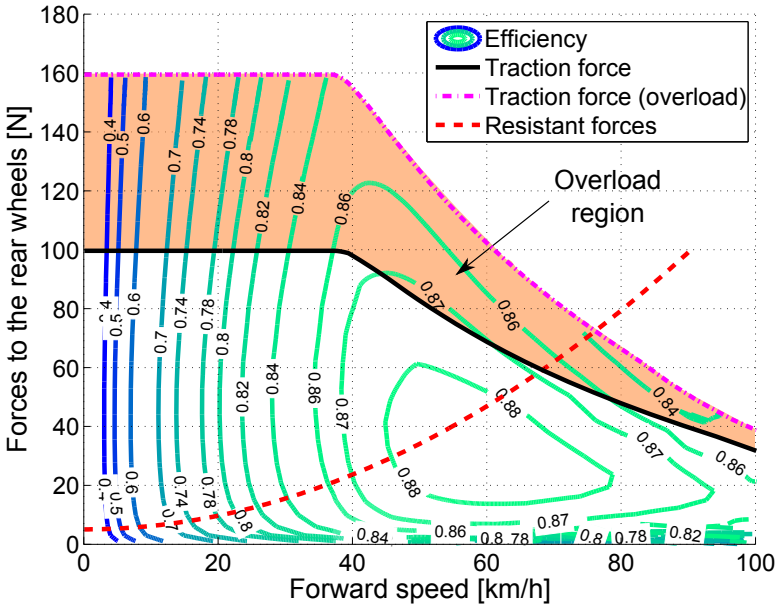

Figure 5.26: Efficiency map in the plane force vs forward speed of the vehicle, in nominal and overload conditions.

ROTOR DEFORMATION ANALYSIS

Large deformations of the EM rotor may compromise the shape of the flux-barriers that have been optimized to reduce torque ripple and to maximize efficiency. For this reason some FE analysis of the rotor have been carried out. Deformations in the plane perpendicular to the shaft axis are the most dangerous. The main loads acting in the radial direction are centrifugal and magnetic forces and the main load in the tangential direction is the electromagnetic torque. The displacements of two annular surfaces at the extremities of the rotor are locked, to simulate the constraint given by the screw-nut system.

Simulations have been performed in two conditions:

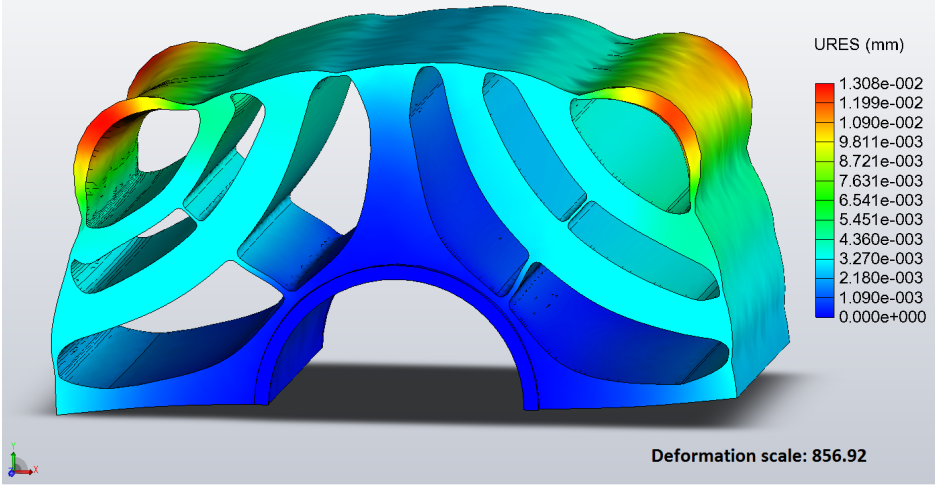

Figure 5.27: Deformation analysis of the rotor, when the speed is 1500 rpm and the maximum torque is 10.8 Nm.

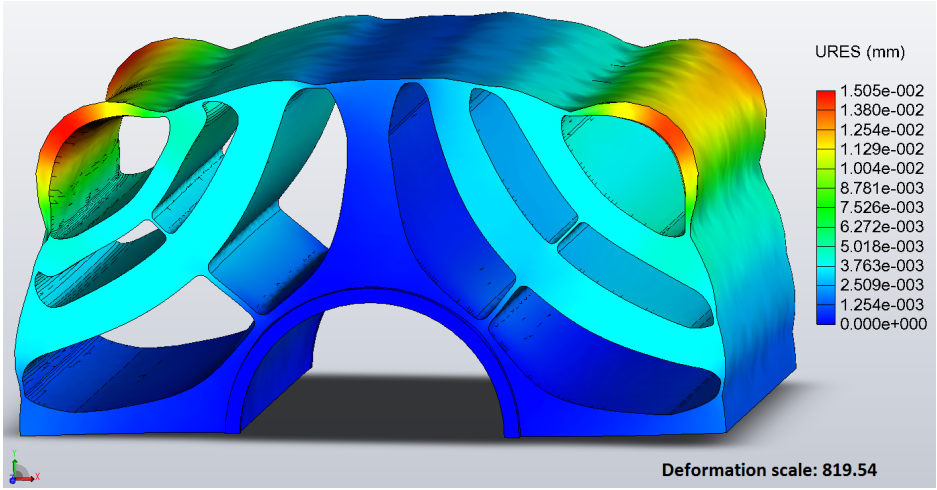

Figure 5.28: Deformation analysis of the rotor, when the speed is 3000 rpm and the torque is 5 Nm.

1. at maximum torque (overload) and rated speed (1500 rpm) to verify the effect of the torque, as shown in Fig. 5.27;

2. at maximum speed (3000 rpm) and overload torque to check the effect of centrifugal forces, as shown in Fig. 5.28.

Simulation results show the deformed rotors and the displacements in both the conditions stated above. The largest displacement occurs on the external surface of the rotor, above the first flux-barrier in condition 2). Its value is 15μm and it is directed chiefly in the radial direction. At maximum speed, Fig 5.28, centrifugal forces mainly impact on rotor deformation. At rated speed, Fig. 5.27 the effect of the torque acting on the external rotor surface is relevant as highlighted by the deformation along the direction of rotation.

Anyway, neither the air-gap between stator and rotor, nor the flux-barrier are compromised by these deformations.

5.2.5 FINAL PERFORMANCES

Table 5.10: Final performances (only electric mode)

	Value	Unit
Batteries weight	11.5	kg
EM+drive weight	11.8	kg
Auxiliary components	5.7	kg
Total vehicle mass (included rider of $80\ kg$)	131	kg
Max acceleration (overload)	1.4	m/s^2
Max velocity (overload)	76	km/h
Max road grade	10	$\%$
Range (@ $35\ km/h$)	115	km

The weights of electric components (i.e. EM, drive and batteries) have been taken into account in the calculation of resistances due to the motion. The energy consumption has been computed on a custom cycle at constant velocity ($35\ km/h$) using high performance lithium-polymer batteries ($48\ V,\ 40\ Ah$).

Table 5.10 summarizes the main features of the designed vehicle and the performances in the pure electric mode.

In order to evaluate the performances of the velomobile in both hybrid and human modes an estimation of the power generated by the pedaling legs of the rider has to be made. Results of experimental tests carried out by means of cycloergometers show that a well trained rider is able to generate in steady state conditions a propulsive power of $250 - 300\ W$ at the cadences of 100 and $80\ rpm$ respectively [41, 42]. The corresponding propulsive torques have values in the range $25 - 35\ Nm$. The analysis of acceleration performance in the human and hybrid mode requires the knowledge of the torque that the rider is able to exert in transient conditions, this torque is lower than the one in steady state conditions, because a share of the muscular torque is used for accelerating the legs.

If the acceleration of the crank-set is lower than $2\ rad/s^2$, the moment of muscular torques in transient conditions is lower than $-4\ Nm$, therefore a propulsive torque of $26\ Nm$ has been assumed for the calculations.

The traction force can be calculated from the propulsive torque taking into account the transmission ratios of the chain and gearbox, which are summarized in Table 5.11.

Fig. 5.29 shows the traction forces that can be generated in the three operating modes against vehicle velocity. The traction force in the pure human mode takes into account that the rider shifts the gear when the cadence reaches 80 rpm (red dots). The traction force curve intersects at $32\ km/h$ the curve of the total resistant force and this velocity is the maximum one that can be reached in the pure human mode.
The curve of the traction force in the pure electric mode derives from the overload torque of Fig. 5.25 taking into account the transmission ratio between the angular velocity of the motor and the rear wheels (4) and the rolling radius $(0.26\ m)$. This curve intersects the resistant force curve at $76\ km/h$, this is the maximum velocity in the pure electric mode.

Table 5.11: Transmission ratios from the pedals to the front wheel

Transmission ratios	1^{st}	2^{nd}	3^{rd}
Front chain		3.3	
Gearbox	0.527	1	1.615

Finally, the curve of the traction force in the hybrid mode is the sum of the human and electric contributions. It is assumed that the rider stops pedaling when (with the highest gear) he overcomes the maximum cadence (85 rpm). Since in this case the velomobile reaches high speeds in a very short time, only one gear shifts has been considered staring the motion with the second gear. It is worth highlighting that in the hybrid mode the rider is able to exert pedaling torques at higher speeds than in the pure human mode, because the electric motor helps him to overcome the resistant forces. Figs. 5.30a and 5.30b show acceleration and vehicle velocity against time. In the human mode the maximum acceleration is about $0.4\ m/s^2$ and in the pure electric mode the maximum acceleration is about $1.2\ m/s^2$. The hybrid mode gives the largest acceleration (about $1.4\ m/s^2$). It is worth highlighting that in the hybrid mode the large change in the slope of acceleration caused by the achievement of the base speed of the electric motor (point A' in Fig. 5.25) takes place about 1 second earlier than in the pure electric mode, because the human propulsion helps the vehicle to increase the speed. Fig. 5.30b shows that the human propulsion allows the vehicle to reach in a shorter time the cruising speed, if it is lower than the maximum cruising speed.
Finally Fig. 5.30c shows the rider cadence during the human and hybrid operating modes. In the hybrid mode the rider has to shift the gear 6 s after the begin of the motion, because of the electric assistance. In this operating mode only one gear shift is allowed since the vehicle reaches quickly high speeds and the motion starts with the gear set up on the second speed ratio.

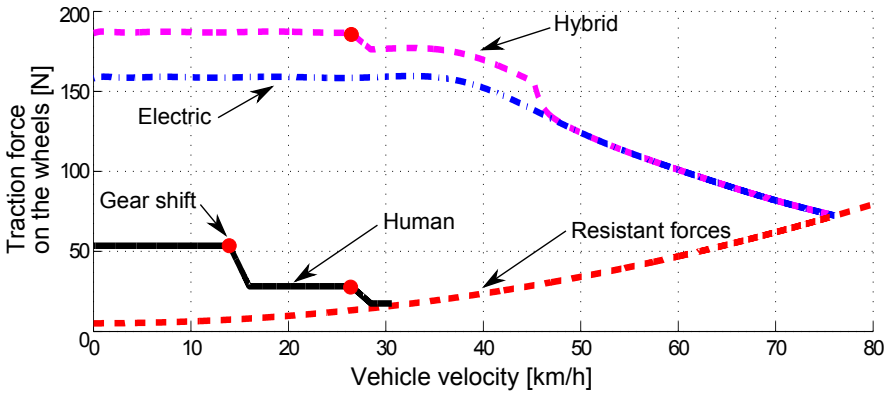

Figure 5.29: Traction forces on the wheels in human, electric and hybrid operating modes.

A prototype velomobile (Fig. 5.31), based on the design concepts developed in the framework of this research, has been manufactured and now road tests are being carried out. First results are satisfactory.

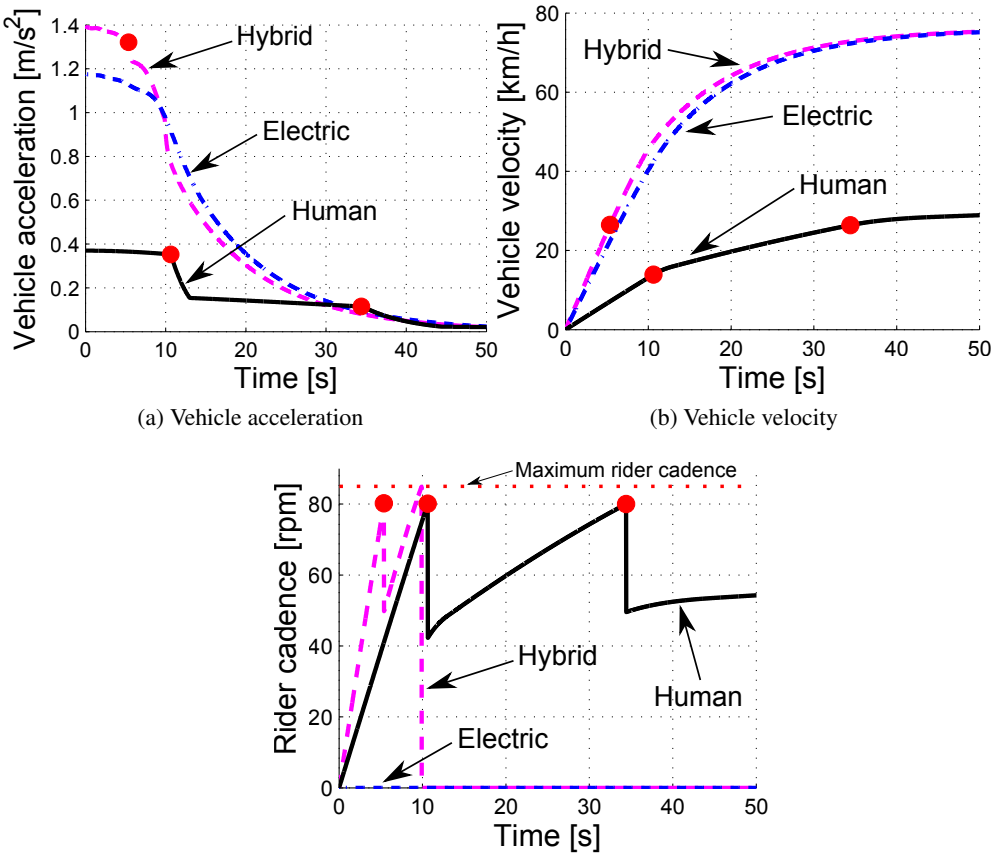

(a) Vehicle acceleration

(b) Vehicle velocity

(c) Rider cadence

Figure 5.30: Acceleration and velocity of the vehicle and rider cadence in human, electric and hybrid operating modes.

Figure 5.31: Velomobile prototype.

5.3 APRILIA RS4 125 HYBRID

The project "Aprilia RS4 125 Hybrid" deals with a regional research program in the field of urban mobility.

In recent years,the interest for mild HEVs is growing up, mainly for fuel saving and emissions reduction, [43,44]. In motorcycles the transition from conventional ICE vehicles to HEVs is very attractive but there are still open issues and possible optimizations to be investigated in order to optimize the size and the weight of the electric parts on-board. The Energy Storage System (ESS) in HEVs is the most critical part of the propulsion system. Its principals requirements are low weight, volume, cost, but conversely it should have high power (performance), high energy density (range), long lifetime, and high reliability. The different type of energy sources complement drawbacks of each single device, [45]. Typically the ESS is composed by different kind of technologies i.e., Ultracapacitor, [46], LiPo, [47], NiMH, [48], and lead-acid [49]. The power provided by the ESS is a function of the power demand and braking regeneration power imposed by the vehicle during driving cycles [50]. In this work a simple but effective solution of motorcycle hybridization has been designed in order to improve the performance of the original vehicle when the torque of the ICE is low, i.e. at low rotating speeds. In order to study the performance of the vehicle a careful analysis of the vehicle has been made. The chosen solution has been validated by means of a motorcycle prototype which has been tested on a specific test bench and on racetrack.

The contents of this chapter have been taken from my personal scientific publications: [51, 52]. The latter has been selected for plenary presentation at the Electric Machines Drives Conference (IEMDC) 2013.

The motorcycle that has been chosen to realize the hybrid prototype is Aprilia RS4 125. The reference is a standard 125 single cylinder four stroke motorcycle with six-speed gearbox, weight of $147\,kg$, wheelbase of $1360\,mm$, maximum torque of $10.7\,Nm$ at $8000\,rpm$ (as shown in Fig. 5.33) and maximum power lower than $11\,kW$ ($15\,CV$ at $9250\,rpm$) according with the limitations in force. The original on-board generator is connected to the $12\,V$ battery and delivers up to $180\,W$.

Figure 5.32: Aprilia RS4 125.

The goal is to improve the performance of the reference motorcycle (in terms of torque) by replacing the conventional generator with a new EM suited to improve the torque of the original ICE and to reduce emissions.
The EM will be directly connected to the ICE shaft in order to realize a parallel hybrid solution. The target is to increase the original ICE torque at low speed, as it is reported in Fig. 5.33, in order to satisfy the user's requirements without increasing maximum power for complying the motorcycle standards. Fig. 5.33 shows by dashed-dotted line the original ICE torque, by solid line the combined one and by dashed line the EM torque.

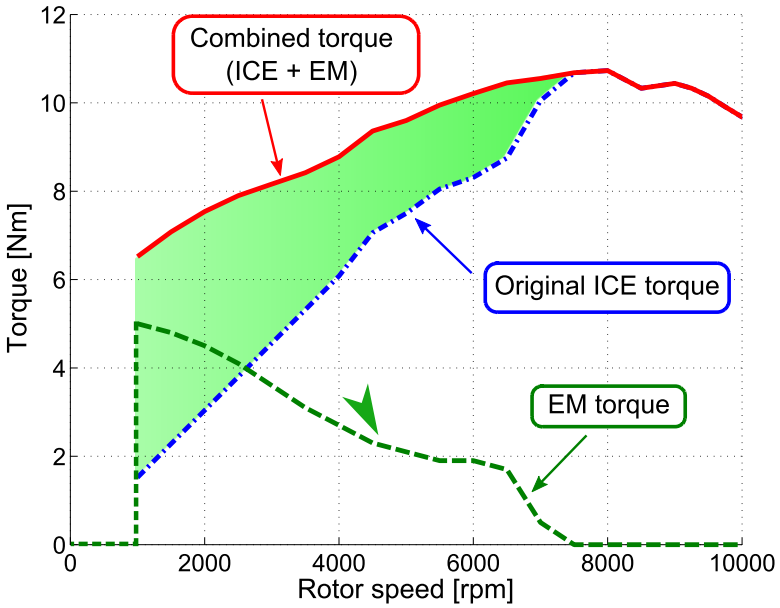

Figure 5.33: ICE and combined torque

5.3.1 POWER-TRAIN OVERVIEW

The motorcycle has been investigated by means of FE simulations, in order to find the most effective power train compatibly with constrains of low weight, volume and cost but with high performances. As a consequence, the power-train architecture is composed by an ICE directly connected to an SPM machine, a bi-directional single-stage power converter and an ESS. The whole power-train is shown in Fig. 5.34. A Vehicle Management Control Unit (VMCU) manages and controls the system.

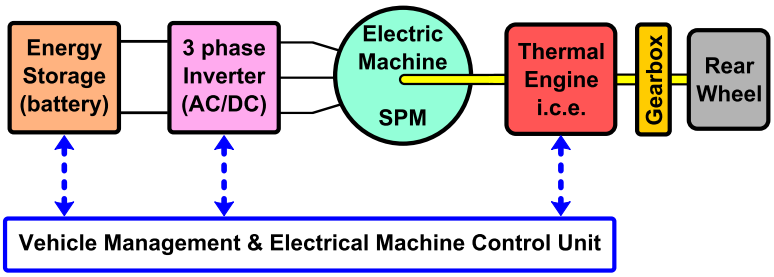

Figure 5.34: Power-train sketch overview.

5.3.2 PERFORMANCE OF THE ELECTRICAL MACHINE

An EM, as that considered in this work, connected to the ICE is commonly called integrated Starter-Alternator (ISA), [53]. ISA machine tasks are: ICE start-up, power boost, generating on-board of electrical energy, and regenerating braking.

The original alternator has been substituted with a more powerful EM in order to satisfy the requirements in terms of torque and power as shown in Fig. 5.33. Since the position of the EM on the motorcycle was fixed by the old alternator, the maximum dimensions were limited. The new EM has been designed in order to accommodate a maximum diameter of $155\ mm$ and a maximum length of $62\ mm$. An SPM machine with outer rotor and inner stator has been developed for space saving reasons and Fig. 5.35 shows the prototype of the stator. A concentrated winding is also adopted in order to reduce the copper weight, cost and also Joule losses. The rated torque of the EM is $6.7\ Nm$, delivered up to $6000\ rpm$ (even if it's not required), the peak torque is $10\ Nm$ and the maximum speed is higher than $8000\ rpm$. Table 5.12 collects EM data including geometrical parameters (i.e. external diameter, stack length, pole and slots number) and electric parameters (i.e. rated phase current and voltage, phase resistance and inductance and so on). Machine performances have been estimated by means of FE analysis. Copper losses (5.2), iron losses (5.3) and mechanical losses (5.4) have been taken into account (into the EM working regions) calculating the efficiency map presented in Fig. 5.36. The real EM working points are also drawn to verify the effective efficiency achieved. The equations used for losses calculation are also reported. In particular copper losses are:

$$P_j = 3RI^2 \tag{5.2}$$

in which R is the winding phase resistance and I is the phase current. Iron losses are estimated

Table 5.12: Electric machine parameters.

Parameter	Value
Pole number	18
Slot number	27
External stator diameter	$135\ mm$
Stack length	$35\ mm$
Type of magnet	Ferrite
Rated torque	$10\ Nm$
Rated phase current	$25\ A_{pk}$
Rated phase voltage	$220\ V_{pk}$
Phase resistance	$75\ m\Omega$
Phase inductance	$230\ \mu H$
External Phase inductance	$120\ \mu H$
Magnet flux linkage	$0.024\ V_{pk}s$
Rated speed	$9000\ rpm$
Average efficiency	$80\ \%$
Weight	$5\ kg$

by:

$$P_{iron} = P_{s,steel}\left(k_{hyst}\frac{f}{50} + k_{ec}\frac{f^2}{50^2}\right)\left(\frac{B}{1}\right)^2 \tag{5.3}$$

where $P_{s,steel}$ is the specific loss of the lamination steel (given at $B = 1\ T$ and $f = 50\ Hz$) and k_{hyst}, k_{ec} are two coefficients that indicate the contribution of hysteresis and eddy currents losses respectively. Finally the mechanical losses are calculated by the empirical equation:

$$P_{mech} = \left(kP_N\sqrt{N}\right)\left(\frac{n}{N}\right)^3 \tag{5.4}$$

where k is a coefficient equal to $0.6 \div 0.8$, [54], P_N is the rated mechanical power (in kW) at the rated speed N and n is the rotor speed expressed in rpm.

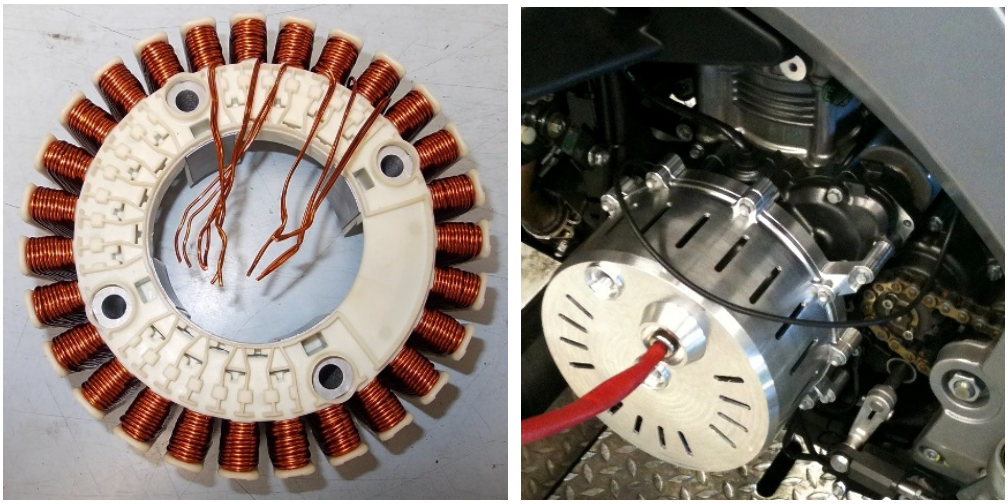

(a) (b)

Figure 5.35: SPM machine prototype.

5.3.3 PERFORMANCE OF THE ELECTRIC CONVERTER

The power converter, that has been adopted for this hybrid motorcycle, is a bi-directional single-stage topology. It is a simple but effective three-phase half-bridge converter, its DC bus is direct connected to the vehicle battery pack whose voltage, V_{DC}, is fixed to 450 V. The power converter characteristics are reported in Table 5.13 and Fig. 5.37 shows the inverter prototype.

In order to estimate the average inverter efficiency in the hybrid vehicle working points a losses analysis has been carried out. The dominant factor in the total power losses of power converter are the conduction losses and switching losses in the devices. The estimate efficiency in all drive working points has been computed by using the device information, that has been reported in its datasheet, [55]. The switching losses, P_{SW}, and conduction losses P_{ON} with IGBT devices have been calculated by following formulae, [56]:

$$P_{SW} = (E_{on} + E_{off})F_{SW} \tag{5.5}$$

$$P_{ON} = V_D I_D \tag{5.6}$$

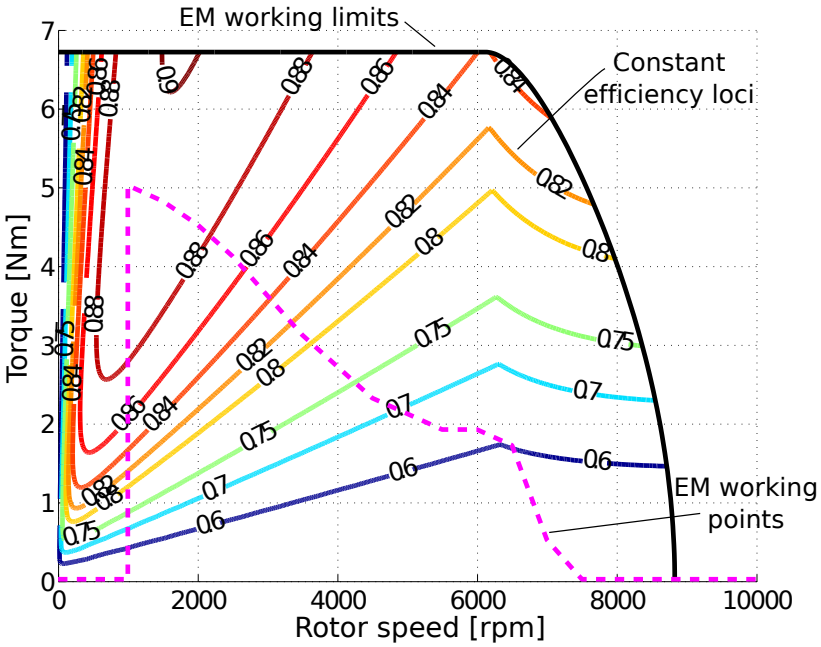

Figure 5.36: SPM machine efficiency map.

Table 5.13: Three-phase inverter parameters.

Parameter	Value
Number of phases	3
Type of switch	IGBT
Switching frequency	20 kHz
Dead time	2 μs
Maximum DC bus voltage	500 V
Rated AC current	25 A_{pk}
Rated AC voltage	220 V_{pk}
Average efficiency	90 %
Weight	3 kg

where I_D and V_D is the current and the voltage of the device respectively, F_{SW} is switching frequency, E_{on} the turn-on switching energy and E_{off} turn-off switching energy. These energies are proportional to device current and for example are $E_{on} = 2\ mJ$ @ $30\ A$ and $E_{off} = 0.65\ mJ$ @ $30\ A$. (5.5) and (5.11) have been used to calculate the total losses of electrical drive and also the power consumption of the converter control can be included and it is estimated in the worst case as $10\ W$. The converter efficiency in the torque vs rotor speed plane has been reported in Fig. 5.38. The estimated average efficiency is more than $90\ \%$.

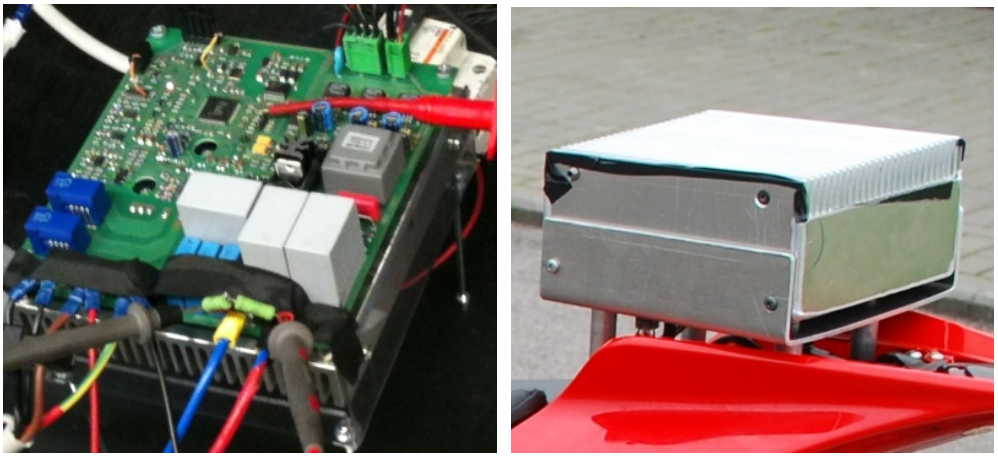

(a) (b)

Figure 5.37: Three-phase inverter prototype.

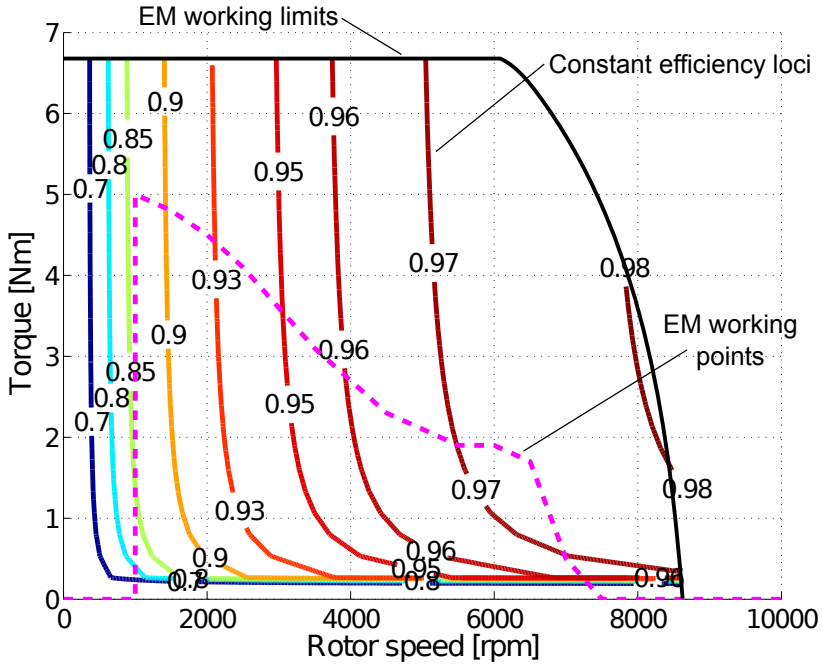

Figure 5.38: Power converter efficiency map.

5.3.4 ENERGY STORAGE SYSTEM (ESS)

In order to estimate the energy and the power required to the ESS a reference driving cycle called *World-wide Motorcycle Emissions Test Cycle* (WMTC) has been chosen. The WMTC cycle is commonly used to verify the consumption of fuel and the emissions for motorcycles. Since the reference motorcycle has a total displacement of 124.8 cc, the WMTC cycle is restricted to urban and sub-urban simulations (no highway) for a total time of 1200 seconds, as show in Fig. 5.39. To the aim of estimating the amount of energy required to the ESS, it is necessary to define a strategy of use for the EM: boost effect during acceleration times and intelligent charge of the ESS when the speed is constant or decreases.
For this purpose it has been used a reference ESS that can be discharged/charged as the EM demands.

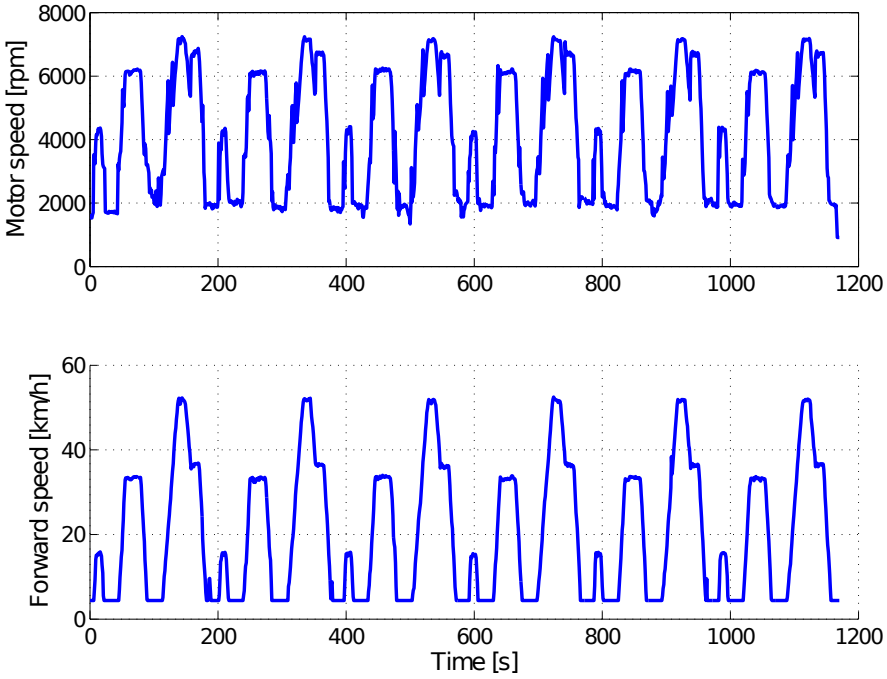

Figure 5.39: World Motorcycle Test Cycle for 125cc motorcycles.

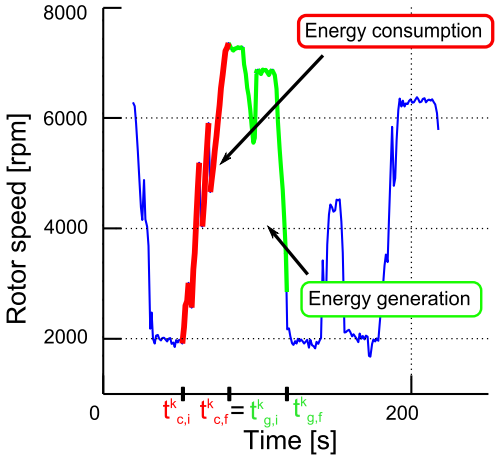

Figure 5.40: Energy approach.

A specific Matlab® code has been developed to analyze the telemetries and testing the strategy of use by means of an energetic approach. Referring to Fig. 5.40 a graphical example of energy consumption calculation is highlighted with the red area (left side). The analytical expression of such an area is shown by means of (5.7), in which the EM speed is expressed in rad/s and the EM torque is achieved by the dashed green characteristic (*EM torque*) reported in Fig. 5.33. The energy consumption, E_c, for each interval $k-th$ is estimated in (5.7) and the total amount of energy in (5.8):

$$E_c = \int_{t_{c,i}}^{t_{c,f}} \frac{EM_{speed} \cdot EM_{torque}}{\eta_{tot}} \, dt \tag{5.7}$$

$$TOT\ E_c = \sum_{K_c=1}^{n_c} E_c \tag{5.8}$$

where t_c is the discharge interval, the subscripts $_i$ and $_f$ indicate initial and final instants of a generic interval $k-th$, n_c represents the total number of discharge interval, and η_{tot} indicates the efficiency of the whole power train.

The same approach has been used for the charging intervals by means of (5.9) and (5.10) that show the energy generation, E_g for each interval $k-th$, and the total one respectively:

$$E_g = \int_{t_{g,i}}^{t_{g,f}} EM_{speed} \cdot EM_{torque} \cdot \eta_{tot}\, dt \tag{5.9}$$

$$TOT\ E_g = \sum_{k_g=1}^{n_g} E_g \tag{5.10}$$

The first graph of Fig. 5.41 shows the strategy of use applied to the WMTC cycle.

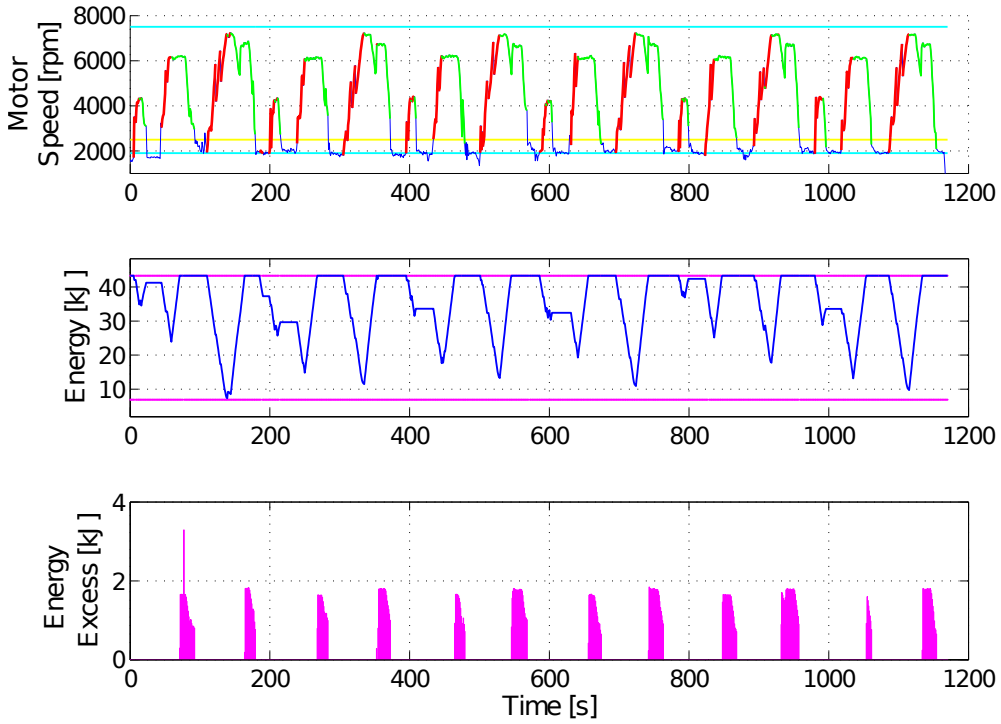

Figure 5.41: Telemetry analysis and energy flow inside the reference ESS.

According with the torque profile shown in Fig. 5.33 the second graph of Fig. 5.41 shows the energy flow inside the reference ESS during the test cycle.This graph is useful to define the maximum deep of discharging and therefore the amount of energy required to the ESS.
The third graph of Fig. 5.41 shows the surplus of charge that can't be stored in the ESS (i.e. when the ESS is totally charged).

It is worth noticing that since the speed profile of the WMTC cycle is fixed (and also the transmission ratios) the rotating speeds of both ICE and EM are the same in both conventional and hybrid configurations. By means of the strategy of use explained above, it is possible to drive the WMTC cycle with a low fuel consumption. This is due to the torque given by the EM during accelerations. Therefore to match the WMTC speed profile, the throttle aperture will be lower than in conventional motorcycle.

Simulation results highlight that the required peak power results equal to $1800\ W$ during the boost phase and equal to$-1500\ W$ during the regenerative braking phase. The required peak energy during WMTC test cycle is $10\ Wh$.

In order to choose the best ESS for such HEV, Ragone chart has been used, [57, 58]. Fig. 5.42 shows an example of Ragone chart used to evaluate the energy storage performance of various technologies.

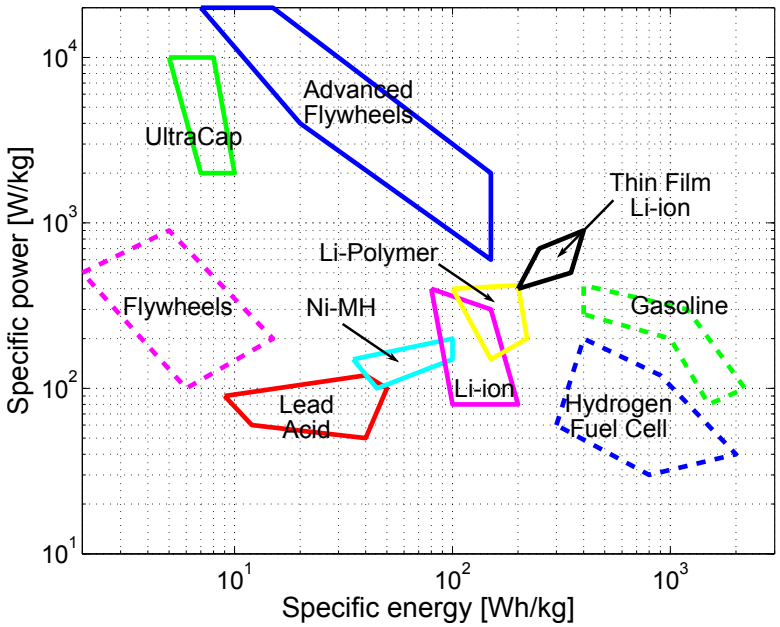

Figure 5.42: Ragone chart.

Since the maximum power required during the motoring phase is $1.8\ kW$, the Ragone chart [**?**] has been redrawn as function of weight and energy as shown in Fig. 5.43. A significant parameter, especially in motorcycles, is the weight. In order to choose the best technology it is necessary to fix the weight limit for the ESS; in this case it has been chosen equal to $20\ kg$. Therefore, referring to Fig. 5.43 all the technologies with weight lower than $20\ kg$ could be well suited providing the minimum amount of energy is higher than $10\ Wh$.

In this study flywheel and hydrogen fuel cell ESSs have not been taken into account. As a consequence the considered ESS technologies are those presented in Fig. 5.44, highlighting their main features. Spider charts report the results on a scale 0 to 1 that corresponds to a poor and an excellent performance respectively [59]. It is possible to underline that NiMH battery is a good compromise in term of cost, volume and weight compared to Li-poly battery and ultra-capacitors. Therefore the NiMH battery has been adopted as ESS for the HEM prototype. The principal parameters of the NiMH battery pack have been reported in Table 5.14 whereas the adopted batteries pack is shown in Fig. 5.45.

In order to investigate the efficiency of the battery pack in all working points Joule losses have been taken into account considering a simple model reported in [60]. The internal resistance of the batteries pack is $R_{int} = 2\Omega$. Such value has been shown in [61] and it allows to calculate the Joule losses in the ESS by:

$$P_{Joule} = R_{int} I_{bat}^2 \tag{5.11}$$

The result of this analysis is shown in Fig. 5.46 and the estimated average efficiency is about $96\ \%$.

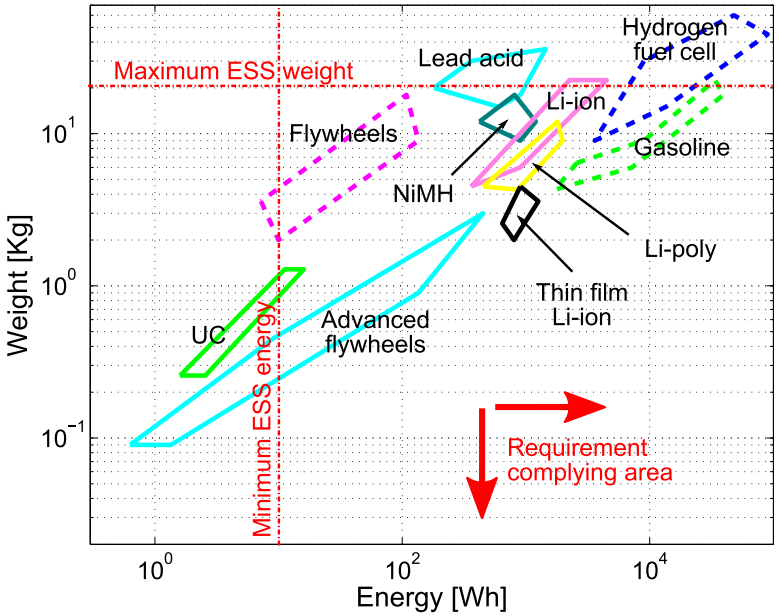

Figure 5.43: ESS maximum power has been fixed at 1800 W @ 1 C and the minimum energy is 10 Wh and the maximum weight is 20 Kg.

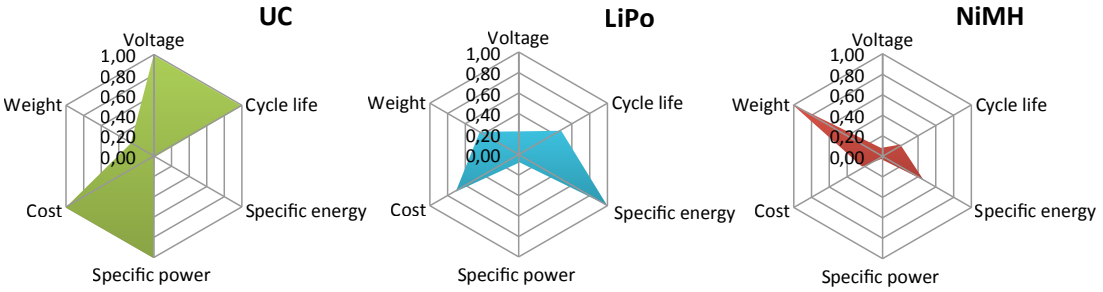

Figure 5.44: ESSs comparison.

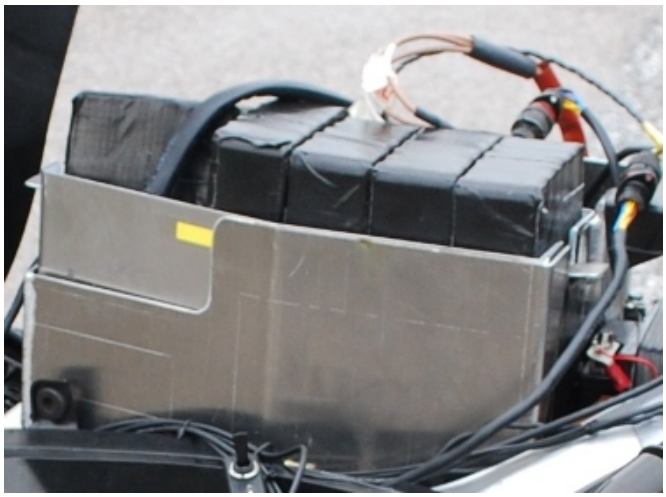

Figure 5.45: Prototype Ni-MH batteries pack.

Table 5.14: Battery pack parameters.

Parameter	Value
Type of battery	Ni-MH
Cell nominal voltage	$1.2\ V$
Cell typical capacity	$1.8\ Ah$
Cell internal impedance	$75\ m\Omega$@$1\ kHz$
Cell diameter	$14\ mm$
Cell height	$50\ mm$
Number of cells in series	350
Maximum battery voltage	$450\ V$
Maximum discharge current	$18\ A$
Maximum charge current	$1.8\ A$
Weight	$11\ kg$

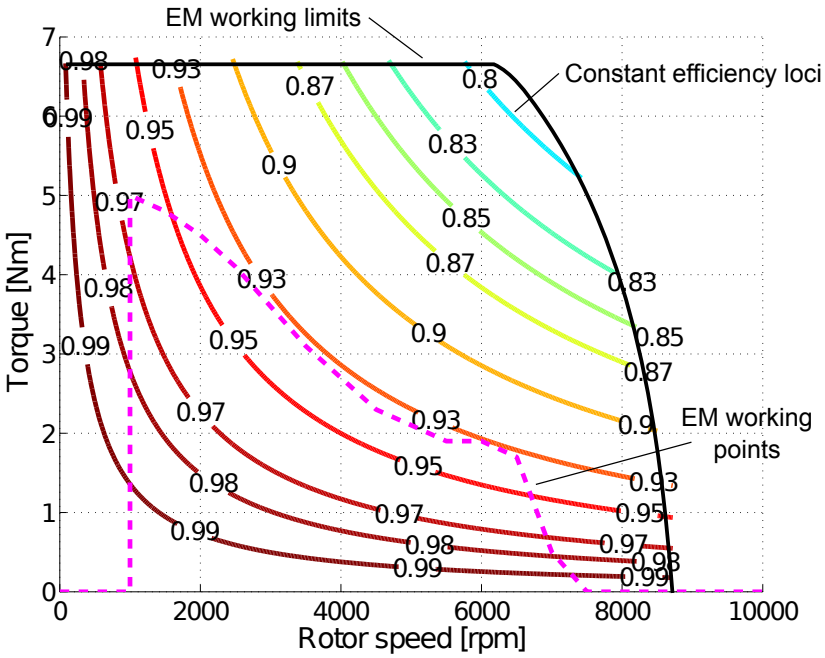

Figure 5.46: Battery efficiency map.

5.3.5 CONTROL UNIT

The HEM performance is monitored by a Vehicle Management Control Unit (VMCU). The torque and power profiles, reported in Fig. 5.33, have been stored into the control unit. In the VMCU two operating modes have been implemented:

- **Motoring mode** (M): the power is transferred from the ESS to the engine shaft by means of the power converter and EM. This operating mode has been implemented during engine startup or accelerating boost.
- **Generating mode** (G): the power is transferred from the engine shaft to ESS by electric generator and power converter. This operating mode has been implemented during the regenerating brake and the battery charge. In both phase the torque of the EM is controlled according with ESS constraints or rather the current and voltage limits of the battery. In order to control the battery voltage, a simple battery voltage control loop has been implemented, using a PI regulator.

Referring to these two operating mode the EM control scheme becomes as reported in Fig. 5.47. It highlights that, in this case, the inventer control unit is composed by EM torque control (motoring phase) and battery voltage control (generating phase).

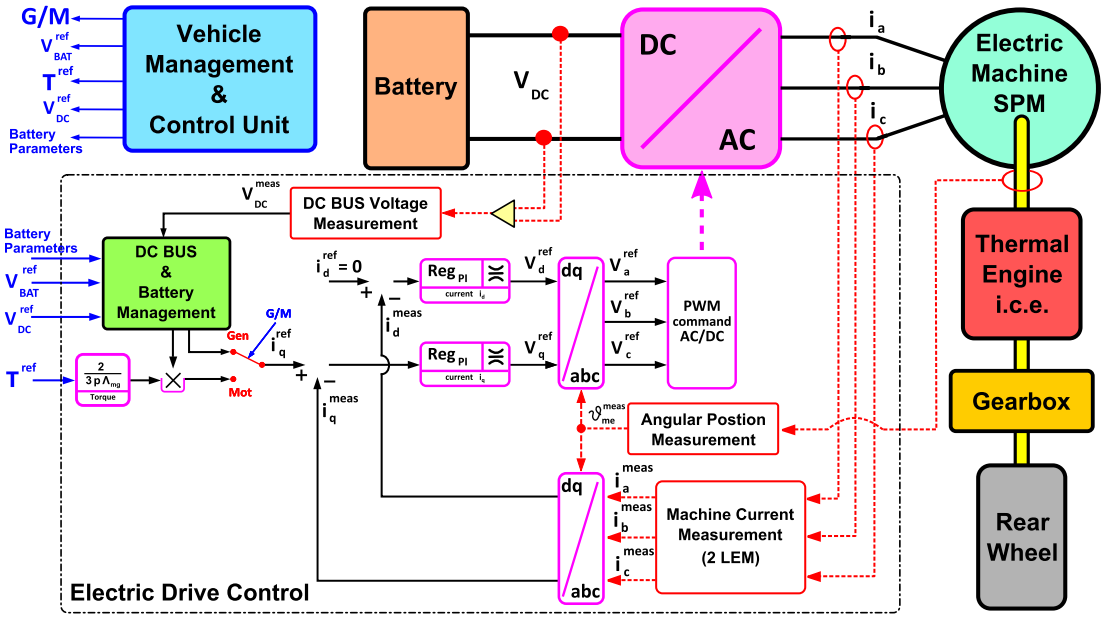

Figure 5.47: HEM control scheme overview.

The main EM control technique adopted for both operating modes is a torque control. Therefore, in order to generate high torque the stator current vector have to be synchronized with the rotor polar axis (d-axis). To this purpose a simple and economical solution has been adopted; a phonic wheel has been used for sensing the rotor position.

In addiction two current loops are implemented and the electric machine is controlled to comply with the MTPA trajectory. Hence, according to the constant torque loci of the adopted EM reported in Fig. 5.36, the current reference of d-axis current loop is maintained to zero while the q-axis current loop is related to torque demand. In this axis the reference current is positive during motoring phase and negative during generating phase.

Such vehicle control strategy and the torque profile of Fig. 5.33 have been implemented inside of the Aprilia APX_2 control unit. Some pictures of VMCU prototype is shown in Fig. 5.48.

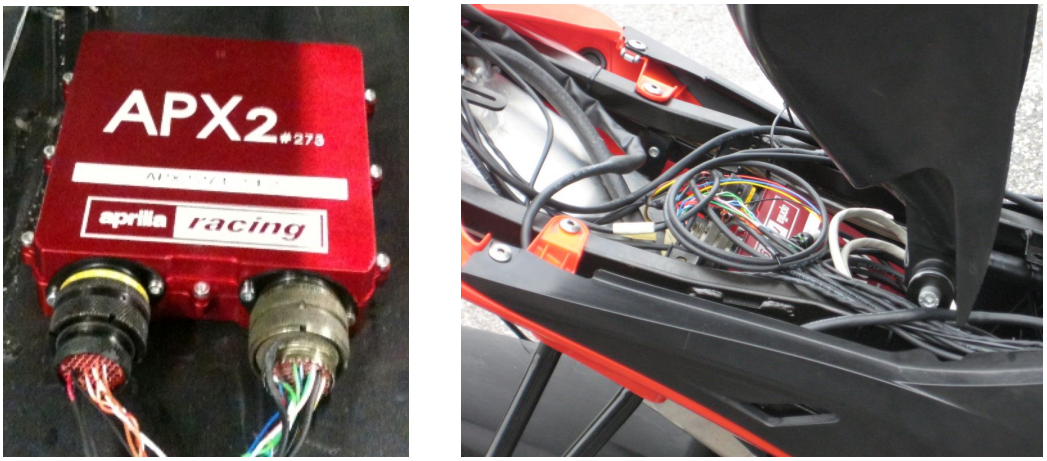

(a) Aprilia APX_2 (b) On-board allocation

Figure 5.48: Prototype of vehicle management control unit.

5.3.6 HEM PROTOTYPE

The HEV prototype is shown in Fig. 5.49. It is worth noticing that the original Aprilia RS4 125 has not been overall modified too much. It underlines a good integration of the new components in the original motorcycle.

The original tank ($14.5\ l$) has been substituted with a smaller one ($5\ l$) and placed under the motorcycle saddle. In this way the space occupied by the original tank has been used for the batteries pack without altering the vehicle profile. The new EM has substituted the original alternator and the EM carter support has been further increased due to the new EM larger size. The inverter has been placed behind the rider and above the passenger seat. The VMCU has been located below the motorcycle saddle.

The introduction of such electric components leads to increase the motorcycle weight to about $15\ kg$, which is a good result because this value corresponds to $10\ \%$ of the original weight.

TEST BENCH MEASUREMENTS

In order to verify the new performances of the proposed HEM, at first the motorcycle has been tested by a specialized test bench inside the Aprilia s.p.a. company site and after that it has been tested in a small private racetrack inside the Piaggio s.p.a. company site respectively.

The adopted Aprilia's test bench is shown in Fig. 5.50.

The mechanical performance of the HEM has been measured with appropriate instruments able to reconstruct the ICE shaft torque from the measured braking torque to the rear wheel. Electrical quantities have been measured by means of a Wattmeter that has been connected to the DC bus between the batteries pack and the power converter.

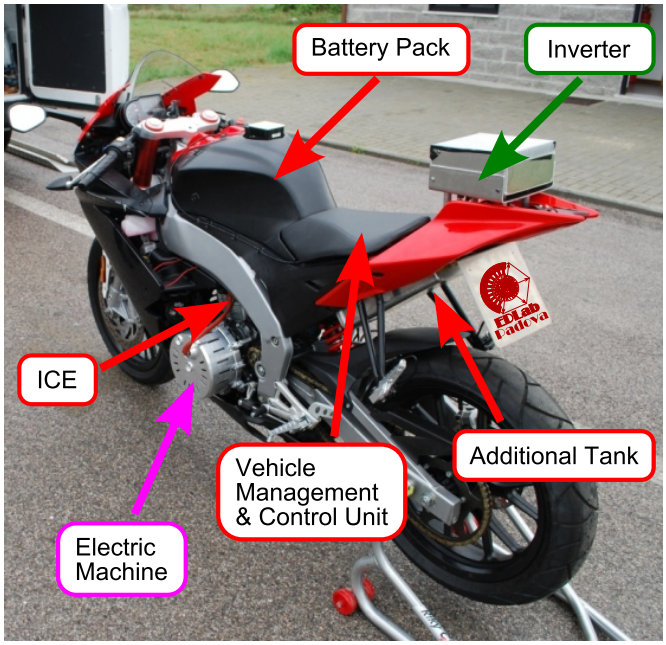

Figure 5.49: Prototype HEV overview.

(a) (b)

Figure 5.50: Prototype HEV under test in Aprilia's test bench.

Fig. 5.51 shows the EM performance acquired at the Aprilia's test bench. For given rotor speeds (i.e. 1000 rpm, 2000 rpm, ...) the EM has been controlled manually increasing its current from zero to the rated one (i.e. with increasing torque). The rotor speed has been fixed by means of the test bench regulating the speed of the rear wheel of the motorcycle and the throttle aperture. Experimental results confirm that the EM can deliver the required torque in all working points during the motoring mode.

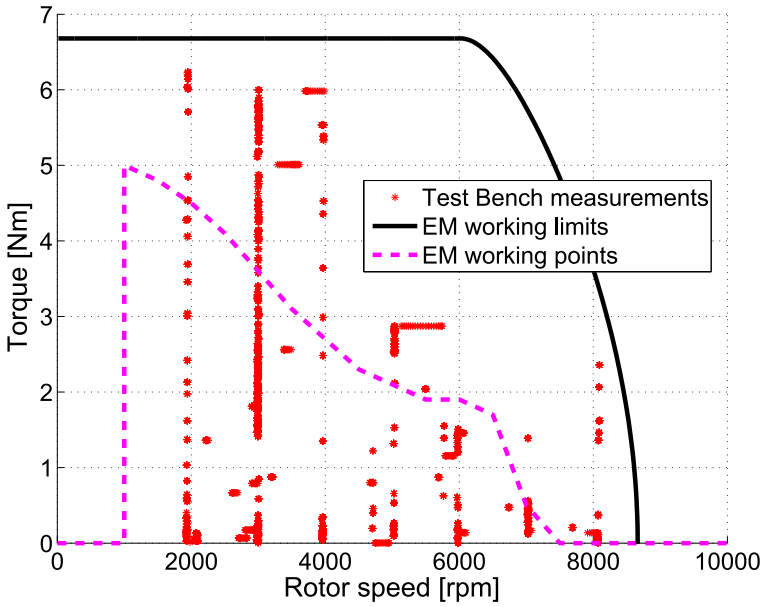

Figure 5.51: Test bench performance measurements.

5.3.7 RACE TRACK TESTS

The performance of the proposed HEV has been verified in a small private racetrack placed inside the headquarter of Piaggio company (owner of Aprilia), as shown in Fig. 5.52. Table 5.15 reports main circuit features and weather conditions during the tests.

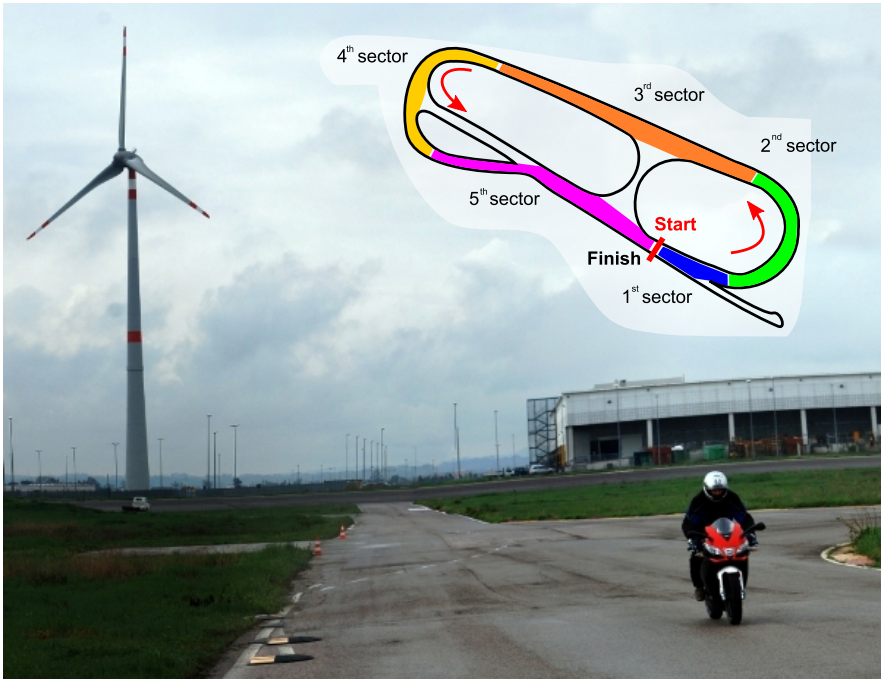

Figure 5.52: Photo of prototype motorcycle during the test in Pontedera racetrack.

In order to validate the final performance of the hybrid power train compared to the conventional one, two test sessions have been made: a first session with only ICE and a second

Table 5.15: Pontedera racetrack parameters.

Parameter	Value
1^{st} *sector* length	50 m
2^{nd} *sector* length	160 m
3^{rd} *sector* length	260 m
4^{th} *sector* length	130 m
5^{th} *sector* length	210 m
Weather condition	cloudy
Ground condition	wet
Ground temperature	$15\ ^{o}C$

session with hybrid power train. Fig. 5.53 collects telemetries of two laps with electric boost (solid line) and with conventional power train (dashed line). It is worth noticing that the results confirm an increasing of the top speed (about 20%) and a decreasing of the lap time (about 10%) with the hybrid power train despite the higher weight of HEV. Furthermore, results show that the energy consumption has been compensated by the on-board energy generation, because the amount of energy inside the ESS after two laps has not changed.

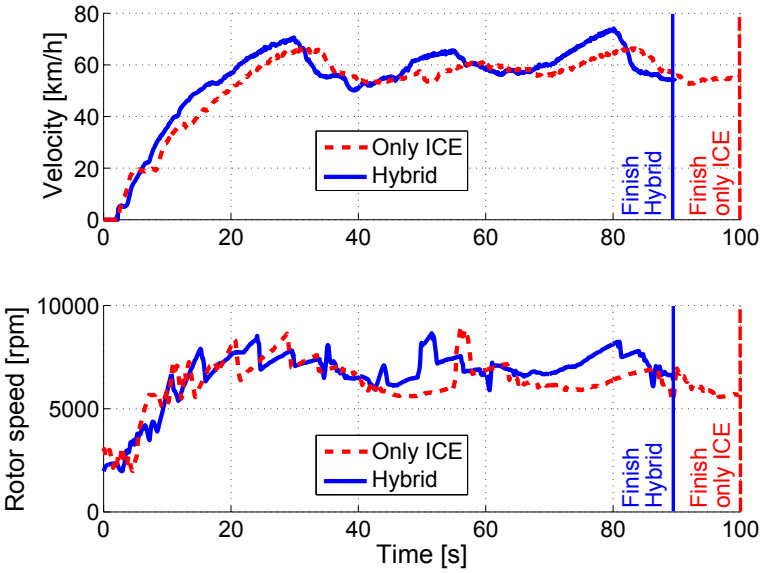

Figure 5.53: Performance of two laps with and without the hybrid configuration in Pontedera racetrack.

During the test session several electrical parameters have been acquired by means of the APX2 control unit, see Fig. 5.54. In according with the torque strategy imposed by VMCU, the peak power during the boost phase is $1800\ W$ whereas during the regenerative braking phase is $-1500\ W$.

Figs. 5.55 and 5.56 show graphical results of acceleration and deceleration performance respectively during the four laps in Pontedera racetrack with the hybrid power train. Fig. 5.55 highlights that the greater contribution of the EM is given during the most important acceler-

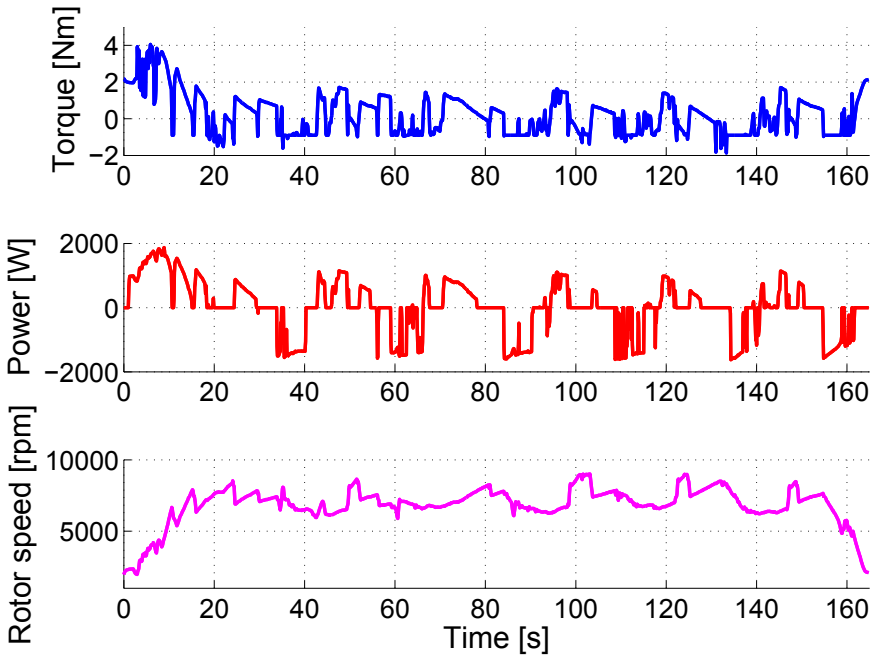

Figure 5.54: Electrical characteristics of HEV have been acquired in four laps in Pontedera racetrack.

ations that is when the vehicle runs at low speeds and when the internal combustion engine is more lacking of torque. Fig. 5.56 shows that a significant part of braking energy is recovered inside the ESS.

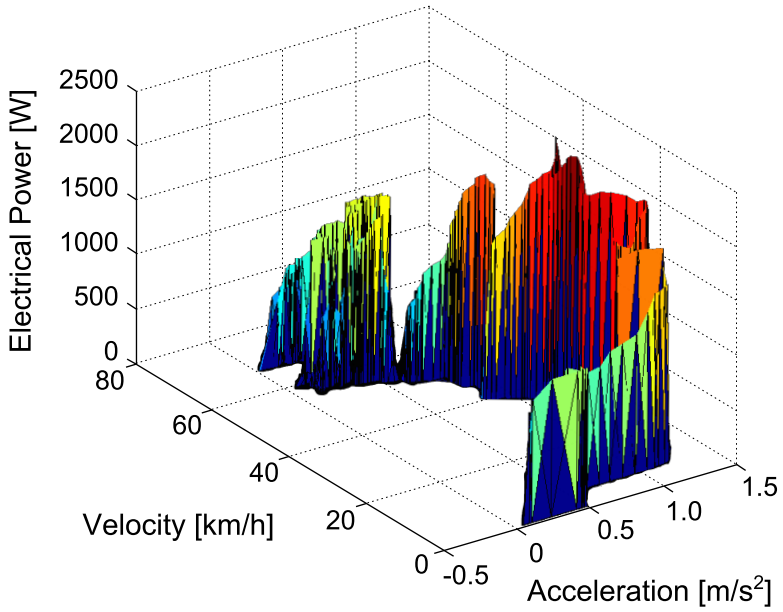

Figure 5.55: Performance of acceleration in Pontedera racetrack.

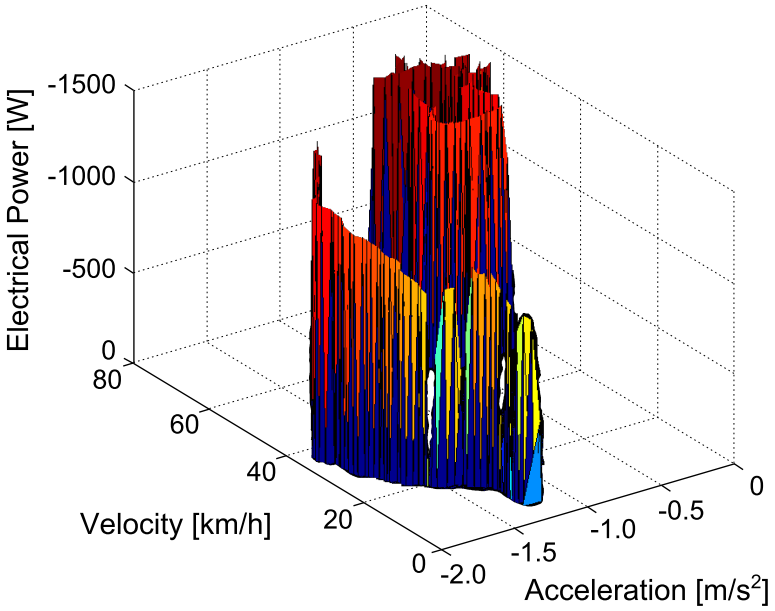

Figure 5.56: Performance of deceleration in Pontedera racetrack.

CONCLUSIONS

This thesis gives an overview on the hybrid power-trains suited for light vehicles. At the same time the thesis confirms that light hybrid vehicles are feasible because some prototypes have been manufactured and tested.

The integration between mechanical and electrical design is required since the dynamic behavior of the vehicle is strongly influenced by the masses of the electrical components. An accurate investigation makes possible high performances and high safety simultaneously.

The analytical model of the reluctance machine has been essential in the design of such a machines and the results are in agreement both with the finite element simulations and with the experimental results.

Series power-trains are the more challenging if they are developed for small powers ($300 - 400\ W$). The efficiency of the generator dramatically reduces the global efficiency of the series power-train.

The efficiency of the electrical machine influences the range of the vehicle, but the energy storage system is important as well. In this thesis the energy storage system has not been investigated even if the most part of the energy comes from it (i.e. there is also the contribution of the regenerative braking). In the next future a development in this field is desirable to promote hybrid and electrical vehicles.

There are still open issues dealing with hybrid and electric vehicles. From the energy density of the energy storage systems (and their costs) to the possibility to charge the energy storage system (network infrastructures), but electrical vehicles could be a valid alternative to the traditional (and polluting) vehicles equipped with internal combustion engines.

ACKNOWLEDGMENTS

The project "Velomobile" has been sponsored by Eurosystems S.p.a. of Reggio Emilia (Italy).

The project "Aprilia RS4 125 Hybrid" has been financed by Veneto Region (Italy); the MO.BI. (MOtociclette BImotorizzate) project leader was Aprila s.p.a. company.

I wish to thank the Professors Alberto Doria, Silverio Bolognani, Nicola Bianchi, Vittore Cossalter and Roberto Lot for the support in these three years.

I wish to thank my colleagues: Stefano Rota, Matteo Massaro, Matteo Formentini, Roberto Sartori, Mauro Tognazzo, Davide Tavernini, Enrico Giolo, Luca Taraborrelli, Massimiliano Caneri, Mattia Morandin, Emanuele Fornasiero, Enrico Carraro, Michele Degano and Damiano Mingardi.

A special thanks to Mosè Castiello for the nice experience in EdLab.

Bibliography

[1] F. Allen E., *Hybrid Vehicles and the Future of Personal Transportation*, 2009.

[2] J. Miller, "Hybrid electric vehicle propulsion system architectures of the e-cvt type," *Power Electronics, IEEE Transactions on*, vol. 21, no. 3, pp. 756–767, 2006.

[3] J. Miller, P. McCleer, and M. Everett, "Comparative assessment of ultra-capacitors and advanced battery energy storage systems in powersplit electronic-cvt vehicle powertrains," in *Electric Machines and Drives, 2005 IEEE International Conference on*, 2005, pp. 1513–1520.

[4] Q. Wang, Q. Wang, and X. Zeng, "Dynamic modelling and simulation of ths ii based on cruise software," in *Transportation, Mechanical, and Electrical Engineering (TMEE), 2011 International Conference on*, 2011, pp. 1075–1079.

[5] V. Cossalter, A. Doria, and M. Ferrari, "Potentialities of a light three-wheeled vehicle for sustainable mobility," in *Proceedings of the ASME Design Engineering Technical Conference*, vol. 6, 2012, pp. 523–532.

[6] M. Ferrari, N. Bianchi, A. Doria, and E. Fornasiero, "Design of synchronous reluctance motor for hybrid electric vehicles," in *IEEE International Electric Machines Drives Conference, IEMDC 2013*, 2013, pp. 1058–1065.

[7] M. Ferrari, N. Bianchi, and E. Fornasiero, "Rotor saturation impact in synchronous reluctance and pm assisted reluctance motors," in *IEEE Energy Conversion Congress and Exposition, ECCE 2013*, 2013, pp. 1235–1242.

[8] M. Bertoluzzo, G. Buja, V. Cossalter, and A. Doria, "Development of an easy-to-ride electric 3-wheel vehicle," in *FISITA World Automotive Congress 2008, Congress Proceedings - Vehicle Concepts, Body Design, Chassis Development*, vol. 5, 2008, pp. 62–71.

[9] V. Cossalter, *Motorcycle dynamics*, LULU, Ed., 2006.

[10] A. Fratta, G. Toglia, A. Vagati, and F. Villata, "Ripple evaluation of high-performance synchronous reluctance machines," *IEEE, Industry Applications Magazine*, vol. 1, no. 4, pp. 14 –22, jul/aug 1995.

[11] A. Vagati, M. Pastorelli, G. Francheschini, and S. Petrache, "Design of low-torque-ripple synchronous reluctance motors," *IEEE Transactions on Industry Applications*, vol. 34, no. 4, pp. 758 –765, jul/aug 1998.

[12] A. Vagati, A. Canova, M. Chiampi, M. Pastorelli, and M. Repetto, "Improvement of synchronous reluctance motor design through finite-element analysis," in *IEEE Industry Applications Conference, 1999.*, vol. 2, 1999, pp. 862 –871 vol.2.

[13] M. Barcaro and N. Bianchi, "Interior pm machines using ferrite to substitute rare-earth surface pm machines," in *International Conference on Electrical Machines (ICEM), 2012*, sept. 2012, pp. 1339 –1345.

[14] M. Barcaro, N. Bianchi, and F. Magnussen, "Rotor flux-barrier geometry design to reduce stator iron losses in synchronous ipm motors under fw operations," *IEEE Transactions on Industry Applications*, vol. 46, no. 5, pp. 1950 –1958, sept.-oct. 2010.

[15] S. Morimoto, Y. Takeda, T. Hirasa, and K. Taniguchi, "Expansion of operating limits for permanent magnet motor by current vector control considering inverter capacity," *IEEE Transactions on Industry Applications*, vol. 26, no. 5, pp. 866–871, Sep/Oct 1990.

[16] D. A. Staton, T. J. E. Miller, and S. E. Wood, "Maximising the saliency ratio of the synchronous reluctance motor," *IEEE Transaction on Industry Applications*, vol. 140, no. 4, July 1993.

[17] N. Bianchi, S. Bolognani, D. Bon, and M. D. Pre', "Rotor flux-barrier design for torque ripple reduction in synchronous reluctance and pm-assisted synchronous reluctance motors," *IEEE Transaction on Industry Applications*, vol. 45, no. 3, May-June 2009.

[18] R. R. Moghaddam, "Synchronous Reluctance Machine (SynRM) Design," 2007, Royal Institute of Technology.

[19] N. Bianchi and M. Barcaro, "Iron losses reduction in synchronous motors with anisotropic rotor," in *34th Annual Conference of IEEE Industrial Electronics, IECON 2008.*, Nov., pp. 1258–1263.

[20] P. Alotto, M. Barcaro, N. Bianchi, and M. Guarnieri, "Optimization of interior pm motors with machaon rotor flux barriers," *IEEE Transactions on Magnetics*, vol. 47, no. 5, pp. 958 –961, may 2011.

[21] N. Bianchi, E. Fornasiero, and S. Bolognani, "Effect of stator and rotor saturation on sensorless rotor position detection," in *IEEE Energy Conversion Congress and Exposition (ECCE)*, sept. 2011, pp. 1528 –1535.

[22] S. Morimoto, Y. Takeda, T. Hirasa, and K. Taniguchi, "Expansion of operating limits for permanent magnet motor by current vector control considering inverter capacity," *Industry Applications, IEEE Transactions on*, vol. 26, no. 5, pp. 866–871, 1990.

[23] W. Soong and T. Miller, "Field-weakening performance of brushless synchronous ac motor drives," *IEE Proceedings on Electric Power Applications*, vol. 141, no. 6, pp. 331–340, 1994.

[24] T. Jahns, "Flux-weakening regime operation of an interior permanent-magnet synchronous motor drive," *IEEE Transactions on Industry Applications*, vol. IA-23, no. 4, pp. 681–689, 1987.

[25] M. O. Kaya, "Free vibration analysis of a rotating timoshenko beam by differential transform method," *Aircraft Engineering and Aerospace Technology*, vol. 78, no. 3, pp. 194 – 203, 2006.

[26] J.-H. Park, H.-Y. Park, S.-Y. Jeong, S.-I. Lee, Y.-H. Shin, and J.-P. Park, "Linear vibration analysis of rotating wind-turbine blade," *Current Applied Physics*, vol. 10, no. 2 SUPPL., pp. S332 – S334, 2010.

[27] H. Yoo and S. Shin, "Vibration analysis of rotating cantilever beams," *Journal of Sound and Vibration*, vol. 212, no. 5, pp. 807 – 808, 1998.

[28] B. Drew, M. Barker, J. Darling, K. Edge, and H. Johannsen, "Review of tilting three-wheeled vehicle chassis," *FISITA*, no. F2004F382, 2004.

[29] T. Gillespie, *Fundamentals of Vehicle Dynamics*. SAE,Warrendale, 1992.

[30] M. Barker, B. Drew, J. Darling, K. Edge, and G. Owen, "Steady-state steering of a tilting three-wheeled vehicle," *Vehicle System Dynamics*, vol. 48, no. 7, pp. 815–830, July 2010.

[31] V.Cossalter, N.Ruffo, F.Biral, R.Berritta, and G.Cocco, "Development of a Novel Three-Wheeled Vehicle," 2000, 3^{rd} IfZ International Motorcycle Conference.

[32] M. Bertoluzzo, G. Buja, V. Cossalter, A. Doria, and D. Mazzaro, "Getting around in electric vehicles," *IEEE Industrial Electronics Magazine*, no. F2008-07-022, pp. 10–18, September 2008.

[33] F. Van De Walle, in *The Velomobile as a Vehicle for more Sustainable Transportation*, 1988, pp. 1651–0194.

[34] K. M. Rahman, B. Fahimi, G. Suresh, A. V. Rajarathnam, and M. Ehsani, "Advantages of switched reluctance motor applications to ev and hev: Design and control issues," *Industry Applications, IEEE Trans*, vol. 36, no. 1, Jan/Feb 2000.

[35] M. Ferrari, N. Bianchi, A. Doria, E. Giolo, E. Fornasiero, C. Martignoni, and F. Bovi, "Development of a hybrid human-electric propulsion system for a velomobile," in *8th International Conference and Exhibition on Ecological Vehicles and Renewable Energies (EVER)*, 2013, pp. 1–8.

[36] M. Bertoluzzo, G. Buja, V. Cossalter, A. Doria, and D. Mazzaro, "Getting around in electric vehicles," *IEEE Industrial Electronics Magazine*, vol. 2, no. 3, pp. 10–18, 2008.

[37] A. Doria, M. Tognazzo, G. Cusimano, V. Bulsink, A. Cooke, and B. Koopman, "Identification of the mechanical properties of bicycle tyres for modelling of bicycle dynamics," *Vehicle System Dynamics*, vol. 51, no. 3, pp. 405–420, 2013.

[38] F. Rowland Whitt and D. Gordon Wilson, "Bicycle science," vol. 2, 1995.

[39] V. Cossalter, "Patent: Meccanismo per la realizzazione di un veicolo a tre ruote con parte anteriore rollante," no. IT1998PD00042 19980302, 1999.

[40] P. Alotto, M. Barcaro, N. Bianchi, and M. Guarnieri, "Optimization of interior pm motors with machaon rotor flux barriers," *IEEE Transactions on Magnetics*, vol. 47, no. 5, pp. 958 –961, may 2011.

[41] A. Doria and R. Lot, "The generalized torque approach for analyzing the results of pedaling tests," *Journal of Biomechanical Engineering*, vol. 123, no. 1, pp. 33–39, 2001, cited By (since 1996):1. [Online]. Available: www.scopus.com

[42] G. J. Van Ingen Schenau, W. W. L. M. Van Woensel, P. J. M. Boots, R. W. Snackers, and G. De Groot, "Determination and interpretation of mechanical power in human movement: Application to ergometer cycling," *European journal of applied physiology and occupational physiology*, vol. 61, no. 1-2, pp. 11–19, 1990, cited By (since 1996):30. [Online]. Available: www.scopus.com

[43] M. Ceraolo, A. Caleo, P. Capozzella, M. Marcacci, L. Carmignani, and A. Pallottini, "A parallel-hybrid drive-train for propulsion of a small scooter," *Power Electronics, IEEE Trans*, vol. 21, no. 3, pp. 768 –778, May 2006.

[44] N. Bianchi, S. Bolognani, and M. Zigliotto, "High-performance pm synchronous motor drive for an electrical scooter," *Industry Applications, IEEE Trans*, vol. 37, no. 5, pp. 1348 –1355, Sep./Oct. 2001.

[45] A. Khaligh and Z. Li, "Battery, ultracapacitor, fuel cell, and hybrid energy storage systems for electric, hybrid electric, fuel cell, and plug-in hybrid electric vehicles: State of the art," *Vehicular Technology, IEEE Trans*, vol. 59, no. 6, pp. 2806 –2814, July 2010.

[46] M. Ayad, M. Becherif, S. AitCheikh, and M. Wack, "The use of supercapacitors in electrical vehicle: Modeling, sizing and control," in *Vehicle Power and Propulsion Conference, IEEE*, Sept. 2010, pp. 1 –6.

[47] T. Nobuaki, S. Imai, Y. Horii, and H. Yoshida, "Development of high-performance lithium-ion batteries for hybrid electric vehicles," *Tech. Rev., New Technol.*, 2003.

[48] D. Reisner and M. Klein, "Bipolar nickel-metal hydride battery for hybrid vehicles," *Aerospace and Electronic Systems Magazine, IEEE*, vol. 9, no. 5, pp. 24 –28, May 1994.

[49] D. Edwards and C. Kinney, "Advanced lead acid battery designs for hybrid electric vehicles," in *Applications and Advances, 2001. The Sixteenth Annual Battery Conference on*, 2001, pp. 207 –212.

[50] E. Karden, S. Ploumen, B. Fricke, T. Miller, and K. Snyder, "Energy storage devices for future hybrid electric vehicles," *J. Power Sources*, vol. 168, no. 1, pp. 2–11, May 2007.

[51] M. Ferrari, M. Morandin, and S. Bolognani, "Mild hybrid motorcycles: Choice of the energy storage system," in *IEEE International Energy Conference and Exhibition (ENERGYCON)*, sept. 2012, pp. 997 –1002.

[52] M. Morandin, M. Ferrari, and S. Bolognani, "Design and performance of a power train for mild-hybrid motorcycle prototype," in *IEEE International Electric Machines Drives Conference (IEMDC)*, 2013, pp. 1–8.

[53] L. Alberti, M. Barcaro, M. Prè and, A. Faggion, L. Sgarbossa, N. Bianchi, and S. Bolognani, "Ipm machine drive design and tests for an integrated starter alternator application," *IEEE Transactions on Industry Applications*, vol. 46, no. 3, pp. 993 –1001, may-june 2010.

[54] I. Ilina, "Experimental determination of moment to inertia and mechanical losses vs. speed, in electrical machines," in *Advanced Topics in Electrical Engineering (ATEE), 2011 7th International Symposium on*, May 2011, pp. 1–4.

[55] FSBB30CH60C Smart Power Module, Fairchild Semiconductor, *www.fairchildsemi.com/pf/FS/FSBB30CH60C*, February 2008.

[56] N. Mohan, T. Undeland, and W. P. Robbins, *Power Electronics: Converters, Applications, and Design*, W. John and Sons, Eds., 2003.

[57] D. V. Ragone, in *Mid-Year Meeting of the Society of Automotive Engineers*.

[58] J. Martinez, "Modeling and characterization of energy storage devices," in *Power and Energy Society General Meeting, 2011 IEEE*, july 2011, pp. 1 –6.

[59] S. Lukic, J. Cao, R. Bansal, F. Rodriguez, and A. Emadi, "Energy storage systems for automotive applications," *Industrial Electronics, IEEE Transactions on*, vol. 55, no. 6, pp. 2258 –2267, june 2008.

[60] "Battery performance models in advisor," *Journal of Power Sources*, vol. 110, no. 2, pp. 321 – 329, 2002.

[61] KAN AA(50)1800, Kan battery co., *www.kanbattery.com*, 2004.